DISS. ETH NO. 28309

On Blood and Mechanical Motion Sensitization of Encoding and Decoding in Magnetic Resonance Imaging

A thesis submitted to attain the degree of

DOCTOR OF SCIENCES OF ETH ZURICH
(Dr. sc. ETH Zurich)

presented by

HANNES DILLINGER
MSc, TU Wien
born on 24.11.1990
citizen of Austria

accepted on the recommendation of
Prof. Dr. Sebastian Kozerke
Prof. Dr. Dominik Obrist

2022

This page is intentionally left blank.

Abstract

The assessment of three-dimensional blood flow dynamics by means of Phase-Contrast Magnetic Resonance Imaging (PC-MRI) holds promising potential for the non-invasive diagnosis of diseases of individual vessels and entire structures such as the heart. A variant of PC-MRI, 4D Flow MRI, offers novel biomarkers, which are gaining importance for the classification of e.g. valvular heart disease. The evaluation of mean blood flow and turbulence, by additionally encoding the Reynolds stress tensor, may further enable the quantification of stenosis severity, the assessment of hemolysis and other factors. As these markers can influence clinical decision making, knowledge of the accuracy and precision of the estimated parameters is of utmost importance. Given the intrinsic limitations of PC-MRI in terms of spatial and temporal resolution and the employed hardware, estimated flow parameters are sensitized to the blood flow itself but also to other, undesired contributions. In addition, long acquisition times in 4D Flow MRI hamper its clinical applicability and patient acceptance.

In previous works, the echo planar imaging (EPI) readout technique has been suggested to reduce the time needed for acquisition of 4D Flow MRI exams. Here, it is shown that employing EPI for 4D Flow MRI results in misregistration, velocity estimation errors and degrading spatial resolution depending on blood flow patterns. Therefore, it is concluded that for shortening scan time other acceleration methods such as compressed sensing in conjunction with standard gradient echo (GRE) imaging are favorable.

Current turbulence encoding models for PC-MRI are based on assumptions regarding the time scales of the underlying flow field. In this work, the turbulence encoding model is derived and related to diffusion MRI and turbulence theory. Results of PC-MRI simulations employing large eddy simulation (LES) data as input show that current turbulence encoding models need to be revisited as they systematically underestimate turbulence parameters. Subsequently, a correction method based on probing the Lagrangian turbulence spectrum is presented and used to gauge the encoding model to reinstate the accurateness of turbulence parameter estimation. The method is demonstrated for PC-MRI of stenotic flows.

While encoding and reconstruction techniques can be further optimized, MRI hardware limitations remain. Based on a linear, time-invariant description of the MRI gradient system, the influence of mechanical resonances on PC-MRI data are highlighted. It is shown that residual background phases, which result in biased velocity estimation, can be reduced both in amplitude and spatial order by PC-MRI sequence optimization. The influence of mechanical resonances on spatial encoding is evaluated, demonstrating that EPI readouts are particularly vulnerable to undesired contributions due to mechanical motion of the gradient system. The gradient performance of lower-field systems is shown to benefit from reduced Lorentz forces, mitigating the influence of mechanical resonances. This benefit is contrasted with the reduced signal-to-noise ratio of lower-field systems. Based on a comparison of an MRI system operated at standard and at lower-field strength, increased gradient fidelity as well as reduced sound pressure levels are demonstrated for the lower-field configuration.

Kurzfassung

Die Quantifizierung des dreidimensionalen Blutflusses durch die Phasenkontrast-Magnetresonanzbildgebung (PC-MRI) hat vielversprechendes Potential für eine nicht-invasive Diagnose von Erkrankungen einzelner Gefässe und ganzer Strukturen wie das Herz. Mit der PC-MRI Erweiterung, 4D Fluss MRI, stehen neue Biomarker zur Verfügung, welche an Bedeutung für die Klassifikation von z.B. Klappenerkrankungen gewinnen. Die Evaluation des mittleren und turbulenten Blutflusses, durch die zusätzliche Kodierung des Reynolds Spannungstensors, ermöglicht eine Quantifizierung des Stenosegrades, eine Abschätzung der Hämolyse und anderer Faktoren. Da diese Parameter die klinische Entscheidungsfindung direkt beeinflussen, ist ihre Genauigkeit von höchster Wichtigkeit. Die intrinsischen Limitationen der PC-MRI im Bezug auf örtliche und zeitliche Auflösung und in Bezug auf die zur Verfügung stehende Hardware resultieren in einer Abhängigkeit der geschätzten Flussparameter nicht nur vom Blutfluss selbst, sondern auch von anderen, ungewollten Beiträgen. Zusätzlich ist die klinische Praktikabilität und die Akzeptanz durch Patienten limitiert durch die lange Acquisitionszeit von 4D Fluss MRI Protokollen.

In vorangegangenen Studien wurde die Echo Planar Imaging (EPI) Methode verwendet, um die Akquisitionszeit von 4D Fluss MRI Untersuchungen zu verkürzen. In der vorliegenden Arbeit wird nun gezeigt, dass EPI für 4D Fluss MRI in fehlerhafter örtlicher Abbildung, Fehlern in der Schätzung der Geschwindigkeiten und in einer reduzierten örtlichen Auflösung in Abhängigkeit des Flussfeldes resultiert. Basierend auf den Ergebnissen wird geschlussfolgert, dass zur Verkürzung der Akquisitionszeit andere Beschleunigungsmethoden wie z.B. Compressed Sensing in Verbindung mit einer Standard Gradient Echo (GRE) Auslesetechnik besser geeignet sind.

Aktuelle Turbulenzkodierungsmodelle für PC-MRI basieren auf Annahmen über Zeitskalen des abzubildenden Flussfeldes. In der vorliegenden Arbeit wird das Kodiermodell hergeleitet und in Beziehung zur Diffusions- und Turbulenztheorie gesetzt. Ergebnisse von PC-MRI Simulationen basierend auf Large-Eddy Simulationsdaten (LES) zeigen, dass aktuelle Turbulenzkodiermodelle überarbeitet werden müssen, da sie eine systematische Unterschätzung der Turbulenzparameter ergeben. Folglich wird eine Korrekturmethode basierend auf der Abtastung des Lagrange Turbulenzspektrums präsentiert, um die Genauigkeit der Schätzung der Turbulenzparameter zu verbessern. Die Methode wird am Beispiel PC-MRI für stenotische Flüsse demonstriert.

Während Kodier- und Rekonstruktionsmethoden weiter optimiert werden können, bleiben Hardwarelimitationen von MRI-Systemen bestehen. Basierend auf der linearen, zeitinvarianten Beschreibung des MRI-Gradientensystem wird der Einfluss von mechanischen Resonanzen auf PC-MRI Daten beleuchtet. Es wird gezeigt, dass verbleibende Hintergrundphasen, die in fehlerhaften Geschwindigkeitsschätzungen resultieren, durch die Optimierung der PC-MRI Sequenz in ihrer Amplitude und der örtlichen Ordnung reduziert werden können. Der Einfluss von mechanischen Resonanzen auf die Ortskodierung wird evaluiert, wobei gezeigt wird, dass besonders die EPI Auslesetechnik anfällig für ungewollte Beiträge durch mechanische Bewegung des Gradientensystems ist. Die Gradientengenauigkeit von Niederfeldsystemen profitiert von

reduzierten Lorentz-Kräften, welche den Einfluss der mechanischen Resonanzen reduzieren. Dieser Vorteil wird dem verringerten Signal-zu-Rausch-Verhältnis von Niederfeldsystemen gegenübergestellt. Basierend auf einem Vergleich eines MRI Systems, welches bei Standard- und Niederfeldstärke betrieben wurde, wird die erhöhte Gradientengenauigkeit und reduzierte Schallpegel bei Niederfeldkonfiguration gezeigt.

Contents

Introduction

Magnetic Resonance Imaging (MRI) has become a key factor in non-invasive clinical decision making for many disciplines. Since its conception more than 50 years ago[1], a plethora of applications has been developed, aimed at gaining a deeper understanding on the emergence and progression of pathologies.

For the assessment of cardiovascular function, phase-contrast MRI (PC-MRI) offers comprehensive, time-resolved information about blood flow in vessels[2]. In its extension, 4D Flow MRI, the acquisition is performed in a volumetric manner, which covers a volume of interest (VOI). The description of derived 3D flow characteristics over time, such as flow jet angle[3], flow displacement[3], vorticity[4], wall shear stress[5], pulse wave velocity[6] and pressure gradient[7] has triggered clinical interest[8–10]. Of particular significance is generalized turbulence encoding[11] using 4D Flow MRI, which may serve as a surrogate measure of net pressure loss across and downstream of stenotic heart valves[12].

Despite its advantages and new possibilities for the evaluation of cardiac blood flow dynamics, the use of MRI in the clinic is hampered by long acquisition durations[13], resulting in limited patient compliance and increased cost per examination. In the case of coronary artery disease, however, non-invasive cardiovascular MR was found to offer cost savings of up to 48% compared to invasive coronary angiography for in-patient tests (overnight stay) at Swiss hospitals[14].

To further increase the clinical and economical acceptance of more comprehensive MRI protocols, considerable research attention has been devoted to shortening scan times. Novel methods such as compressed sensing[15], free running acquisition without the need for breath holds and motion-resolved reconstruction[16] and the application of inherently faster acquisition strategies[17] have been proposed. Due to the lack of true ground truth in non-invasive imaging, however, the accuracy of newly conceived methods must be compared to current gold standard or other previously established techniques.

To date, Doppler echocardiography is the preferred diagnostic method for assessing valvular heart disease[18]. Besides the visual depiction of size, wall thickness or orifice area, velocity measurements enable the determination of increased afterload for the ventricle[19] based on estimation of the pressure gradient across the valve. The simplified Bernoulli equation relates the maximum blood flow velocity found at the vena contracta to the pressure gradient, which is then used to gauge the severity of aortic stenosis[18]. However, as the simplified equation not only neglects compressibility and frictional effects but assumes irrotational flow and, most importantly, identical cross-sectional areas up- and downstream of the valve, unreliable results are to be expected[20]. Several extensions of the Bernoulli equation have been proposed[21,22], describing correction approaches to reduce overestimation of pressure gradients, resulting in increased accuracy[23]. Despite the advances, Doppler echocardiography itself remains highly observer dependent[24]. In addition, in some patients paradoxical low-flow conditions with reduced survival rates[25] have been reported. Unfortunately, the reference method for Doppler pressure estimation is in fact invasive catherization, which is not favorable from a patient-centered point of view.

In-vivo PC-MRI measurements have been validated against non-invasive methods such as Doppler ultrasound imaging, which in turn has the aforementioned drawbacks, or other flow MRI techniques, which have previously been established and accepted for their accuracy and reproducibility[26]. However, the challenge remains that MRI experiments are influenced by a vast number of imaging parameters. In order to provide guidance for parameter selection, a number of key settings have been suggested for 4D Flow MRI[27]. In general, parameter settings ought to be published alongside the actual data whenever possible to support reproducible research[28]. Nevertheless, the repeat accuracy may be limited when deploying identical imaging protocols on different MRI systems[29]. Another challenge for reproducible research relates to ethical constraints, as the use or sharing of medical data requires appropriate consent by the patient[30], which is an opt-in scheme in Switzerland currently[31] (Sec.2, Art.16f).

Paired synthetic ground-truth and MRI imaging data obtained through simulations can serve as an indispensable tool to quantify systematic and random errors of MRI acquisition, reconstruction and post-processing techniques. To this end, solutions to the Bloch equations[32] may be employed to describe the evolution of the MRI signal over time in response to different types of flow and for different imaging conditions. Assuming the application of time-varying magnetic field gradients, complex-valued signals of an ensemble of magnetic moments can be calculated, which can then be processed to form images via the inverse Fourier transformation[33].

Simulation approaches can range from analytical Eulerian solutions for simplified phantoms[34,35] to numerical Eulerian-Lagrangian[36] or Lattice Boltzmann[37,38] solutions for turbulent flows, for example. Alongside, the computational complexity of models increases making necessary approximations and simplifications of the underlying processes to be simulated.

Today, the growing compute capacity of high-performance computing systems enables MRI simulations based on first principles including sophisticated ground truth data synthesis. For example, computational fluid dynamics (CFD) simulations, employing direct numerical simulation (DNS) or a large eddy simulation (LES) approach, allow the generation of complex flow fields as input for advanced MRI simulations of mean and turbulent fluid flows. This helps to better understand details of the encoding process of PC-MRI of laminar[39] and turbulent flows[40] or diffusion[41], as it allows the observation of variables during simulation which would not be accessible in a real-world experiment.

Measurement data from real-world MRI experiments may still differ from simulation results due to hardware imperfections of MRI systems[42] and patient-induced distortions. For example, imperfections of the gradient chain[43] as well as radio-frequency and main field inhomogeneity[44] may not have been considered in simulations. These factors, however, may also impact the overall accuracy and precision of the measurements and hence potentially also impact decision making based on PC-MRI[18,45].

One approach to address the gap between simulations with limited MRI modelling scope and real-world MRI experiments is data assimilation[46,47]. Recently, the filtering of simulated 4D Flow MRI data based on DNS forecasts has been presented[48], with the potential to enhance the spatiotemporal resolution of in-vivo 4D Flow MRI in the future.

Another promising approach is to extend the validity of the encoding model to real-world MRI systems by incorporating their characteristics into the simulation model[49,50]. To this end, hardware imperfections may be accounted for at the time of data acquisition or during data reconstruction. The former option promotes optimal operational states of the system over suboptimal ones (PC-MRI sequence optimization[49,51,52]) whereas the latter is preferred as long as simplified descriptions of the MRI system can be found (linear time invariance (LTI)[53], thermal modeling[54]) and used for correction of k-space trajectories[55]. Applying Conant and Ashby's theorem[56]: "*every good regulator of a system must be a model of that system*" to the MRI acquisition and reconstruction process implies that undesired system behavior should be avoided as much as possible by prospectively incorporating model knowledge into the MRI measurement design (referring to the model in the theorem). Any effects that cannot be considered by the former must ultimately be corrected for by retrospective corrections (referring to the regulator in the theorem).

Outline

Section 1 introduces the encoding and reconstruction model for spatial position and velocity in PC-MRI in the presence of flow, where sample motion during spatial encoding is identified as erroneous signal contribution.

Evaluation of the loss of resolution, errors in velocity estimation and misregistration due to sample motion is subject of the published article in Section 2. The section encompasses conclusions, which favor GRE over EPI based on insights derived from combined computational fluid dynamics and MRI simulations.

Section 3 generalizes the encoding and reconstruction model to non-resolvable scales, resulting in a statistical description of the encoding process. The relation of the encoding of randomized motion and turbulent flow is introduced. Not necessarily limited to, but focused on turbulent flow encoding in MRI, timescales of both the encoding and the random motion process itself are shown to be intertwined.

The published article in Section 4 introduces a mathematical derivation of the MRI signal model when random motion is present. Challenging current turbulence encoding models, it is demonstrated that the validity of currently used models may not be universally supported.

Section 5 focuses on MRI system characterization using a description of the MRI gradient system as a linear time invariant system, including the definition of the gradient modulation transfer function and its application to sequence optimization to mitigate the influence of mechanical resonances. The impact of mechanical motion of the MRI gradient system on spatial encoding and velocity encoding is the subject of Section 5.5 and Section 5.7, respectively. The SNR dependency on field strength is discussed, while potential opportunities of lower-field strength systems are identified.

Finally, Section 6 focuses on the direct comparison of a clinical MRI system at its product (3T) and lower-field strength (0.75T) configuration. Improvements in gradient fidelity and reduced sound pressure levels at 0.75T are demonstrated.

Contributions of the Thesis

In this thesis, several important aspects influencing the accuracy of PC-MRI are illustrated. The loss of resolution, flow misregistration and quantification errors when applying echo planar imaging techniques in fast flow regimes are evaluated by employing point spread function analysis and flow field comparisons. It is demonstrated that echo planar imaging is not suitable for imaging of fast flows for diagnosing aortic stenosis for example.

Current signal models for turbulence quantification are based on assumptions of temporal scales and correlations of the underlying random motion process. In the work at hand, light is shed on the encoding process itself employing a comprehensive signal model, which demonstrates that assumptions on temporal scales do not hold for high Reynolds flows. Highlighting the similarities between diffusion and turbulence encoding in MRI, it is possible to connect concepts from turbulence theory such as the Lagrangian correlation time to concepts from diffusion MRI. A derivation of the complete signal model is given and its implication on the estimation of statistical turbulence parameters is evaluated. Based on simulations, current signal models are found to systematically underestimate turbulence. To this end, a correction method is proposed. In addition, a novel method to probe the Lagrangian motion spectra of turbulent flows using tailored gradient waveforms is proposed to estimate the Lagrangian motion spectra on a voxel basis, which could further improve the accuracy of turbulence parameter estimation and may offer insights for research on turbulence theory.

Imperfections of the MRI gradient system itself are highlighted with a focus on mechanical resonances. The description of the gradient system as a linear, time-invariant system offers characterization of the system in terms of the gradient modulation transfer function and enables sequence optimization to mitigate undesirable effects on spatial and velocity encoding.

Subsequently, opportunities of lower-field MRI systems are discussed with a focus on signal-to-noise ratio, specific absorption rate, acoustic noise and mechanical resonances. Finally, by comparison of the same MRI system at standard and lower-field configuration in terms of the gradient modulation transfer function and acoustic noise spectra, it is concluded that lowering the field strength increases gradient fidelity and patient comfort due to reduced sound pressure levels.

1 Encoding and Decoding in MRI

1.1 Sequence Building Blocks

Excitation, encoding and data acquisition in MRI is performed in a sequential manner. A series of building blocks comprising radiofrequency (RF) pulses and magnetic field gradients is depicted in Figure 1.1. Radiofrequency transmission and spin preparation is performed during t_{RF} and t_{prep}, respectively. Data acquisition is performed during t_{enc} where the echo time TE describes the time point of the maximum echo signal. Gradients during t_{post} spoil residual transverse magnetization or ensure balancing gradient moments, for example. The series of building blocks is repeated with repetition time TR where changes in t_{prep} and t_{post} allow sensitization for velocity or other tissue properties.

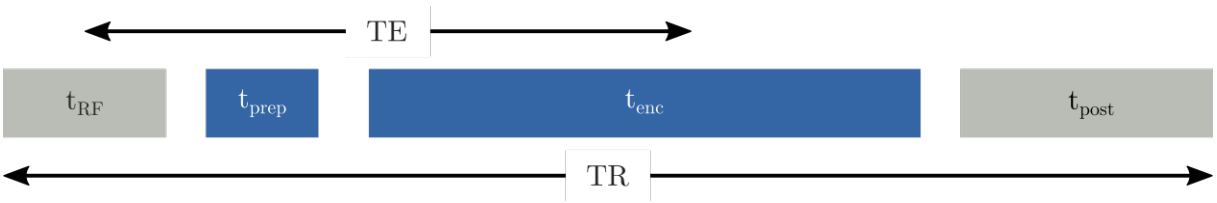

Figure 1.1: MR sequence building blocks consisting of RF excitation t_{RF}, spin preparation block t_{prep}, spatial encoding block t_{enc} and post-acquisition block t_{post}. The sequence of blocks is repeated with repetition time TR and the echo time TE denotes the duration between the center of the RF pulse and the center of acquisition.

1.2 MRI Signal Model for Encoding

Assuming excitation during the t_{RF} block, magnetization is tipped into the transverse plane. Signal is detected through Faraday induction using a suitable RF receive coil. Given transverse magnetization $M_{xy}(\vec{r},t)$, the signal during the spatial encoding block t_{enc} is given as

$$d(\vec{k},t) = \int_{\mathcal{V}} M_{xy}(\vec{r},t)\ \mathrm{e}^{\alpha(\vec{r},t)}\ \mathrm{e}^{\mathrm{j}\varphi(\vec{r},t)}\ \mathrm{e}^{\mathrm{j}\vec{k}_{enc}(t)\cdot\vec{r}(t)}\ \mathrm{d}\vec{r} + \text{noise}\ , \tag{1.1}$$

where $\alpha(\vec{r},t)$ and $\varphi(\vec{r},t)$ denote amplitude and phase modulation functions, respectively. These modulation functions are further described in Section 1.3 and Section 3.2, respectively. The application of magnetic field gradients $\vec{G}_{enc}(t)$ results in the wave vector $\vec{k}_{enc}(t) = \gamma \int_0^t \vec{G}_{enc}\,(t')\ \mathrm{d}t'$ used for spatial encoding. Of note, the relationship between position $\vec{r}(t)$ and the MRI signal's phase $d(\vec{k}_{enc},t)$ is linear in $\vec{k}_{enc}(t)$. As the magnetic field gradients can be applied in three orthogonal axes, the 3D spatial distribution of magnetization within a sample can be mapped to spatial frequencies in three main directions, which forms the k-space. The Fourier relationship between image coordinates $\vec{r}(t)$ and frequency space $\vec{k}_{enc}(t)$ holds.

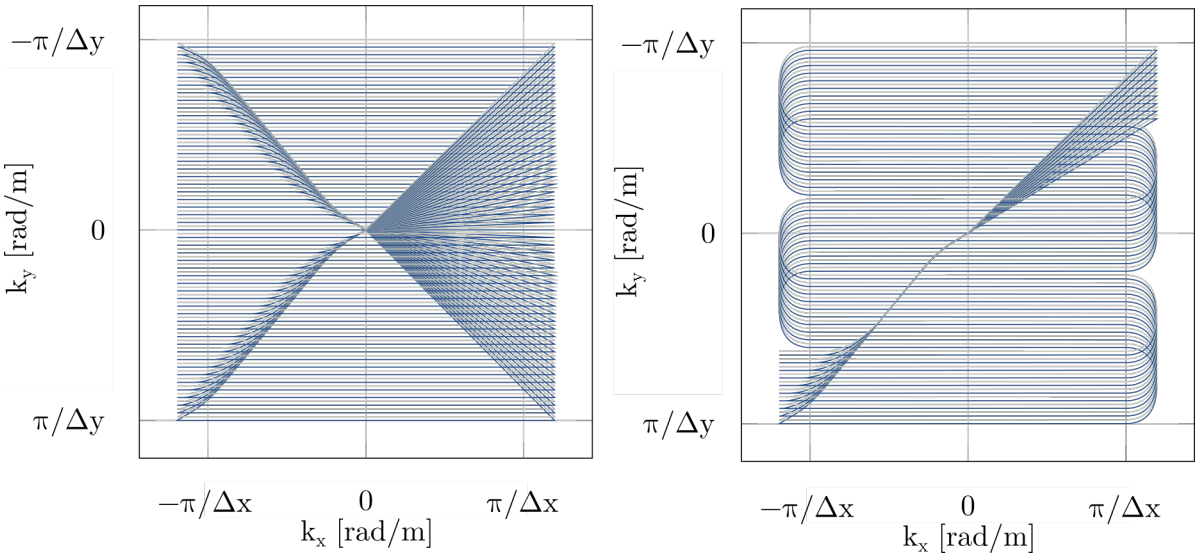

Figure 1.2: Traversing through k-space is described by the k-space trajectory. (A) Gradient Echo (GRE) trajectory acquiring a single k-space line per excitation along the frequency encoding direction k_x. (B) Exemplary Echo Planar Imaging (EPI) trajectory acquiring 5 lines per excitation.

Traversing k-space, using wave vector $\vec{k}_{enc}$, is described by the k-space trajectory; shown for a 2D example in Figure 1.2. The time point when the corresponding trajectory crosses the ordinate (or the origin for EPI) is referred to as echo time (TE). A variety of trajectories have been proposed, such as gradient echo[57,58] (GRE), echo planar imaging[59] (EPI), radial[60], spiral[61] and ultra-short echo-time imaging (UTE[62]). Data acquisition is performed at discrete time points while applying a magnetic field gradient. The discretization is described by $\vec{k}_{enc}(t) \mapsto \vec{k}_{enc,\kappa}$ where $\kappa = \{1, 2, \ldots, n\}$ and n is the number of acquired samples during one encoding block. The underlying process of oversampling, demodulation and averaging will not be further discussed here but can be found elsewhere[63]. Of note, the magnetization $M_{xy}(\vec{r}, t)$ and the integral over the volume $\mathcal{V}$ remain continuous. Discretization of the spatial position $\vec{r}$ gives rise to the so-called inverse crime problem, resulting in overly optimistic results[34].

A typical gradient echo sequence for phase contrast MRI (PC-MRI), employing a Cartesian readout trajectory, is shown in Figure 1.3. It comprises spatially selective excitation during t_{RF} by a time-varying magnetic field $\vec{B}_1(t)$ and a magnetic field gradient $\vec{G}(t)$ being played out at the same time. During t_{prep}, a pair of gradient lobes forms a bipolar waveform to sensitize the current sequence block to flow. During t_{enc}, spatial encoding is performed by stepping phase-encode gradients in every repetition and by playing out frequency encoding gradients. The echo time can be minimized by incorporation of velocity encoding gradients in the spatial encoding gradients[64]. During t_{post}, additional gradients are introduced to either balance gradient moments or to eliminate any remaining transverse magnetization.

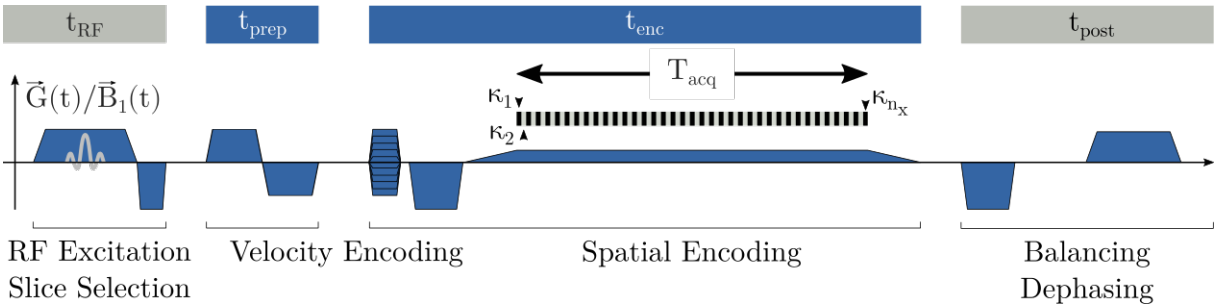

Figure 1.3: Gradient Echo sequence (GRE) consisting of RF excitation and slice-select gradient, followed by a bipolar gradient for velocity encoding. Spatial encoding is performed by phase-encode gradients and a prephaser followed by the readout gradient. Data acquisition is performed during continuous time intervals with centers described by discrete time points κ_n ranging from 1 to the number of samples n_x to be acquired within one TR. Balancing or dephasing is employed at the end of the sequence.

1.3 Phase Modulation Function

The phase modulation function in Equation (1.1) can be written as

$$\varphi(\vec{r},t) = \underbrace{\sum_{n=1}^{\infty} \frac{1}{n!} \frac{\mathrm{d}^{(n)}\vec{r}(t)}{\mathrm{d}t^{(n)}}\bigg|_{t=t_0} \gamma \int_{t_0}^{t} \vec{G}_{prep}(t') \ (t'-t_0)^n \ \mathrm{d}t'}_{\varphi_{prep}(\vec{r},t)} + \varphi_{background}(\vec{r},t) + \varphi_{system}(\vec{r},t) \ , \tag{1.2}$$

where the RHS sum includes the integral over the Taylor series of position $\vec{r}(t)$ multiplied by the gyromagnetic ratio γ and preparation gradient $\vec{G}_{prep}(t)$. For PC-MRI, $\vec{G}_{prep}(t)$ describes the bipolar waveform used for velocity sensitization. The integral term is defined as the gradient moment of order n, given as $\vec{m}_n(t) = \int_{t_0}^{t} \vec{G}_{prep}(t') \ (t'-t_0)^n \ \mathrm{d}t'$. Expanding the term $\varphi_{prep}(\vec{r},t)$ yields

$$\varphi_{prep}(\vec{r},t) = \varphi_r(\vec{r},t) + \varphi_v(\vec{r},t) + \mathcal{O}(t^2) \ , \tag{1.3}$$

where the phase terms are given by $\varphi_r(\vec{r},t) = \vec{k}_{prep}(t) \cdot \vec{r}(t_0)$ and $\varphi_v(\vec{r},t) = \vec{k}_{prep,v}(t) \cdot \vec{v}(\vec{r},t_0)$, where $\vec{k}_{prep}(t) = \gamma \int_{t_0}^{t} \vec{G}_{prep}(t') \, \mathrm{d}t'$ and $\vec{k}_{prep,v}(t) = \gamma \int_{t_0}^{t} \vec{G}_{prep}(t') \ (t'-t_0) \ \mathrm{d}t'$. In $\mathrm{t_{prep}}$, bipolar gradients are employed for velocity encoding which inherently have zero net area but a non-vanishing first moment. Therefore, $\varphi_r(\vec{r},t)$ vanishes due to $\vec{k}_{prep}(\text{end of } \mathrm{t_{prep}}) \equiv 0$ and spatial encoding is performed exclusively given $\vec{k}_{enc}(t)$ or in its discrete form, $\vec{k}_\kappa$. Therefore, for the remainder of this thesis, we denote $\vec{k}_{enc}(t) \mapsto \vec{k}(t)$ or in its discretized form $\vec{k}_{enc,\kappa} \mapsto \vec{k}_\kappa$ and $\vec{k}_{prep,v}(t) \mapsto \vec{k}_v(t)$.

The phase term $\varphi_{background}(\vec{r},t)$ denotes undesired phase contributions due to magnetic field inhomogeneities from differences in susceptibility of varying tissues or other undesired sources related to the sample while $\varphi_{system}(\vec{r},t)$ denotes contributions due to characteristics related to the MRI system itself. $\varphi_{background}(\vec{r},t)$ is assumed to be time-invariant but varying over time and space. The term $\varphi_{system}(\vec{r},t)$ arises from imperfections of the gradient system which are subject of Section 5. Assuming $\varphi_{system}(\vec{r},t) = 0$ and $\varphi_r(\vec{r}, \text{end of } \mathrm{t_{prep}}) = 0$, the desired net phase due to motion $\varphi_v(\vec{r},t)$ and the undesirable phase component $\varphi_{background}(\vec{r},t)$ can be distinguished by two separate acquisitions with

a difference in first moment of $|\Delta\overrightarrow{m}_1(t)|$. By complex division of the two data sets, which relates to subtraction of the signal phases, the phase component $\varphi_{background}(\vec{r},t)$ is cancelled out and $\varphi_{prep}(\vec{r},\text{ end of } \mathrm{t_{prep}}) = \varphi_v(\vec{r},\text{ end of } \mathrm{t_{prep}})$.

The first moment of velocity encoding $\overrightarrow{m}_1(t)$ during $\mathrm{t_{prep}}$ resulting from $\vec{k}_v(t)$ is set such that a bilinear transform between phase and velocity exists, namely

$$v_{enc} = \frac{\varphi_v(\vec{r},t)}{\gamma\ |\Delta\overrightarrow{m}_1(t)|}\Bigg|_{t=TE,\quad \varphi_v(\vec{r},TE)=\pi\ \forall\vec{r}\in\mathcal{V}} , \tag{1.4}$$

where v_{enc} is termed encoding velocity and is set slightly above the highest expected velocity in the sample[65] in order to maximize the velocity-to-noise ratio (VNR), which is defined in Section 5.9. Of note, the identical first moment difference $|\Delta\overrightarrow{m}_1(t)|$ can be achieved by either setting $\left|\vec{G}(t)\right| = \{G(t),\ 0\}$ (asymmetric encoding) or $\left|\vec{G}(t)\right| = \{-G(t)/2,\ G(t)/2\}$ (symmetric encoding) for the two acquisitions, respectively.

When bulk motion of magnetization is present within a voxel, the additional net phase $\varphi_v(\vec{r},t)$ is superimposed onto $\varphi_{prep}(\vec{r},t)$ corresponding to the sum over the velocity distribution of the magnetization. In theory, by varying $\vec{k}_v(TE)$, the bulk velocity distribution can be probed separately, resulting in the extended signal model

$$\begin{aligned} &d\big(\vec{k},\vec{k}_v,t\big) \\ &= \int_{\mathcal{V}} M_{xy}(\vec{r},t)\ \mathrm{e}^{\alpha(\vec{r},t)}\ \mathrm{e}^{\mathrm{j}\vec{k}(t)\cdot\vec{r}(t)}\ \mathrm{e}^{\mathrm{j}\vec{k}_v(t)\cdot\vec{v}(t)}\ \mathrm{e}^{\mathrm{j}\varphi_{background}(\vec{r},t)}\ \mathrm{e}^{\mathrm{j}\varphi_{system}(\vec{r},t)}\ \mathrm{d}\vec{r} \\ &+ \text{noise} , \end{aligned} \tag{1.5}$$

which is referred to as Fourier Velocity Encoding (FVE)[66] with the corresponding encoding vector $\vec{k}_v$. The special case for a single encoded and reference segment resulting in $|\Delta\overrightarrow{m}_1(t)| = \gamma\vec{k}_v(t)$ is included in the parameterization by velocity encoding vector $\vec{k}_v$.

1.4 Reconstruction Model

The reconstruction model assuming constant velocity $v(t) = v(t_0)$ during $\mathrm{t_{prep}}$, time invariant background phase and ideal system characteristics resulting in $\varphi_{system}(\vec{r},t) = 0$ is given by

$$S\big(\vec{r},\vec{k}_v\big) = \sum_{\kappa} d\big(\vec{k}_\kappa,\vec{k}_v\big)\ \mathrm{e}^{-\mathrm{j}\vec{k}_\kappa\cdot\vec{r}(t)} , \tag{1.6}$$

where $d\big(\vec{k}_\kappa,\vec{k}_v\big)$ is the complex k-space data given in the discrete $\vec{k}_\kappa,\vec{k}_v$-space and $\vec{r}(t)$ the spatial position. Any additional phase contribution to the signal $d\big(\vec{k}_\kappa,\vec{k}_v\big)$ during $\mathrm{t_{acq}}$, which is not accounted for in the reconstruction model by the k-space trajectory, disturbs the intended linear mapping between k-space vector $\vec{k}_\kappa$ and spatial position $\vec{r}(t)$ and leads to undesirable effects in the resulting image data. This also includes physiological motion such as beating of the heart or breathing motion. To prevent inconsistencies of the k-space data, PC-MRI scans are typically ECG triggered and performed within a breath hold or data are binned into several breathing motion states[67].

The blood flow itself, however, can also cause inconsistencies during data acquisition due to the motion of magnetization. Approaches to render spatial encoding due to $\vec{k}_\kappa$ insensitive to velocities at the echo time have been presented[68], which, however, result in

an undesirable increase of echo time. Of note, the compensation technique is based on the Taylor expansion of the time-dependent position of magnetization around a single time point. Rapidly changing flow conditions (including pulsatile flow) may limit the validity of the approximation. Also, it is evident that in order to achieve a desired zeroth gradient moment for spatial encoding, maximizing the gradient amplitude is preferred over increasing the time that the gradient is applied[69] given that the first gradient moment of rectangular gradient waveforms depends quadratically on time and only linearly on the amplitude.

While EPI acquisition has been used for 4D Flow MRI[17], the fact, that every pair of gradient lobes on the frequency encoding axis forms a velocity encoding waveform, gives rise to even/odd echo rephasing phenomena[70]. In addition, artifacts result from phase accrual in the direction of the phase encoding blips[71,72]. Section 2 comprises simulations and an experimental study of these effects for high flow regimes as found in aortic stenoses.

2 On the Limitations of Echo Planar 4D Flow MRI

Hannes Dillinger[1], Jonas Walheim[1], Sebastian Kozerke[1]

[1] Institute for Biomedical Engineering, University and ETH Zurich, Zurich, Switzerland

Published as: Dillinger H, Walheim J, Kozerke S. On the limitations of echo planar 4D flow MRI. *Magn Reson Med.* 2020;84(4):1806-1816. doi:10.1002/mrm.28236

2.1 Introduction

Increasing interest in 4D Flow MRI has emerged in recent years[27,73]. Numerous studies have investigated blood flow patterns[2,74], turbulent blood flow with focus on turbulent kinetic energy[12,75] and pressure loss in stenotic vessels[76,77] using 4D Flow MRI and have indicated the added value of these additional parameters.

Increased scan times, however, limit 4D Flow MRI scan protocols to be applied in clinical routine[73,78]. A number of recent studies have addressed this issue by using Compressed Sensing[67,79,80] and fast readout strategies such as echo-planar imaging (EPI)[17,81–90]. Results for EPI have revealed that the measured velocity field depends on the orientation of the phase and frequency encoding direction[91]. Of note, however, the majority of the work in this area[17,69,71,72,92–95] has focused on simple (convex) geometries and low velocity regimes. The high velocity regime is defined in case the displacement of magnetization in the velocity field between the time point of motion encoding (center of bipolar gradient) t_{ME} and the echo time t_{TE} is greater than the voxel width Δx,

$$\tilde{r}(t_{TE}) - \tilde{r}(t_{ME}) > \Delta x \tag{2.1}$$

The aim of the present work is to examine the effects of EPI and gradient echo (GRE) readout in phase-contrast imaging of high flow regimes and how they affect image resolution and displacement artifacts.

2.2 Theory

Starting with the general form of the k-space signal equation

$$d(t) = \int_{\mathcal{V}} \rho_0\big(\vec{r}(t)\big)\, \mathrm{e}^{\mathrm{j}\varphi(t)}\, \mathrm{d}\vec{r}'(t) \tag{2.2}$$

a time instant t is related to data in k-space $d(t)$. Here, $\rho_0\big(\vec{r}'(t)\big)$ denotes spatially dependent complex-valued transverse magnetization in the volume of interest $\mathcal{V}$. $\vec{r}'(t) = [r'_x(t)\vec{e}_x,\ r'_y(t)\vec{e}_y,\ r'_z(t)\vec{e}_z]^{\mathrm{T}}$ describes the time-dependent position vector of magnetization. The phase being acquired between the beginning of one readout t_0 and time point t by applying gradient is given by

$$\varphi(t) = \gamma \int_{t_0}^{t} \vec{G}(t') \cdot \vec{r}'(t')\, \mathrm{d}t', \tag{2.3}$$

where $\vec{G}(t') = [G_x(t)\vec{e}_x,\ G_y(t)\vec{e}_y,\ G_z(t)\vec{e}_z]^{\mathrm{T}}$ denotes the gradient waveforms in x-, y- and z-direction, respectively, and $\vec{G}(t') \cdot \vec{r}'(t') = [G_x(t)r'_x(t)\vec{e}_x,\ G_y(t)r'_y(t)\vec{e}_y,\ G_z(t)r'_z(t)\vec{e}_z]^{\mathrm{T}}$. In

phase-contrast MRI the Taylor series expansion of the position vector around time point t_0 is used according to

$$\vec{r}(t) = \underbrace{\vec{r}(t_0)}_{\vec{r}_0} + (t-t_0)\underbrace{\frac{\partial \vec{r}(t)}{\partial t}\Big|_{t=t_0}}_{\vec{v}(t_0)=\vec{v}_0} + (t-t_0)^2\frac{1}{2}\underbrace{\frac{\partial^2 \vec{r}(t)}{\partial t^2}\Big|_{t=t_0}}_{\vec{a}(t_0)=\vec{a}_0} + \mathcal{O}(t^3) \ , \tag{2.4}$$

which results in position, velocity and acceleration (plus higher order terms such as jerk) dependent phase terms

$$\begin{aligned}\varphi(t) = \underbrace{\gamma\vec{r}_0 \cdot \int_{t_0}^{t} \vec{G}(t') \ \mathrm{d}t'}_{\varphi_r(t)=\vec{k}(t)\,\cdot\,\vec{r}_0} + \underbrace{\gamma\vec{v}_0 \cdot \int_{t_0}^{t} \vec{G}(t') \ (t'-t_0) \ \mathrm{d}t'}_{\varphi_v(t)} \\ + \underbrace{\gamma\frac{1}{2}\vec{a}_0 \cdot \int_{t_0}^{t} \vec{G}(t') \ (t'-t_0)^2 \ \mathrm{d}t'}_{\varphi_a(t)} + \ \mathcal{O}(t^3) \ .\end{aligned} \tag{2.5}$$

One can identify the phase term for position encoding $\varphi_r(t)$ and additional phase terms $\varphi_v(t)$ and $\varphi_a(t)$ that give rise to misalignment in the imaging process. Equation (2.5) can be written in terms of the gradient moments

$$\varphi(t) = \gamma\left(\overrightarrow{m}_0 \cdot \vec{r}_0 + \overrightarrow{m}_1 \cdot \vec{v}_0 + \frac{1}{2}\overrightarrow{m}_2 \cdot \vec{a}_0\right) + \mathcal{O}(t^3) \ , \tag{2.6}$$

where the gradient moment of order n is defined as $m_n(t) = \int_{t_0}^{t} \vec{G}(t') \ t'^n \ \mathrm{d}t'$. Nulling a specific order of moments renders the sequence insensitive to these orders of motion at a single, specified time instant.

Flow compensation is an example of nulling the first moment $m_1(\mathrm{TE})$. For fast imaging methods such as EPI, motion compensation strategies have been studied which result in longer TE because of gradient moment requirements[94]. On the other hand, keeping TE short has been shown to reduce artifacts in phase-contrast imaging[96].

For monitoring the phase deviation during readout, an error term $\tilde{\varphi}_r(t)$ is defined as

$$\tilde{\varphi}_r(t) = \ \varphi(t) - \varphi_r(t) = \varphi_v(t) + \varphi_a(t) \ , \tag{2.7}$$

which sums up the phase contributions for first and second order uncompensated gradient waveforms. Consequently, the misalignment in meters can be calculated as

$$\Delta\tilde{r}_i(t) = \frac{\Delta x}{2\pi}\left[\gamma\int_{t_0}^{t} \vec{G}(t') \cdot \vec{r}_i(t') \ \mathrm{d}t' - \gamma\vec{r}_{0;i} \cdot \int_{t_0}^{t} \vec{G}(t') \ \mathrm{d}t'\right] \ , \tag{2.8}$$

where Δx represents the Fourier resolution in x-, y- or z-direction, respectively. The continuous form of Equation (2.2) can be approximated in discrete form as

$$\tilde{d}(t) = \sum_{i=1}^{N} \rho_0\big(\vec{r}_i(t)\big) \ \mathrm{e}^{\mathrm{j}\gamma\int_{t_0}^{t} \vec{G}(t')\cdot\vec{r}'(t') \ \mathrm{d}t'} \ , \tag{2.9}$$

where N is the number of traced isochromats and $\tilde{d}(t) \approx d(t)$ for large N.

Displacement artifacts

Let us assume that the velocity encoding and readout happens at discrete time points t_{ME} and t_{TE} as outlined in Figure 2.1A. The phase $\varphi(t_{ME})$ is imaged at position $\vec{r}(t_{TE})$ – a "snapshot" of the velocity field given by $\varphi(t_{ME}) \propto \vec{v}(\vec{r}(t_{ME}))$ translated by the movement of the magnetization between time instants t_{ME} and t_{TE}. The Point Spread Function (PSF) is not modulated but only shifted. This displacement artifact has been examined in Steinman et al.[91] for low flow velocities. The present work aims to provide an estimate of displacement artifacts occurring in high velocity regimes.

Phase accumulation artifacts

Motion during readouts with finite time duration results in broadening and shifting of the PSF[94] as outlined in Figure 2.1B. The linearization given in Equation (2.4) is only valid in a range around t_0.

Considering Equation (2.5), $\varphi_v(t)$ and $\varphi_a(t)$ both represent phase terms that (if unequal to zero) result in artifacts. For the oscillatory gradients used in frequency encoding direction in EPI, velocity-dependent phase shifts at every odd echo occur[94]. On the other hand, in phase encoding direction unipolar blips are used, therefore phase shifts due to motion accumulate over time and result in modulation of the PSF.

By increasing TE while keeping the duration of readout constant, artifacts due to displacement will be increased. In contrast, the modulation of the PSF is dependent on phase accumulation depending on the readout strategy. In this work, phase accumulation of EPI is investigated.

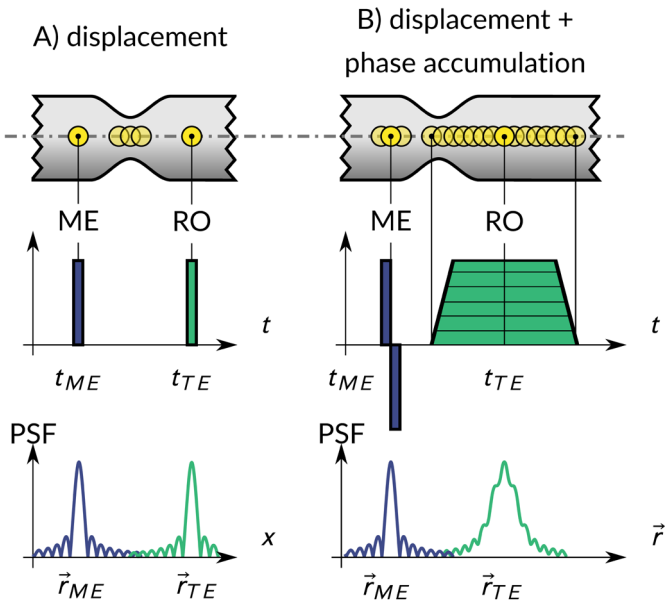

Figure 2.1: A) Assuming instantaneous readout (RO) results in displacement artifacts without blurring of the PSF. The amount of misregistration is given by the ow velocity and the time duration between motion encoding (ME) and echo time (TE). B) Finite time readouts result in additional broadening of the PSF.

2.3 Methods

In silico study

An outline of the simulation framework is provided in Figure 2.2. Further information about the simulation setup can be found in the Supplementary Material section online. An example script is available online at https://osf.io/q47s8.

Simulation of Data Acquisition

In cardiac-triggered 4D Flow MRI, only a subset N_{seg} of all required k-space profiles is acquired per heartbeat[78]. The remaining profiles are acquired during subsequent heart beats, at the exact same time delay from the R peak of the ECG signal. This results in every segment having the same initial conditions for magnetization and position within the R-R interval. If interleaved acquisition with cardiac triggering is assumed, respective subset profiles (k_x, k_y) are acquired one after another in k_z direction within one time frame (compare Figure 2.2A) as (k_y, k_z) directions are phase encoded for example. This renders the acquisition along k_z independent of (k_x, k_y) dimensions besides that the acquisition starts at a different time point within the time frame. In the present study, the velocity field is assumed to be stationary and hence we derive the same initial conditions for every (k_y, k_z) profile. Of note, this enables us to restrict the simulation to 2D in (k_x, k_y) without loss of generality.

CFD Simulation

A computational fluid dynamic (CFD) simulation using the Reynolds Averaged Navier Stokes (RANS) approach was performed on a stenotic U-bend geometry (50% stenosis, cosine shaped[97] using OpenFOAM v1712). A parabolic inlet profile with 1 m/s, no-slip wall and zero-gradient boundary condition for the velocity at the outlet was applied. The simulation resulted in a steady velocity vector field $\vec{v} \in \mathbb{R}^{2\times\Omega}$, given at the CFD grid points of domain Ω which is given as the $(x, y \in [-FOV_{x,y}/2,\ FOV_{x,y}/2,\ z = 0]$ plane. The maximum velocity downstream of the stenosis was 2.2 m/s.

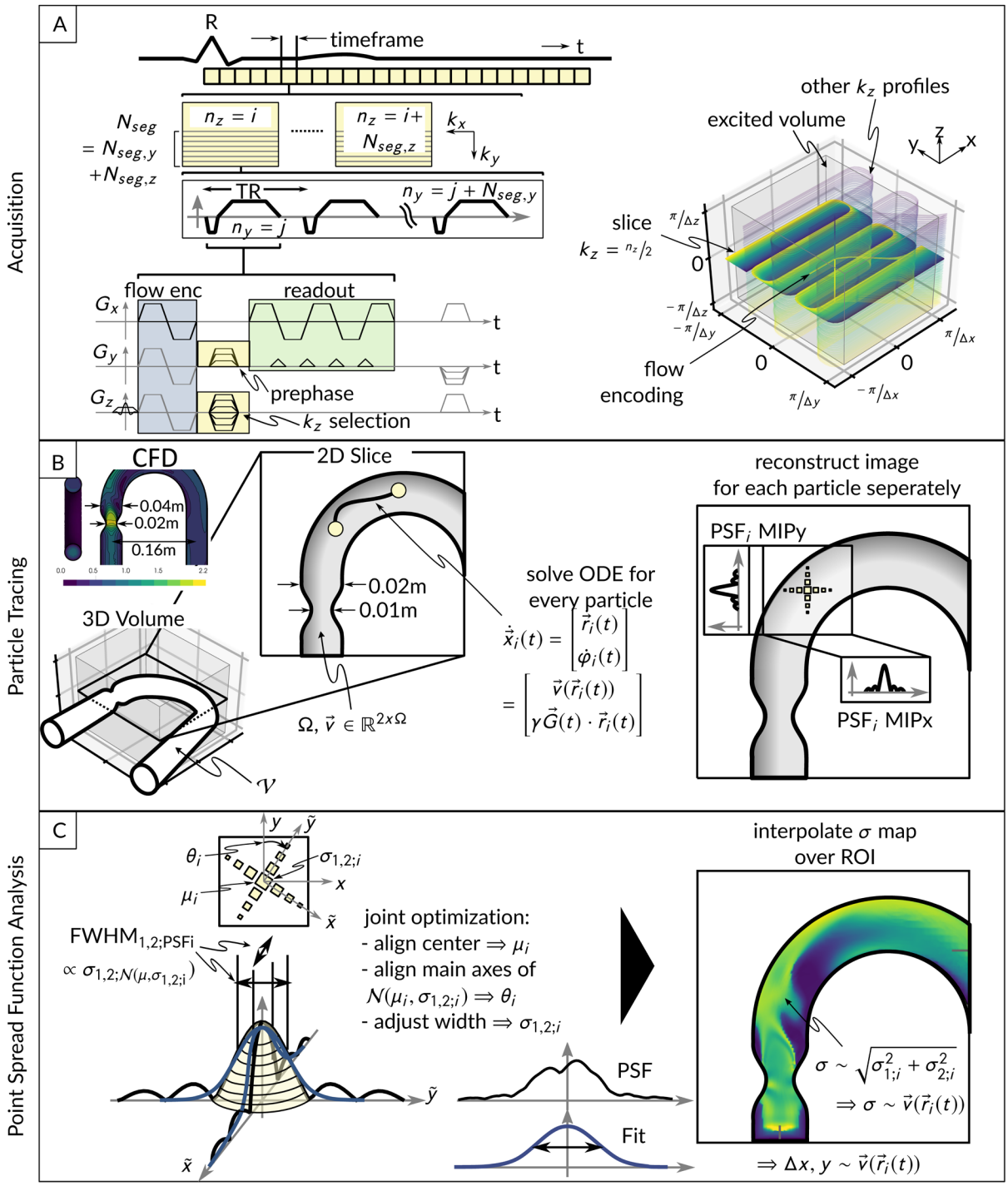

Figure 2.2: Schematic depiction of the simulation framework. A) In 4D Flow, interleaved acquisition is used to acquired data over several R-R intervals. A 3D EPI trajectory is defined. B) A single k_z plane (ROI) is selected by extracting the central slice. On the ROI, massless tracer particles are seeded for which the state vector Equation 10 is solved and images are reconstructed. C) To quantify the PSF, a Gaussian fitting process is used. This results in a spatially varying effective resolution map which depends on the trajectory taken by the particle during readout.

Particle Tracing

Particles ($N = 10771$) were seeded on a plane parallel to the centerline of the U-bend. For every mass-less tracer particle i, the state vector differential equation

$$\dot{\vec{x}}_i(t) = \begin{bmatrix} \dot{\vec{r}}_i(t) \\ \dot{\varphi}_i(t) \end{bmatrix} = \begin{bmatrix} \vec{v}(\vec{r}_i(t)) \\ \gamma \vec{G}(t) \cdot \vec{r}_i(t) \end{bmatrix} \tag{2.10}$$

was solved using the mean velocity vector field $\vec{v}$ output from the RANS simulation. A Dormand-Prince method readily available in MATLAB R2017b (The MathWorks, Natick, MA) was used to solve the ODEs in parallel. The initial conditions were set as $\vec{x}_0 = \vec{x}(t_0) = [\vec{r}_0, 0]^{\mathrm{T}}$, where $\vec{r}_0 = \vec{r}(t_0)$ denotes the initial seeding position. $\vec{r}_0$ is defined by regularly seeding particles inside the field-of-view (FOV). At evaluation time points given by the trajectory, it was ensured that there was at least one particle per pixel. To mimic a zero-slip condition at the boundary of Ω, particles' velocities were set to zero outside domain Ω (while phase integration was continued).

Displacement Artifact Imaging

For simulating displacement artifacts exclusively, motion encoding and readout were assumed to happen instantaneously at respective time points of motion encoding t_{ME} and echo time t_{TE}. This was performed by utilizing the solution to the first line in Equation (2.10), evaluating the vector field at $\vec{v}(\vec{r}_i(t_{ME}))$ and mapping it to position $\vec{r}_i(t_{TE})$ for every particle. The scattered velocity values at $\vec{r}_i(t_{TE})$ were interpolated to the image grid given by the FOV and the image resolution using natural neighbor interpolation[98]. As the imaging process happened instantaneously, the PSF was not altered in shape but shifted.

Sampling Trajectories

As the mapping $t \mapsto d(t)$ is known by generating the k-space trajectory, the differential Equation (2.10) was solved for every entry in the data matrix, resulting in a data point $d(t) \in \mathbb{C}$ given by Equation (2.9). Every entry in the data matrix was related to a k-space point by the transformation $d(t) \mathrel{\widehat{=}} d(k_x, k_y)$ for $t \in [t_0, t_1, \ldots, t_{nx \times ny}]$. The coil sensitivity was assumed to be constant throughout the FOV. Gradient waveforms were generated considering gradient strength and slew rate limits of current MRI scanners of 30 mT/m and 195 T/m/s, respectively. Trajectories were generated using standard GRE Cartesian readout ($n_s = 1$ profile at a time) and EPI ($n_s = 5$ profiles). The initial conditions were reset to $\vec{x}_0$ after each shot. A 0.1×0.1 m^2 FOV with a resolution of 1×1 mm^2 was simulated. The first moment of the bipolar gradient was calculated according to $v_{enc} = 2.2$ m/s for the encoded measurement. Corresponding echo times (t_{TE}) were 2.1 ms and 4.3 ms for Cartesian and EPI readout, respectively. Trajectories in k-space are shown in Supporting Information Figure S1 online. Phase unwrapping was applied for all velocity plots[99].

PSF Calculation

As the PSF shape was blurred by growing ghosts for flow in frequency and phase encoding direction, a Gaussian fitting approach was chosen instead of characterizing the Full-Width-at-Half-Maximum (FWHM) directly. This enabled a characterization of non-sinc PSFs and comparison to the undisturbed PSF. For every particle $i \in \{1, 2, \ldots, N\}$, an image was reconstructed containing exclusively particle i. The Fourier space data matrix was increased 5-fold by zero padding keeping the image ratio constant. A 2D Gaussian function was aligned with the main axes of the magnitude image and scaled accordingly in an optimization process. Incorrect fitting results have been manually removed.

Exemplary fitting results can be found in the Supporting Material Section online, Supporting Information Figure S2-S4.

In vitro study

4D Flow MRI data of a steady flow phantom[100] driven by a centrifugal pump (BG-GP 636, Einhell Germany AG, Germany) was acquired on a 3T Philips Ingenia system (Philips Healthcare, Best, the Netherlands) using standard 4D Flow MRI GRE and EPI readout. A schematic of the flow phantom setup is shown in Figure 2.3. The list of scan parameters can be found in Table 2.1. Encoding constants were $v_{enc} = 150$ cm/s per axis and an additional reference measurement with $v_{enc} = 0$ cm/s. All measurements were performed using a 32-channel receiver coil. The data was reconstructed using MRecon (GyroTools LLC, Zurich, Switzerland).

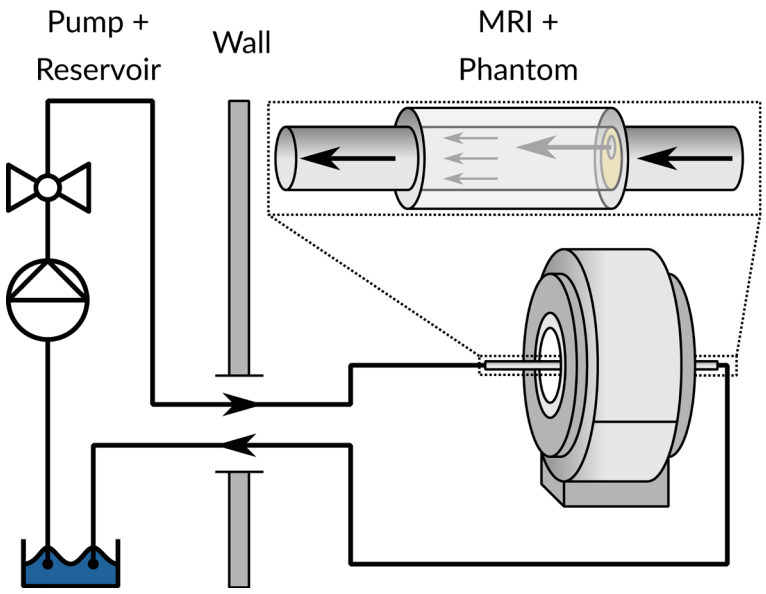

Figure 2.3: Schematics of the flow phantom setup used in the in vitro experiment. The hydraulic circuit consists of a pump, a valve connected (placed outside the scanner room) and a water reservoir connected to the phantom. The main flow direction is orientated along the main magnetic field of the scanner.

Table 2.1: In vitro scan parameters.

Method	**Fold-Over**	**FOV [mm³]**	**Rec. Size**	**Rec. Resol. [mm³]**	**TE [ms]**	**Scan Time**
GRE	FH	78 x 350 x 301	288 x 288 x 50	1.2 x 1.2 x 1.6	2.25	3.2 min
GRE	RL	78 x 301 x 350	288 x 288 x 50	1.2 x 1.2 x 1.6	2.25	3.2 min
EPI5	FH	78 x 350 x 301	288 x 288 x 50	1.2 x 1.2 x 1.6	3.17	47 s
EPI5	RL	78 x 301 x 350	288 x 288 x 50	1.2 x 1.2 x 1.6	3.3	49 s
EPI11	FH	78 x 350 x 301	288 x 288 x 50	1.2 x 1.2 x 1.6	5.09	34 s
EPI11	RL	78 x 301 x 350	288 x 288 x 50	1.2 x 1.2 x 1.6	5.2	35 s

2.4 Results

Simulation

Displacement Artifacts

Figure 2.4 compares the displacement artifact for time points of motion encoding (ME), end of prephaser (PP) and echo time (TE) for EPI5 readout. As readout was assumed to happen instantaneously, the velocity field is given by the translated encoded velocity field. For the timepoints of motion encoding, end of prephaser and echo time, displacements of the maximum velocity of $\Delta c(t_{ME}) = 0.33$ mm, $\Delta c(t_{PP}) = 2.29$ mm and $\Delta c(t_{TE}) = 7.30$ mm along the centerline are measured.

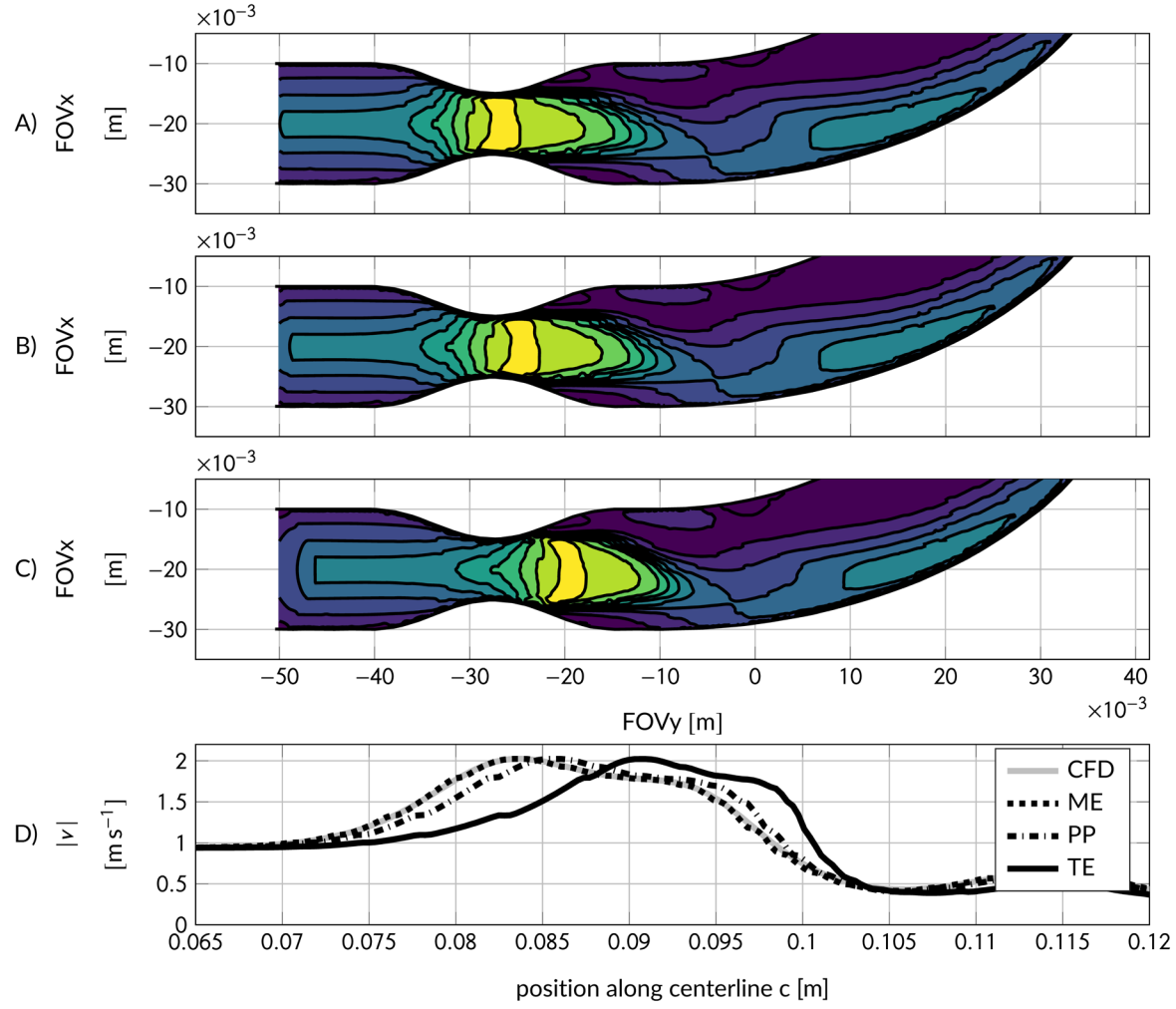

Figure 2.4: In silico velocity magnitude for instantaneous readout assuming EPI5. Time points are A, motion encoding (ME), B, end of prephaser (PP) and C, echo time (TE). D, shows the velocity along the centerline for given time points.

Displacement and Phase Accumulation Artifacts

Considering an example particle trajectory, Figure 2.5 shows the misregistration $\tilde{r}_{x,y}(t)$ evaluating Equation (2.8) which results from the phase accumulation of the EPI train and blips, respectively.

The reconstructed PSF for a single particle (trajectory depicted in Figure 2.5) is shown in Figure 2.6 for phase encoding direction aligned with the main flow and MIP along x and y, respectively. Additional plots can be found in the Supplementary section online. Both misregistration due to the longer TE as well as modulation of the PSF dependent on the maximum velocity is seen for EPI5.

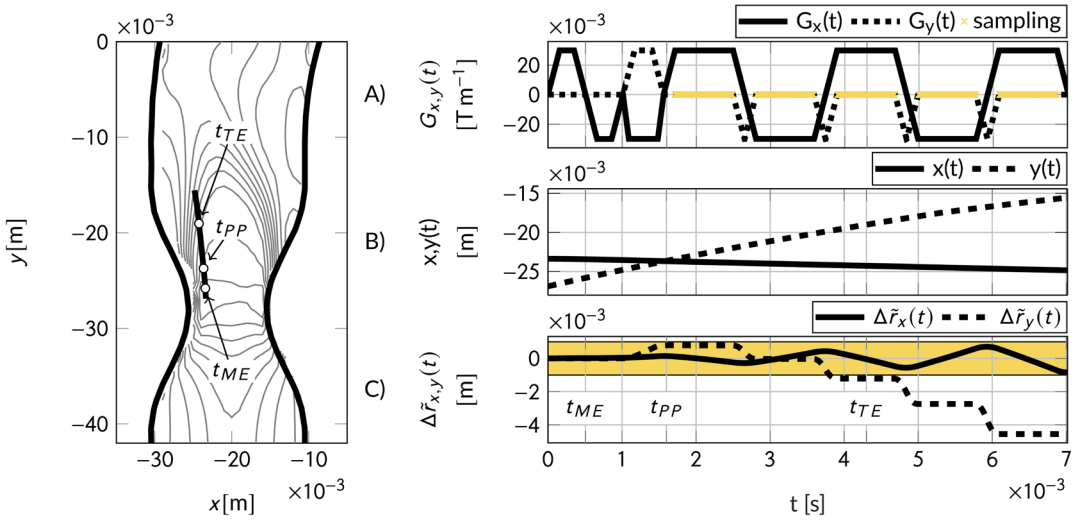

Figure 2.5: Exemplary in silico particle trajectory and resulting phase accumulation. The main flow is aligned with phase encoding direction. Left: The particle crosses several velocity contour lines which are not linearly spaced, therefore not only velocity but also higher order terms increase the accumulated phase shift during readout. Right: A, Gradient signals in x- and y-directions for one shot with respective time points for motion encoding (ME), end of prephaser (PP) and echo time (TE). B, Particle position over time. C, Misalignment due to phase accumulation.

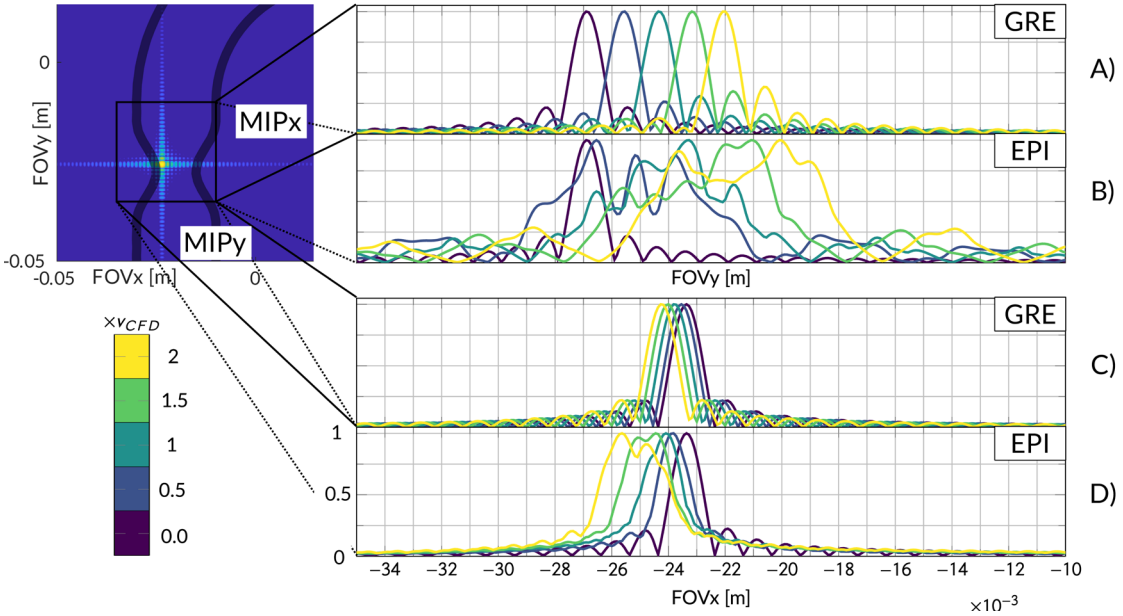

Figure 2.6: Normalized in silico PSF for exemplary particle as in Figure 5 with simulated velocity multiplied by factor $\times v_{CFD}$, main flow direction aligned with phase-encoding direction. A and B, showing the maximum intensity projection (MIP) along the x direction for GRE and EPI, respectively. C and D, show MIP along the y-direction for GRE and EPI, respectively. The PSF shift along FOVx and FOVy is given by the particle motion and varies with the factor $\times v_{CFD}$ and TE (different for GRE and EPI).

In Figure 2.7, depending on the alignment of the main flow direction along either frequency or phase encoding direction, artifacts are observed for EPI readout while the GRE results do not depend on the orientation. For EPI readout, especially at the transition boundary from the jet core to the lower velocity regime (where accelerations both in x- and y-direction are present), differences in velocities from ground truth as high as 1 m/s are seen. Reconstructed in silico images for both velocity components v_x and v_y can be found in Supplementary Information Figure S5 and Supplementary Information Figure S6 online.

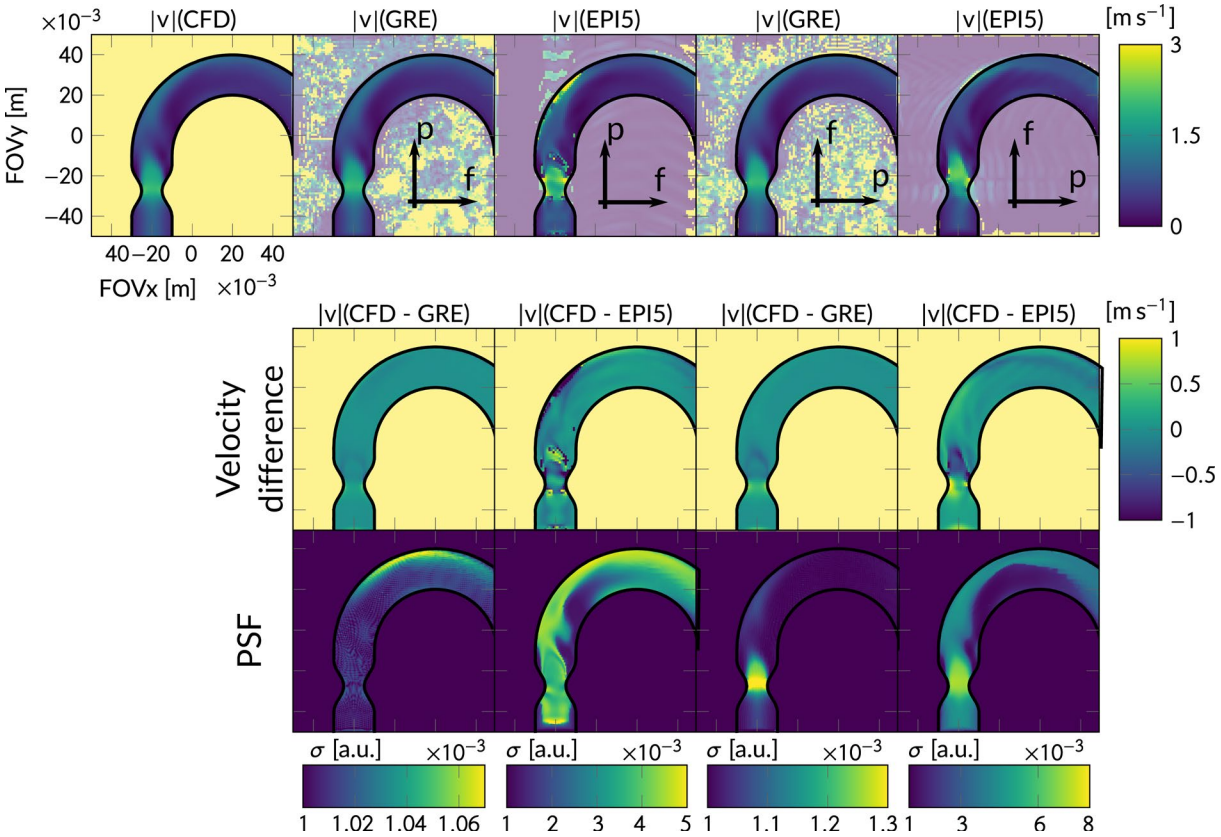

Figure 2.7: Reconstructed in silico images and width of PSF for GRE and EPI5. Either phase (p) or frequency (f) encoding direction is aligned with the main flow. Flow magnitude $|v| = \sqrt{v_x^2 + v_y^2}$ *is presented and difference images* $|v|(CFD - GRE/EPI)$ *show an over- and underestimation for positive and negative values, respectively. The PSF width reveals spatially varying resolution as a function of the velocity field. Background has been masked by an alpha value of 0.3. CFD: ground truth CFD solution, GRE: Gradient echo, EPI5: EPI factor 5 readout.*

The PSF results shown in bottom row of Figure 2.7 are characterized by $\sigma = 1/\sqrt{\Delta x^2 + \Delta y^2}\ \sqrt{\sigma_1^2 + \sigma_2^2}$ where $\sigma_{1,2}$ denote the standard deviation along the main axes of a 2D Gaussian function fitted to the reconstructed PSF. Since there exists no closed form conversion between Gaussian and Sinc function, the parameter PSF is to be interpreted as arbitrary unit. The PSF width for EPI5 readout was increased by a maximum factor of 5 and 8 for aligning the flow direction along frequency and phase encoding direction respectively in contrast to GRE for which it was found to be independent of the main flow direction.

In vitro experiment

Differences in the jet shape and length for EPI and GRE readout are compared in Figure 2.8. For better interpretability, the FOV was divided into 30 sectors, which resulted in 18 ROI sectors. A histogram analysis reveals that not only higher velocities were imaged at a position further downstream for EPI5 (i.e. longer TE) but also the velocity distribution was shifted towards higher velocities compared to GRE. This results in an overestimation of the velocity field after the stenosis for EPI readouts. The mean difference of the velocity magnitude inside the ROI between different orientations of the

fold-over direction was 0.1284 m/s for EPI5 compared to 0.1045 m/s for GRE. A comparison of EPI11 to GRE and EPI5 can be found in Supplementary Material section online, Supplementary Information Figure S7 and Supplementary Information Figure S8. Proton density images for the experiment are shown in Supplementary Information Figure S9.

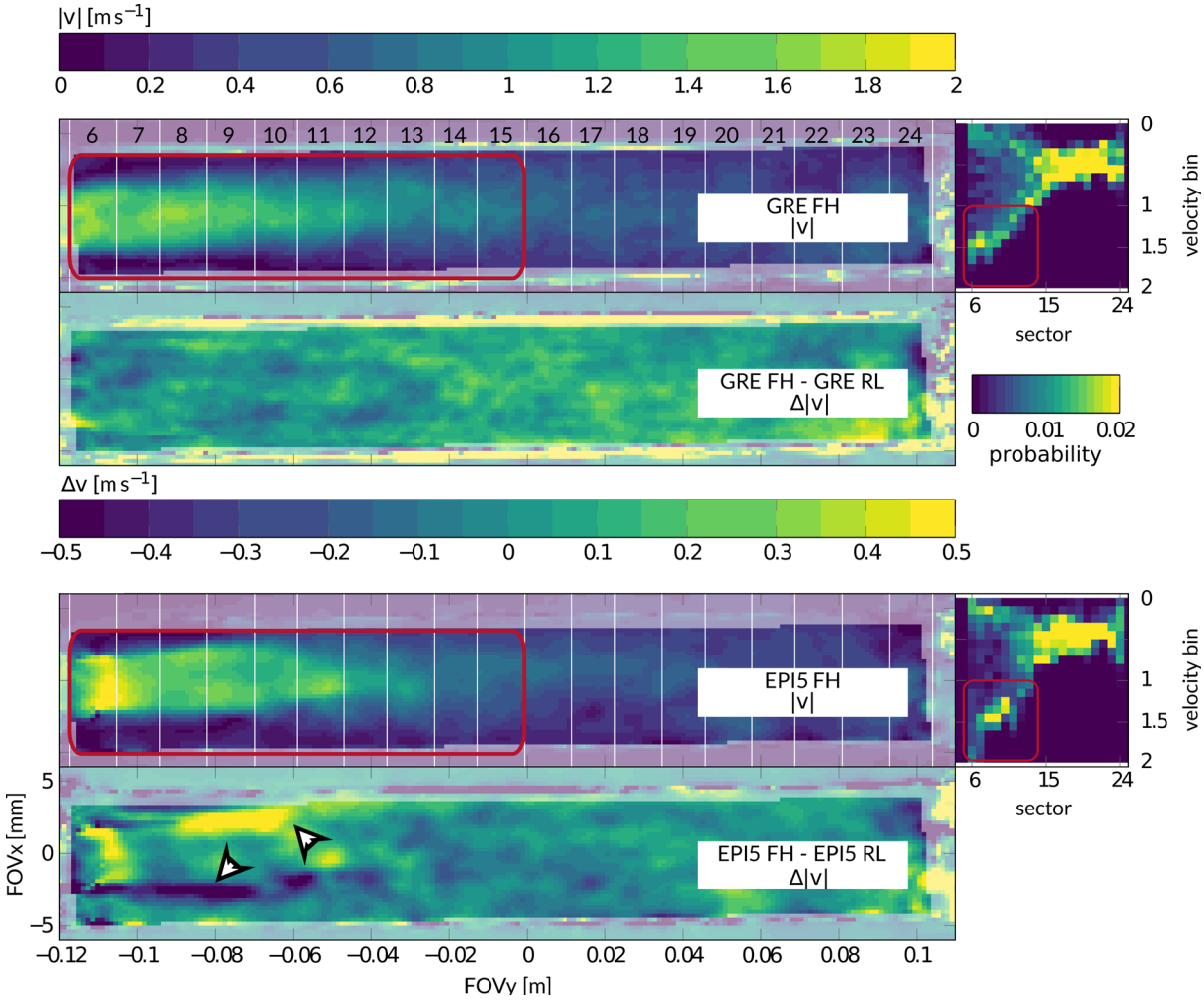

Figure 2.8: In vitro velocity magnitude images (|v|) for GRE and EPI5 with phase encoding direction aligned with main flow. The velocity histogram using 32 equally spaced bins ($0.05s^{-1}$) for each sector is shown at the right for GRE FH and EPI FH. Difference images ($\Delta|v|$) are given as the difference in velocity magnitude between phase- and frequency-encoding direction aligned with main flow, respectively. The jet shape and extent is modulated for EPI compared to GRE. For EPI5, velocity differences between orientations can be found at areas of high acceleration or shear (short white arrows).

2.5 Discussion

In this work, flow artifacts in 4D Flow MRI using GRE and EPI readout have been quantified for realistic high flow conditions. The analysis was based on CFD velocity data as input into a comprehensive phase-contrast flow simulation using a Lagrangian Particle Tracing approach[36]. Based on MRI simulations using realistic imaging parameters, it is concluded that longer TE results in considerable velocity misregistration. In contrast to

GRE, EPI readouts are additionally associated with spatially varying broadening of the point spread function.

By using CFD data and by implementing k-space trajectories as implemented on current MR systems, ground truth and the imaged velocity vector field could be assessed in a quantitative manner. The results confirmed that displacement artifacts occur for long TE[91]. Moreover, phase accumulation due to motion-sensitive readout strategies disturbs the resulting image[71]. The PSF modulation for EPI5 was found to reduce image resolution locally up to a factor of 8 times compared to GRE. The general picture emerging from the analysis is that even for simple geometries in which the flow direction turns by 90° at some point, the resulting velocity image depends on the orientation of the phase encode directions and hence the imaging volume.

It has been demonstrated that using GRE with short echo times[69] can reduce in plane motion artifacts. The in vitro data shown in Figure 2.8 provide data revealing that the velocity histogram is not only blurred in flow direction but also velocity is overestimated downstream of the stenosis. This finding has implications since the maximum velocity is an important criterion in classification of aortic stenoses[101].

One limitation of the current study is the restriction to steady flow. However, the absence of pulsatile flow avoids other confounding effects which have not been the focus of the present work. Instead, it aims at the investigation of displacement and phase accumulation artefacts during high flow, i.e. worst-case scenarios. A recent study[102] found EPI factor 3 in vivo compared GRE readout inferior but lacks the availability of ground truth. The present work on the other hand, utilizes CFD ground truth data. Eddy-current effects of real MRI systems have been neglected (which can give rise to significant background phase errors (see Busch et al.[103]). No spin history effects have been simulated as the particles' phases were assumed to be zero at the beginning of every shot. Inflow effects (or "washout") in slice direction can be interpreted as displacement artefacts as magnetization is transported out of the excited volume (described for Spin Echo in Axel et al.[104]). This would result in displacement artifacts and decreasing signal amplitude.

Stack-of-radials[105], 3D radials[60] or spiral[61] readout strategies have been proposed for phase-contrast MRI. Conceptually, radial readouts can be compared to GRE in terms of readout durations while spiral readouts might be compared to EPI. The amount of displacement artifacts depends on the trajectory of magnetization between the timepoint of motion encoding and echo time. The amount of PSF modulation, on the other hand, will differ depending on the k-space trajectory and hence Spiral and EPI will show differences in phase accumulation artifacts. The assessment of PSF modulation in spiral readouts is subject of ongoing work.

Finally, as the particle density and trajectory simulation time step were limited by computational resources, the effects investigated are bound to these space and time scales. Future studies will have to investigate EPI for turbulence encoding and smaller, more complex flow structures.

2.6 Conclusion

4D Flow MRI using EPI readout results not only in considerable velocity misregistration but also in spatially varying degradation of resolution. The proposed work indicates that EPI is inferior to standard GRE for 4D Flow MRI.

3 Encoding and Decoding of Random Motion in MRI

In Section 1, for the MR signal model for velocity encoding it was assumed that, first, the Taylor expansion of motion up to a given order is valid around timepoint t_0 and, second, that velocities within a given voxel are equal.

3.1 Continuous Process of Motion Encoding

The first assumption inherently connects the duration of motion encoding gradients to the time duration over which the Taylor expansion can be considered valid. Therefore, if the motion encoding duration is much shorter than the correlation time of motion of isochromats in a voxel, the process of motion encoding can be considered a discrete event and results in a phase accrual corresponding to the velocity within the voxel. The second assumption above must be relaxed when a velocity distribution is present within a voxel and hence the phase accrual then corresponds to the mean of the velocity distribution.

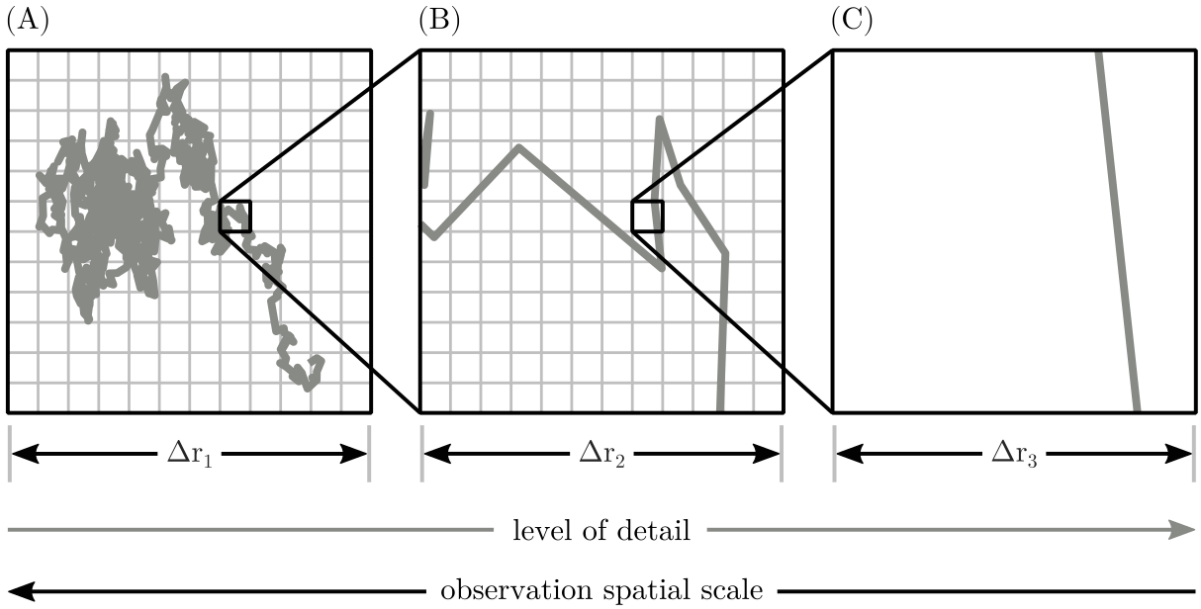

Figure 3.1: Spatial observations scales related to a spatial trajectory of an exemplary random motion process. (A) For a voxel size of Δr_1, a material point remains in the voxel but its spatial position varies randomly. The motion is referred to as intravoxel motion. (B) For a voxel size $\Delta r_2 \ll \Delta r_1$, random directional changes are still observed. (C) For a voxel size $\Delta r_3 \ll \Delta r_2$, the motion is coherent within the spatial observation scale and can be considered deterministic.

If the time scale of motion of isochromats is on the order of the duration of the motion encoding gradient waveform, the encoding process itself must be regarded a continuous process. An example of the relation of spatial motion and observation scales are depicted in Figure 3.1.

3.2 Amplitude Modulation Function

A comparison of the spatial scale of isochromats (H_2O molecule size $3\text{Å} \approx 0.3\text{nm}$) and typical voxel sizes on the order of millimeters illustrates the impossibility of observing and encoding the motion of isochromats separately. In addition, the timescale at which

random motion of isochromats happens may be shorter than the motion encoding time. Therefore, a statistical description of isochromat motion must be employed.

The net phase due to motion of isochromats is given by the ensemble average[106] of magnetization. Assuming a Gaussian velocity distribution within the voxel, the resulting signal is given by

$$E(\vec{r},t) \propto \exp\left[\underbrace{-\mathrm{j}\,\gamma \int_0^t \vec{q}(t') \cdot \overline{\vec{v}(\vec{r},t')}\ \mathrm{d}t'}_{\varphi_v(\vec{r},t)} \right. \\ \left. \underbrace{-\ \frac{1}{2} \int_0^t \int_0^t \vec{q}(t)\ \vec{q}(t+\tau)\ \overline{\vec{v}(\vec{r},t)\ \vec{v}(\vec{r},t+\tau)}_{LC}\ \mathrm{d}\tau}_{\alpha(\vec{r},t)} \right] , \tag{3.1}$$

which can be interpreted as the phase component $\varphi_v(\vec{r},t)$ as defined in Section 1.3 which is given by the mean of bulk motion of a velocity distribution $\overline{\vec{v}(\vec{r},t')}$ and an amplitude modulation function $\alpha(\vec{r},t)$ given by the autocorrelations of the time integral of the velocity encoding gradient $\vec{q}(t) = \gamma \int_0^t \vec{G}_{prep}(t')\ \mathrm{d}t'$ and the autocorrelation of the instantaneous magnetization motion $\vec{v}(\vec{r},t)$. Of note, the definition of $\vec{q}(t)$ differs from the notation used in Dillinger et al.[107] to be consistent with works by Tuch[108]. The index LC denotes the location correlation and evaluates the standard deviation in time of $\vec{v}(\vec{r},t)$ as in $\sigma^2 = \langle w^2 \rangle - \langle w \rangle^2$. The volume integral over the volume of interest has been omitted.

Given the amplitude modulation function

$$\alpha(\vec{r},t) \propto\ -\frac{1}{2} \int_0^t \int_0^t \vec{q}(t)\ \vec{q}(t+\tau)\ \overline{\vec{v}(\vec{r},t)\ \vec{v}(\vec{r},t+\tau)}_{LC}\ \mathrm{d}\tau\ , \tag{3.2}$$

the existence of two timescales is apparent, relating the time scale of motion encoding due to $\vec{q}(t)$ to the time scale of the motion of magnetization itself. Depending on the autocorrelation of the time integral of the encoding gradient $\vec{q}(t)\ \vec{q}(t+\tau)$ (autocorrelation integral has been omitted for brevity), two encoding regimes can be differentiated. As depicted in Figure 3.2, relating the time scale of an exemplary random process to a typical velocity encoding gradient waveform, results in a continuous process of motion encoding, considering the isochromat trajectory during time span t_1 to t_2 and t_2 to t_3. In the limit of short gradient pulses, however, the mean squared distance (MSD) is encoded in $\alpha(\vec{r},t)$ and solely $\vec{r}(t_1)$ and $\vec{r}(t_2)$ are of importance[109,110].

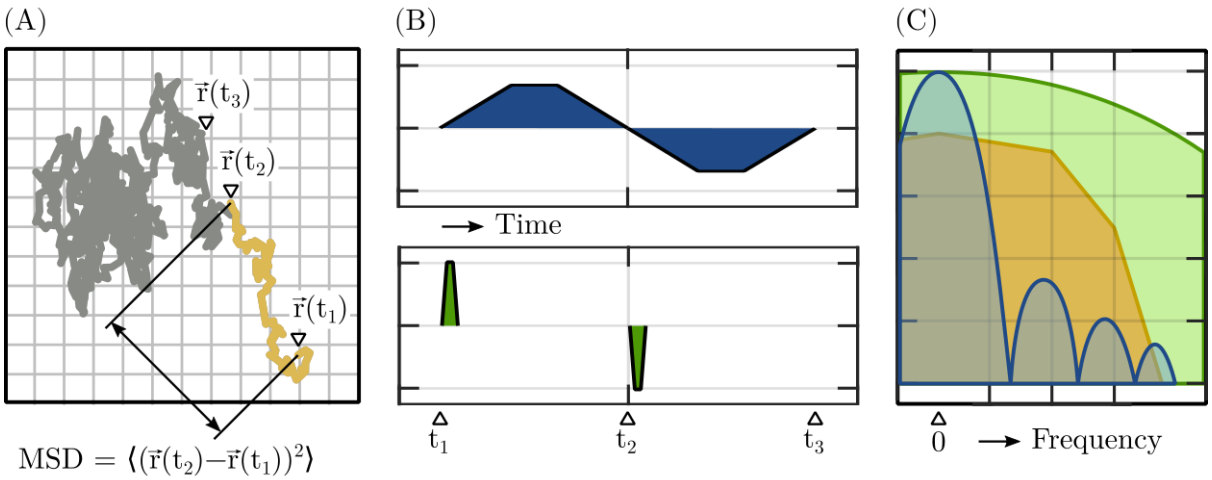

Figure 3.2: (A) Spatial trajectory $\vec{r}(t)$ of an exemplary random process at time points t_1, t_2 and t_3. (B) Time points are related to the beginning, maximum first moment and the end of the motion encoding gradient waveform, respectively. Upper row: bipolar gradient resulting in continuous motion encoding process. Lower row: short gradients resulting in displacement encoding of the mean squared distance depicted in (A). (C) Spectral depiction of gradients (colors as in (B)) related to spectrum of the random process (brown). Spectral coverage of the long duration gradient (blue) may be insufficient to encode high frequency content as opposed to the short gradient pulses (green). The spectrum of the random process can vary spatially, temporally and is dependent on the process itself.

Of note, a unique property of motion encoding is its possibility to encode random motion across several orders of scales. Timescales in diffusion processes[111] or in turbulent flow[112], for example, may differ by three orders of magnitude. Nevertheless, by adjusting gradient waveforms accordingly, time scales of encoding can be tuned to time scales of motion within given limits.

3.3 Extension of the Reconstruction Model

The reconstruction model defined in Equation (1.6) is extended by employing the zeroth gradient moment during t_{prep} given as $\vec{q}(t)$ as additional parameter

$$S(\vec{r},\vec{k}_v,\vec{q}) = \sum_{\kappa} d(\vec{k}_\kappa,\vec{k}_v,\vec{q})\ \mathrm{e}^{-\mathrm{j}\vec{k}_\kappa\cdot\vec{r}(t)}\ , \tag{3.3}$$

where traversing through $\vec{q}$-space is given by the corresponding $\vec{q}$ sample points. As encoding due to $\vec{q}$ results in an amplitude contribution to $d(\vec{k}_\kappa,\vec{k}_v,\vec{q})$, the amount of desired signal loss due to $\alpha(\vec{r},t)$ can be controlled by the gradient amplitude $\vec{G}_{prep}(t)$ for a spatially constant correlation function $\overline{\vec{v}(t)\ \vec{v}(t+\tau)}_{LC}$. Similar to Section 1.3, the special case for a single encoded and reference segment resulting in probing a single point in $\vec{q}$-space is included in the parameterization by $\vec{q}(t) = \gamma\int_0^t \vec{G}_{prep}(t')\ \mathrm{d}t'$ with $\vec{G}_{prep}(t)$ being the bipolar gradient employed for velocity encoding.

3.4 Correlation Timescales in Turbulent Flows

As turbulent flows may occur in patients with aortic disease[113] but also in healthy controls[114], quantification of turbulent parameters is of great clinical interest.

In order to statistically describe turbulent flow fields, the Reynolds decomposition can be applied to the instantaneous velocity $\vec{v}(t)$, resulting in a mean $\bar{\vec{v}}$ and fluctuating part $\vec{v}'(t)$ as in

$$\vec{v}(t) = \bar{\vec{v}} + \vec{v}'(t) \ . \tag{3.4}$$

The mean $\bar{\vec{v}}$ can be defined as the time average over time interval T for statically stationary flows[112],

$$\langle \vec{v}(t) \rangle_T = \frac{1}{T} \int_t^{t+T} \vec{v}(t') \ \mathrm{d}t' \ , \tag{3.5}$$

or as ensemble average if the flow experiment "*can be repeated or replicated N times*"[112]

$$\langle \vec{v}(t) \rangle_N = \frac{1}{N} \sum_{n=1}^{N} \vec{v}^{(n)}(t) \ , \tag{3.6}$$

where $\vec{v}^{(n)}(t)$ corresponds to the resulting flow field of the nth realization or as spatial averaging "*given on a cubic domain of side* $\mathcal{L}$"[112] by

$$\langle \vec{v}(t) \rangle_{\mathcal{L}} = \frac{1}{\mathcal{L}^3} \int_0^{\mathcal{L}} \int_0^{\mathcal{L}} \int_0^{\mathcal{L}} \vec{v}(\vec{r}, t) \, \mathrm{d}x \ \mathrm{d}y \ \mathrm{d}z \ . \tag{3.7}$$

For ergodic processes temporal and ensemble averaging can used interchangeably. There is evidence that turbulent flows in fact fulfill the ergodic hypothesis[115]. Hence, as the simulation in Section 4 assumes the underlying flow field to be ergodic, the ensemble average of isochromats within a volume of interest can be employed to derive the signal equations.

On the other hand, the spatial encoding process with finite resolution *cannot* be considered compliant to Equation (3.7), if motion within the sample is present. Instead of spatial averaging as in Equation (3.7), convolution with the point spread function (PSF), which itself varies depending on k-space trajectory[39,93,116] occurs.

For the fluctuating part $\vec{v}'(t) = \vec{v}(t) - \bar{\vec{v}}$, a timescale τ_c can be described[112,117] (defined in Equation (4.8)) based on the two-point velocity autocorrelation function $VACF_{m,n}(t, \tau) = \langle {v'}_m(t) \ {v'}_n(t+\tau) \rangle$ where $v'_{m,n}(t)$ denote the velocity fluctuations in the directions m, n[112] (see also Equation (4.39)). Given Equation (3.1), including the definition of the location correlation and the velocity autocorrelation, it is evident that as the timescale τ_c is on the order of the duration of motion encoding τ, motion encoding itself must be considered a continuous process. Subsequently, a spectral interpretation allows tailoring probing gradients for Lagrangian autocorrelation spectra.

4 Fundamentals of Turbulent Flow Spectrum Imaging

Hannes Dillinger[1], Charles McGrath[1], Christian Guenthner[1], Sebastian Kozerke[1]

[1] Institute for Biomedical Engineering, University and ETH Zurich, Zurich, Switzerland

Published as: Dillinger H, McGrath C, Guenthner C, Kozerke S. Fundamentals of turbulent flow spectrum imaging. *Magn Reson Med.* 2022;87(3):1231-1249. doi:10.1002/mrm.29001

4.1 Introduction

Time-resolved three-dimensional phase-contrast MRI (4D Flow MRI) has received significant attention in the field[27]. Applications of 4D Flow MRI include the assessment of valve diseases[118], aortic aneurysms / dissection[119,120], stenosis of pulmonary vessels[121] and many more. In aortic valve stenosis, quantification of blood flow jet velocities and maximum pressure gradients play a key role in clinical diagnosis[18]. Moreover, turbulent flow metrics including Turbulent Kinetic Energy (TKE) have been regarded of potential value. Binter et al.[12] have demonstrated that increased levels of TKE convey additional information relative to mean pressure gradients across stenoses and hence potential utility has been indicated for improved assessment of valve diseases.

Considerable research attention has been directed to mapping TKE using 4D Flow MRI[12,16,67]. Moreover, encoding of the full Reynolds stress tensor has been proposed to assess turbulent shear flow and to improve the estimation of net pressure losses[67,122].

The encoding theory of random motion in turbulent flow using MRI is covered in seminal studies by Kuethe et al.[123,124] and Gao et al.[125]. A theoretical framework has been formulated based on the assumption of an exponentially decaying correlation function, which was applied to map turbulent intensities in a stenosis phantom[126]. Based on this framework, Gatenby and Gore[127,128] differentiated between two regimes: $\tau_c \gg \tau$ and $\tau_c \ll \tau$, where the average correlation time τ_c for a fluid element to change direction is related to a velocity encoding gradient of duration 2τ.

The assumption $\tau_c \gg \tau$ constitutes the foundation of the work concerned with turbulence encoding[11,97]. However, to the best of our knowledge, this assumption has never been verified for phase-contrast MRI. While in vitro and in vivo measurements[129–131] in stenotic aortae with realistic flow conditions have predicted a correlation time τ_c in the millisecond range, it, at the same time, invalidates the assumption $\tau_c \gg \tau$ given practical bipolar gradient waveform lobe durations τ.

Of note, early work by Stepišnik[132,133] introduced a description of motion spectra in terms of the velocity auto-correlation function and its Fourier transform for diffusion MRI. The main conclusion derived by Stepišnik is that the attenuation of the magnitude signal solely depends on the area of the overlap of gradient and motion spectra. Callaghan and Stepišnik[134] successfully applied a method using different gradient spectra for predicting the frequency-varying diffusion coefficient in a moving fluid. In turbulent flow MRI, to the best of our knowledge, no such considerations have been made. Newling et al.[135] state that the correlation time must be imaged on a voxel basis to obtain precise estimates of

the diffusivity, however, while they refer to Gao and Gore's technique, they do not apply it.

The objectives of the current work are threefold: First, the spectral response of motion encoding gradient waveforms (incl. velocity encoding and velocity-compensated waveforms) is derived and evaluated with respect to their theoretical encoding power of characteristic turbulent flow spectra. It is shown that velocity encoding gradients of identical first gradient moments but different durations result in different degrees of underestimation of turbulence parameters. Second, a method for quantification of turbulent motion spectra using velocity-compensated gradients is presented and used to correct for systematic underestimation of turbulence parameters derived from velocity-encoded data. Third, a correction method for turbulence parameter estimation using velocity encoding gradients with different durations and without prior probing of the turbulent motion spectra is proposed.

4.2 Theory

Encoding of Incoherent Motion using Motion Encoding Gradients

The k-space signal equation yielding data $d(t)$

$$d(t) = \int_{\mathcal{V}} \rho_0 \left(\vec{r}\,'(t) \right) \mathrm{e}^{\mathrm{j}\varphi(t)} \, \mathrm{d}\vec{r}\,'(t) \,, \tag{4.1}$$

is based on the Fourier relation of the spatially dependent complex-valued transverse magnetization $\rho_0\big(\vec{r}\,'(t)\big)$ in the excited volume $\mathcal{V}$ given phase

$$\varphi(t) = \gamma \int_{t_0}^{t} \vec{G}\,(t') \cdot \vec{r}\,'(t') \, \mathrm{d}t' \tag{4.2}$$

and evaluated as the time integral of the gradient waveform $\vec{G}(t)$ and the time-dependent position vector of magnetization $\vec{r}\,'(t)$ starting at a reference point in time t_0 (assumed zero for the remainder of the manuscript). As the current manuscript focuses on motion-encoded phase, henceforth $\vec{G}(t)$ is termed motion encoding gradient (MEG). Depending on the order of moment compensation, a velocity-encoding gradient (VEG) with vanishing zeroth moment $\overrightarrow{M_0}(TE) = \int_0^{TE} \vec{G}\,(t) \, \mathrm{d}t \equiv 0$ or a velocity-compensated gradient (VCG) with vanishing zeroth and first moment $\overrightarrow{M_1}(TE) = \int_0^{TE} \vec{G}\,(t)(t - t_0) \, \mathrm{d}t \equiv 0$ with respect to echo time TE is obtained.

Temporal Interpretation

If incoherent motion is present in a voxel, the Fourier phase $\varphi(t)$ results from an ensemble of magnetization and the signal received can be written as the ensemble average[106]

$$E(t) = \overline{\mathrm{e}^{\mathrm{j}\varphi(t)}} = \exp\Big[\textstyle\sum_{n=1}^{\infty} \frac{(-1)^n}{n!} \int_0^t \int_0^t \dots \int_0^t \langle \, \mathrm{j}\varphi(t_1)\mathrm{j}\varphi(t_2) \dots \mathrm{j}\varphi(t_n) \rangle_c \, \mathrm{d}t_1 \, \mathrm{d}t_2 \dots \mathrm{d}t_n \Big], \tag{4.3}$$

where index c denotes the cumulant average[136], while the volume integral is omitted for brevity. If a Gaussian distribution is assumed (see Appendix), the resulting expression

for the signal of an ensemble of magnetization with Gaussian phase distribution is given as

$$E(t) = \exp\left[-\mathrm{j}\underbrace{\gamma \int_0^t \vec{G}(t') \cdot \overline{\vec{r}(t')}\ \mathrm{d}t'}_{\varphi_0(t)+\varphi_v(t)} - \underbrace{\tfrac{1}{2}\gamma^2 \int_0^t \int_0^t \vec{G}(t_1) \cdot \overline{\vec{r}(t_1)\ \vec{r}(t_2)}_{LC} \cdot \vec{G}(t_2)\ \mathrm{d}t_1 \mathrm{d}t_2}_{\alpha(t)} \right] . \quad (4.4)$$

As $\alpha(t)$ in Equation (4.4) is real-valued, it exhibits a damping of the magnitude, which is referred to as dephasing due to intravoxel standard deviation (IVSD[11]).

Performing a per-partes integration[137], Equation (4.4) results in

$$E(t) = \exp\left[-\mathrm{j}\underbrace{\gamma \int_0^t \vec{q}(t') \cdot \overline{\vec{v}(t')}\ \mathrm{d}t'}_{\varphi_v(t)} - \underbrace{\tfrac{1}{2}\gamma^2 \int_0^t \int_0^t \vec{q}(t_1) \cdot \overline{\vec{v}(t_1)\ \vec{v}(t_2)}_{LC} \cdot \vec{q}(t_2)\ \mathrm{d}t_1 \mathrm{d}t_2}_{\alpha(t)} \right] , \quad (4.5)$$

where $\vec{q}(t) = \int_0^t \vec{G}(t')\ \mathrm{d}t'$ denotes the time integral of the gradient waveform and $\vec{v}(t)$ denotes the instantaneous velocity. Of note, the amount of spin ensemble dephasing (i.e. the value of $\alpha(t)$), is solely dependent on the ratio of the correlation time scale τ_c (proportional to the term $\overline{\vec{v}(t_1)\ \vec{v}(t_2)}_{LC}$, further defined in Equation (*4.31*)) and the duration τ of the MEG given a fixed encoding strength.

The assumption $\tau_c \gg \tau$ implies that the spectral energy of the random process $\overline{\vec{v}(t_1)\ \vec{v}(t_2)}_{LC}$ is confined in a low frequency regime compared to the spectrum of the VEG. Therefore, the amount of dephasing given by $\alpha(t)$ in Equation (4.5) can be controlled by the MEG amplitude alone, independent of duration τ, as long as $\tau_c \gg \tau$ holds. However, satisfying $\tau_c \gg \tau$ for a given correlation time τ_c in the millisecond regime would result in infeasible MEG durations. It can therefore be necessary to operate in the regime $\tau_c \approx \tau$. As can be seen in Figure 4.1, τ_c may vary spatially and, for pulsatile flow, vary also temporally.

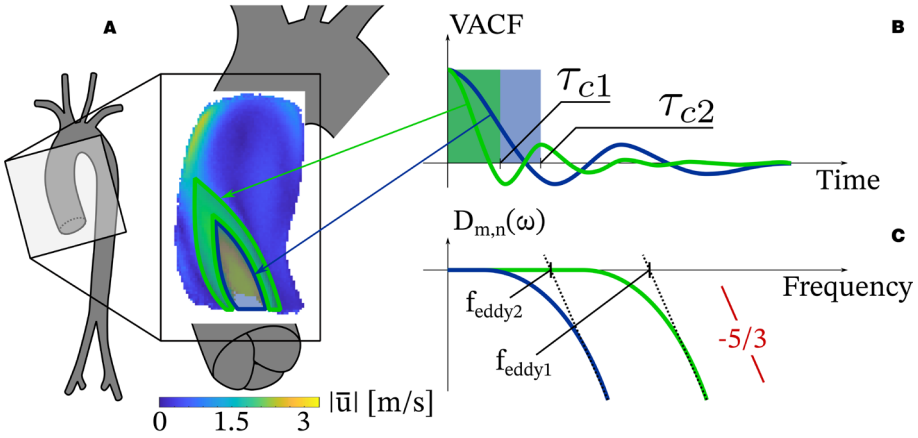

Figure 4.1: (A) Turbulence characteristics in a jet region vary spatially and temporally and can be described by random processes with different properties. Underlying mean velocity magnitude data[138] *$|\bar{u}|$ enables differentiation between jet core and boundary zone, for example, which are expected to show different turbulence characteristics (compare TKE plots in Binter et al.*[61]*). (B) Depending on the region, e.g. at the jet boundary, velocity autocorrelation functions exhibit a shorter correlation time τ_{c1} when compared to τ_{c2} in the jet core. (C) This results in different VACF spectra $D_{m,n}(\omega),\ m,n \in \{x,y,z\}$. The eddy frequency f_{eddy} is used to describe the spectral dynamics of the simplified random processes. $-5/3$ line depicts the begin of the inertial range of the two spectra, respectively.*

When neglecting all terms with orders higher than one in the expansion of the general distribution, Equation (4.4) results. The term $\varphi_v(t)$ is the phase component, which encodes bulk motion, while the second term $\alpha(t)$ encodes incoherent motion fluctuating around the mean. The tensor property of the product of the vectors $\vec{q}(\tau_1)$, $\vec{q}(\tau_2)$ and the matrix $\overline{\vec{v}(\tau_1)\ \vec{v}(\tau_2)}_{LC}$, in theory, enables probing of every element of the matrix by encoding a linear combination of the matrix elements. Since the correlation matrix $\overline{\vec{v}(\tau_1)\ \vec{v}(\tau_2)}_{LC}$ is necessarily symmetric, a dataset of six orthogonal measurements, i.e. a linear combination of the upper or lower triangle, provides all necessary information. ICOSA6[139], for example, is used to sample the surface of an icosahedron space which is spanned by the main gradient directions with the necessary six measurements. Recent implementations have employed a multi-v_{enc} approach[16] using a set of three different v_{enc}'s to account for the nonlinearity in the encoding of $\alpha(t)$ in $E(t)$.

Spectral Interpretation

The velocity autocorrelation function (VACF) of a random motion process is defined as

$$VACF(t,\tau) = \overline{\vec{v}(t)\ \vec{v}(t+\tau)} = \int_t^\infty \vec{v}(t') \cdot \vec{v}(t'+\tau)\ \mathrm{d}t' \ , \tag{4.6}$$

where $\vec{v}(t)$ is the instantaneous velocity. Given a stationary ergodic random process, temporal and spatial averaging can be exchanged yielding the same result and only the time interval τ, not the exact origin of time of the measurement, matters[106]. The VACF can therefore be written as

$$VACF(\tau) = \overline{\vec{v}(0)\ \vec{v}(\tau)}\ . \tag{4.7}$$

The correlation time τ_c defines a time scale for the "memory" of the random process[106,140] as

$$\tau_c = \frac{\int_0^\infty \overline{\vec{v}(0)\ \vec{v}(t')}\ \mathrm{d}t'}{\overline{\vec{v}(0)^2}}\ . \tag{4.8}$$

The spectrum of the VACF is given as the Fourier pair

$$D_{m,n}(\omega) = \tfrac{1}{2}\int_{-\infty}^{\infty} \overline{v_m(0)\ v_n(t')}\ \mathrm{e}^{\mathrm{j}\omega t'}\ \mathrm{d}t' = \int_0^\infty \overline{v_m(0)\ v_n(t')}\ \mathrm{e}^{\mathrm{j}\omega t'}\ \mathrm{d}t'\ , \tag{4.9}$$

where m,n denote different spatial directions $\{x,y,z\}$ and $D_{m,n}(\omega)$ is also known as the self-diffusion tensor[106]. In the right-most term, the even property of $VACF(\tau)$ is utilized. Equation (4.9) can be used to reveal the spectral relationship between the MEG and VACF spectrum, given as $S(\omega,t)$ and $D_{m,n}$, respectively, as

$$\alpha(t) = \tfrac{1}{2\pi}\gamma^2 \int_{-\infty}^{\infty} D_{m,n}(\omega)\ S(\omega,t)\,\mathrm{d}\omega\ . \tag{4.10}$$

Further details about the derivation can be found elsewhere[137].

The MEG spectrum is given as

$$S(\omega,t) = |\tilde{q}(\omega,t)|^2 \tag{4.11}$$

where $\tilde{q}(\omega,t) = \int_0^t q(t')\ \mathrm{e}^{\mathrm{j}\omega t'}\mathrm{d}t'$ and $q(t) = \int_0^t G(t')\ \mathrm{d}t'$, i.e. the Fourier transform of the time integral of gradient waveform samples (see Appendix or [41]).

From Equation (4.10) several conclusions can be drawn:

1. The signal attenuation caused by $\alpha(t)$ is determined by the area under the curve that is given by the product of the VACF spectrum $D_{m,n}(\omega)$ and the MEG i.e. the sensor spectrum $S(\omega,t)$.
2. If the MEG waveform would be an ideal bipolar Dirac function ($\vec{G}(0) = \vec{c}$, $\vec{G}(\tau) = -\vec{c}$, $\vec{G}(t) = \vec{0}\ \forall t \setminus \{0,\tau\}$, $\vec{c} \in \mathbb{R}^3$ i.e. a VEG waveform), the gradient spectrum $S(\omega,t) = \text{const}\ \ \forall\omega$ and hence permits probing the entire VACF spectrum. This can be interpreted as the short gradient pulse approximation[109] in analogy to literature on measuring the diffusion coefficient[110].
3. If the correlation time is significantly shorter than the time for motion encoding, $\tau_c \ll \tau$, Equation (4.10) can be approximated[133] as

$$\alpha(t) = \tfrac{1}{2\pi}\gamma^2 D_{m,n}(0) \int_{-\infty}^{\infty}\ S(\omega,t)\,\mathrm{d}\omega\ , \tag{4.12}$$

which results in the equation derived by Torrey[141], once the Parceval identity[41] is applied

$$\alpha(t) = \gamma^2 D_{m,n}(0) \int_0^t \underbrace{\left|\int_0^u \vec{G}(t')\ \vec{G}(t')\ \mathrm{d}t'\right|^2}_{q(u)}\ \mathrm{d}u \tag{4.13}$$

with $D_{m,n}(0)$ being the self-diffusion coefficient for the directional indices m,n, which is not dependent on ω since $D_{m,n}(\omega) \approx D_{m,n}(0)\ \forall\omega$ is assumed.

4. Turbulent kinetic energy (TKE) is given as $k = \int_0^\infty E_{m,m}(\omega)\,\mathrm{d}\omega$, where $E_{m,m}(\omega)$ denotes the energy spectrum[112], which can be interpreted as the VACF spectrum $D_{m,m}(\omega)$ (further details in the Appendix). Subsequently, only probing of the entire VACF spectrum in the limit of short gradient pulses results in quantitatively correct estimates of TKE.
5. Different frequency ranges of the VACF spectrum can be probed, if the gradient spectral response is tailored accordingly, potentially allowing reconstruction of the entire VACF spectrum from multiple measurements.

Relation to Turbulence Theory

Reynolds decomposition of turbulent velocity fields results in separate mean and fluctuating velocity field components[112]. The fluctuating component can be described by a random process[117] with correlation time τ_c. If $\vec{v}(t)$ is assumed to be the velocity of a fluid particle in the flow field, it is found, by inserting VEG waveforms into Equation (4.5), that $\alpha(t)$ encodes the VACF[142].

The Reynolds Stress Tensor (RST) is defined by the covariance of velocity components,

$$RST = \begin{bmatrix} \sigma_{xx}^2 & \sigma_{xy}^2 & \sigma_{xz}^2 \\ \sigma_{yx}^2 & \sigma_{yy}^2 & \sigma_{yz}^2 \\ \sigma_{zx}^2 & \sigma_{zy}^2 & \sigma_{zz}^2 \end{bmatrix} \quad , \tag{4.14}$$

where $\sigma_{mn}^2 = \langle u_m u_n \rangle,\ m,n \in \{x,y,z\}$[35]. The definition of the covariance of the velocity

$$\langle u_m u_n \rangle = \overline{u_m u_n} - \overline{u_m}\ \overline{u_n} \quad , \tag{4.15}$$

directly connects the RST to the location correlation (denoted in Equation (4.4) and defined in the Appendix) when using VEGs.

4.3 Spectra of Velocity Encoding (VEG) and Velocity Compensated Gradients (VCG)

The gradient spectra $S(\omega,t)$ for VEGs with identical first gradient moment $M_1 = \pi/(\gamma v_{enc})$ for $v_{enc} = 450\mathrm{cm/s}$ (used in recent works[9]) but different frequencies are shown in Figure 4.2A. The VEG waveforms respect the gradient limit specifications given in the Methods section.

The gradient spectrum of a VEG with duration 2τ and $f_{VEG} = 1/(2\tau)$ is characterized by a *sinc* function with the first zero-crossing at $f_0 = 2f_{VEG}/N$ (Figure 4.2B), where N is the number of repetitions. In general, the zero-frequency lobe is always dominant.

In Figure 4.2C, VCG gradient waveforms for a different number of repetitions but constant frequency f_{VCG} are shown. Their amplitude is scaled according to their maximum first moment over time. The VCG spectra $S(\omega,t)$ (Figure 4.2D) exhibit a lobe at the gradient frequency, however, they do not show a zero-frequency lobe. Their spectra are well suited for point-wise probing the VACF spectrum due to their narrow frequency band in the gradient spectrum.

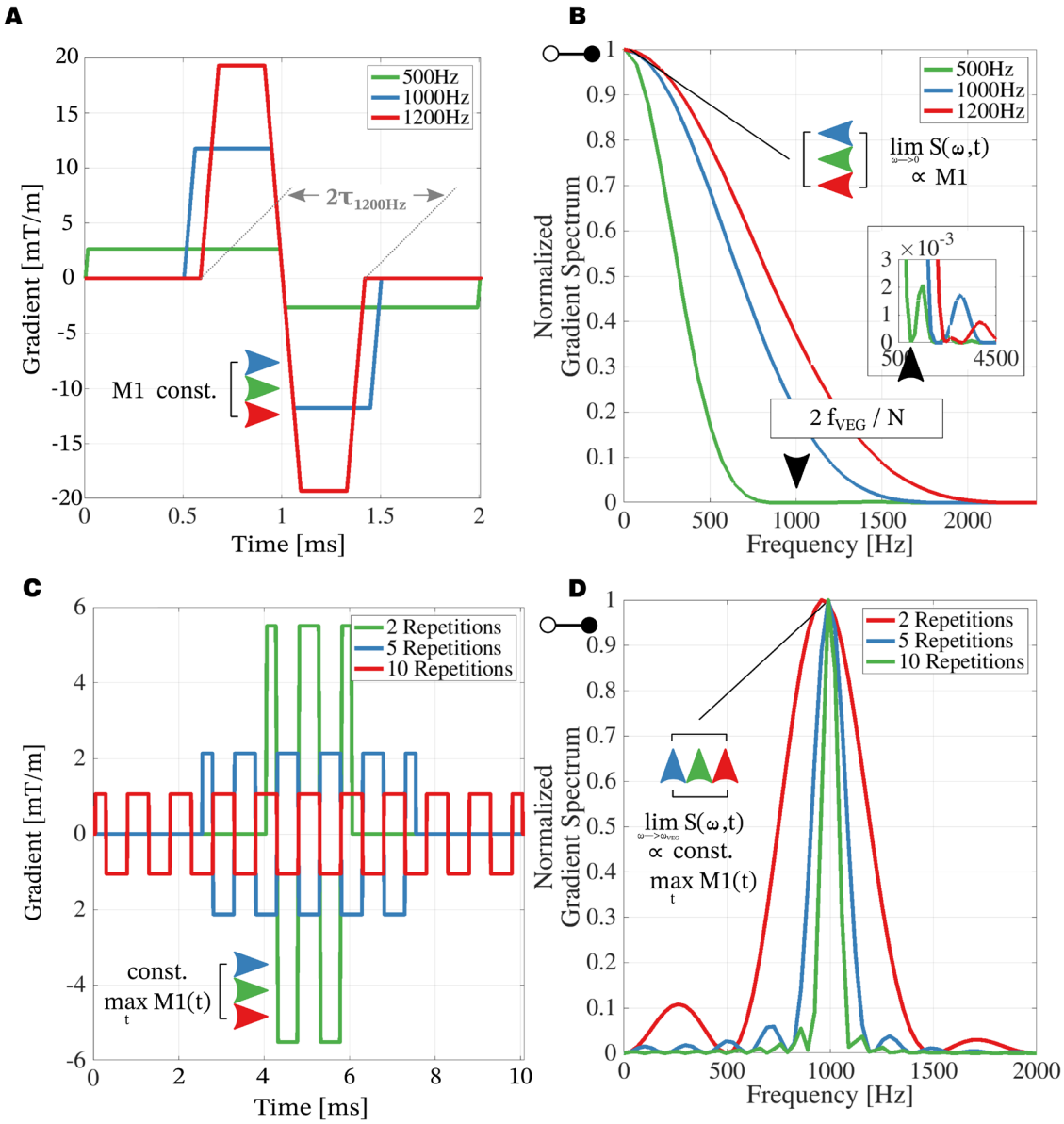

Figure 4.2: Gradient waveforms and spectra for (A, B) velocity encoding gradients VEG ($v_{enc} = 450cm/s$, $f_{VEG} = \{500,1000,1200\}Hz$) and (C, D) velocity-compensated gradients VCG ($f_{VCG} = 1000Hz$, $N_{f_{VCG}} = \{2,5,10\}$). The spectra plots are calculated according to Equation (11) and are normalized by their value at $f = 0$ and $f = f_{VCG}$ for VEGs and VCGs, respectively. (A) The gradients have same first moment M_1 (i.e. same v_{enc}) but different durations, which (B) determine the spectral coverage. Inset: Secondary peaks in the spectrum with amplitude reduced by a factor of approx. 500 compared to zero frequency amplitude can be neglected. (C) VCG amplitudes are defined by their maximum first moment during encoding time $\max_t M_1(t)$, $t = [0, t_{dur}]$ (see Supplementary Information Figure S4 online). VCGs exhibit a (D) narrow peak in the spectrum which renders them suitable for point-wise probing.

4.4 Encoding Power of Gradients

Given Equation (4.10), knowledge about both the VACF spectrum $D_{m,n}(\omega)$ and MEG spectrum $S(\omega, t)$ is necessary to estimate the encoding strength $\alpha(t)$. VACF spectra of stenotic flows have been investigated in numerous works[114,129,131,143–150]. Assuming a simplified one-dimensional model VACF spectrum $E(\kappa, l, c_l)$[112] given by

$$f_l(\kappa, l, c_l) = \left(\frac{\kappa l}{\kappa l + c_l}\right)^{\frac{5}{3}} \quad , \tag{4.16}$$

$$E(\kappa, l, c_l) = \kappa^{-5/3} f_l(\kappa, l, c_l) \quad ,$$

where κ is the wave number, l a reference length and $f_l(\kappa, c_l)$ is a non-dimensional function which defines the shape of the inertial range and tends to unity for small κl, a VACF spectrum based on $c_l = f_{eddy}^2 l$ can be defined. The cutoff-frequency f_{eddy} defines the onset of the $-5/3$ inertial range[35] and ranges from several 10 Hz[148] up to 1000Hz[151], depending on the Reynolds number Re and viscosity ν. For example, increasing the viscosity from $\nu_{water} = 0.71\text{mm}^2/\text{s}$ to $\nu_{blood} = 2.6\text{mm}^2/\text{s}$ at 36°C[152], and keeping other parameters constant, increases the eddy frequency almost 4-fold. Exemplary plots of VACF and VEG spectra are depicted in Figure 4.3A.

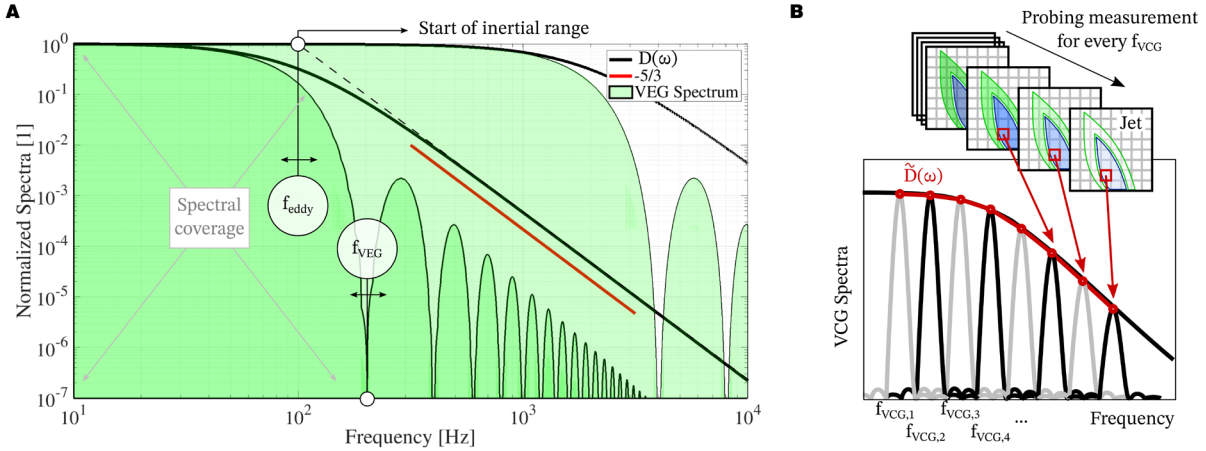

Figure 4.3: (A) Comparison of normalized VACF spectra $D(\omega)$ for $f_{eddy} \in \{100, 2000\}Hz$ and VEG spectra for gradient frequencies $f_{VEG} \in \{100, 2000\}Hz$ using logarithmic scaling. For low frequency VACF spectra, the high frequency VEG provide sufficient spectral coverage whereas the low frequency VEG coverage may be insufficient. $-5/3$ lines depict the slope of the VACF spectra in the inertial range. (B) Using velocity-compensated gradients (VCG) of frequency $f_{VCG,n}$, $n \in \mathbb{N}$, it is possible to reconstruct an estimate $\widetilde{D}(\omega)$ of the true VACF spectrum $D(\omega)$ per voxel. This information can be used for correction of limited spectral coverage of VEG.

Depending on the specific shape of the VACF spectrum, the coverage of the VEG spectrum might be insufficient. Using a normalized form of Equation (4.10) and $D(\omega) = E(\kappa, l, c_l)$, yields the relative encoding power $\tilde{\alpha}(t)$ of a VEG spectrum $S(\omega, t)$,

$$\tilde{\alpha}(t) = \frac{\int_{-\infty}^{\infty} D(\omega)\ S(\omega, t)\, \mathrm{d}\omega}{\int_{-\infty}^{\infty} D(\omega)\, \mathrm{d}\omega} \tag{4.17}$$

depending on the eddy frequency, which is shown in Figure 4.4A, where integration was performed in the frequency range as given in Figure 4.3A. The relative encoding power for a fixed VEG frequency of $f_{VEG} = 900\text{Hz}$ but varying f_{eddy} regimes is depicted in Figure 4.4B.

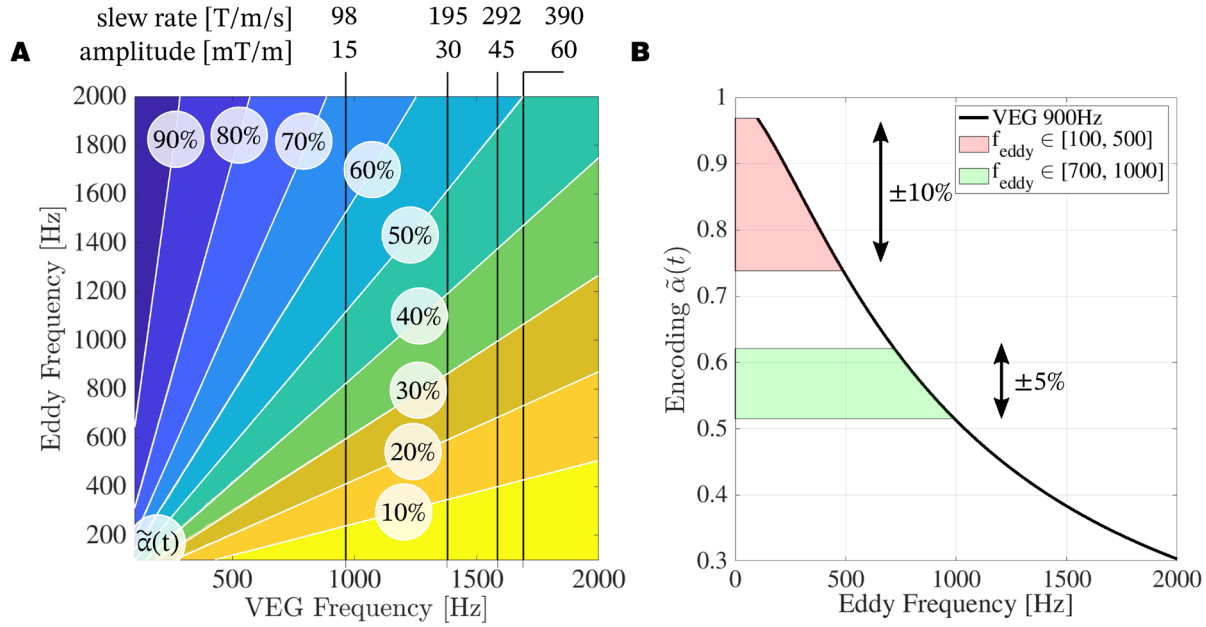

Figure 4.4: (A) Relative encoding power $\tilde{\alpha}(t)$ given by Equation (4.17) (color and isolines) depending on the VEG frequency f_{VEG} (abscissa) and the eddy frequency f_{eddy} (ordinate) for $v_{enc} = 450cm/s$ for given maximum slew rate and gradient amplitude (respective values stated above the plot). (B) Assuming gradient limits of slew rate 195T/m/s and maximum gradient amplitude 0.03T/m (currently available on clinical MRI systems) and VACF spectra comprising $f_{eddy} \in [100, 500]$, for example, the magnitude damping $exp(\tilde{\alpha}(t))$ of the VEG at maximum frequency 900Hz varies within up to ±10% depending on f_{eddy} (plot is normalized by value $\tilde{\alpha}(t)$ at first frequency). This results in spatially varying damping and is dependent on the voxel position for inhomogeneous turbulent flows. It cannot be corrected for (all gradients already have same v_{enc}). The uncertainty due to a range of f_{eddy} in a noise-less signal is shown by red/green areas and indicated by percentage values.

4.5 Current Approach of Intravoxel Standard Deviation Estimation

The intravoxel standard deviation σ (IVSD) is encoded based on the signal model presented by Dyverfeldt et al.[97], which relates the magnitude signal of two differently encoded segments $|S(k_{v1})|$ and $|S(k_{v2})|$, using the encoding velocity moments k_{v1} and k_{v2} according to

$$\sigma = \sqrt{\frac{2\ln\left(\frac{|S(k_{v2})|}{|S(k_{v1})|}\right)}{k_{v1}^2 - k_{v2}^2}}\,. \tag{4.18}$$

The model relies on the assumption $\tau_c \gg \tau$, which was estimated around $\tau_c \geq 10\text{ms}$[11] based on MRI data[153]. In vitro measurement using Laser Doppler Anemometry (LDA) of realistic flow conditions and viscosity, predict, however, $\tau_c \approx 1\text{ms}$[131]. This may invalidate the assumption $\tau_c \gg \tau$ as the spectral coverage of the gradients is not taken into account.

4.6 Methods

Large Eddy Simulation

Computational fluid dynamics (CFD) simulations using a Large Eddy Simulation approach (LES) in OpenFOAM v1912 were performed on a "stenotic" tube (75% area reduction, cosine shape[154]). A parabolic inlet profile resulting in

$$\mathrm{Re} = \frac{uD}{\nu} = 4000 \ , \tag{4.19}$$

based on the free flow diameter D, the mean flow velocity u at the inlet and the dynamic viscosity of whole blood at 36°C ($\nu = 2.6$ mm^2/s) was used. Details about the mesh and validation of the CFD solver can be found in Supplementary Information Figure S1 and S2 online, respectively.

For non-stationary input data, as Petersson et al. noted[155], agreement between LES and simulated MRI data is poor, if the time-averaged flow quantities are used. Instead of randomly choosing timeframes from the instantaneous solution[51], the CFD data was extracted continuously in time, beginning at an arbitrary reference time point, and then fed into the MRI simulation. This process emulates the start of an MRI acquisition at some point in time and running the MRI simulation for the duration of the MEG. Therefore, time resolved CFD data were exported for slices in the x,z-plane with Δt = 100 µs and linearly interpolated onto the MRI simulation time grid. Online supporting Information Video S1 shows the CFD slices over time.

MRI Simulation VEG

Our recently presented MRI simulation particle tracing approach[39] was extended to include random motion based on a discrete random walk model (DRW)[156]. The fluctuating velocities $v'_x,\ v'_z$ were kept constant for a spatially varying time constant defined by the Lagrangian integral time

$$T_L \approx 0.30\ \frac{k}{\varepsilon} = 0.30 \frac{1}{\omega} \ , \tag{4.20}$$

where k, ε and ω denote the turbulent kinetic energy (TKE), the standard dissipation rate and the specific dissipation rate of TKE of the LES turbulence model, respectively. The eddy lifetime $\tau_{eddy} = 2T_L$ relates to the eddy frequency as $f_{eddy} = 1/\tau_{eddy}$. As shown in Figure 4.5, the eddy frequency of the dataset used as input data was in the range $f_{eddy} = [1000, 5000]$Hz. A similar approach has also been used in other works concerned with turbulent MRI simulations[36]. The current simulation does not assume isotropy and employs Cholesky decomposition to draw samples from correlated distributions given by the covariance matrix Σ according to

$$\begin{aligned} &\zeta_{x,z} \sim \mathcal{N}(0,1) \ , \\ LL^{\mathrm{T}} = \Sigma, \quad &\Sigma = \begin{bmatrix} \sigma_{xx}^2 & \sigma_{xz}^2 \\ \sigma_{zx}^2 & \sigma_{zz}^2 \end{bmatrix}, \quad \Sigma \text{ is spd}, \\ &\begin{bmatrix} v'_x \\ v'_z \end{bmatrix} = L \begin{bmatrix} \zeta_x \\ \zeta_z \end{bmatrix} \ , \end{aligned} \tag{4.21}$$

where Σ is derived from RST values $\sigma_{mn}^2,\ m, n \in \{x, z\}$ taken from CFD data.

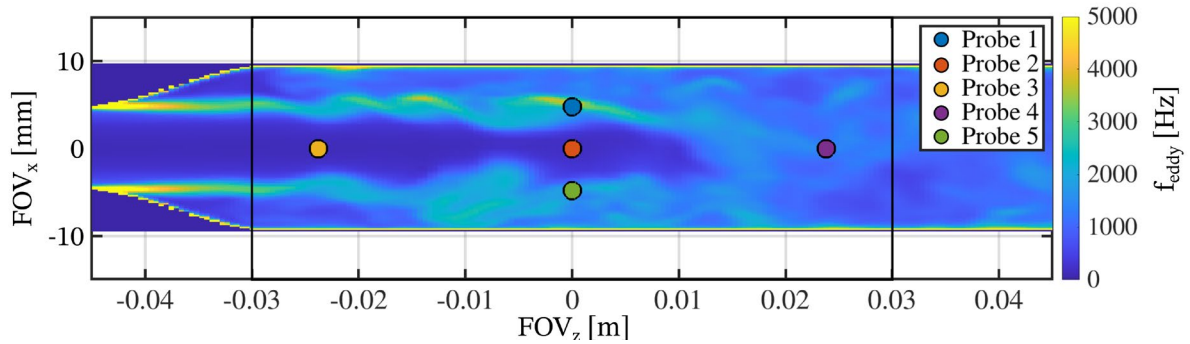

Figure 4.5: Probe positions P1 to P5 used for the Lagrangian VACF and VACF spectrum calculation. Underlay image encodes the eddy frequency f_{eddy} (colorbar) of the first CFD input data frame. Probe 1 and 5 are in high eddy frequency regions (jet border), while Probe 2 and 3 are in low eddy frequency regions (jet core). Probe 4 is set in an intermediate eddy frequency region (transitional region where the jet breaks down). Markers not to scale with the probe radius r.

The computational framework[39], written in MATLAB R2017b (The MathWorks, Natick, Massachusetts), was modified to utilize GPU functions and the forward Euler method (fixed step length of $\Delta t = 1\mu s$) was used to increase speed and extensibility. A total of $n_{tot} = 10^6$ tracer particles were seeded in the simulated field-of-view (FOV). The particles' position increment per time step is given by $\Delta i(t + \Delta t) = \left(\bar{v}_i(t) + v'_i(t)\right) \Delta t,\ i \in \{x, z\}$. The CFD input time frames were linearly interpolated in time between simulation time steps t and $t + \Delta t$. Online supporting Information Video S2 exemplary shows the particle motion over simulation time.

Simulation runs with different gradient frequencies f_{VEG} (i.e. several $S(k_{v2})$, same v_{enc}) were compared to a non-encoded reference data ($S(k_{v1})$ i.e. without applying a VEG and hence $v_{enc} = \infty$). The segments $v_{enc} \neq 0$ and $v_{enc} = \infty$ (reference) were not assumed to be separated in time, i.e. using the same CFD input data time frames. This mimics a beat-interleaving strategy of motion encoding segments as in cardiac-gated scans. The encoding was simulated only in z-direction as the extension to other directions is readily made and provides no new insights. Equation (4.18) was used for calculation of σ_{zz}. Ground truth was assumed to be the first CFD input data time frame at $t = 0$ down-sampled to the MRI image size.

To keep the simulation tractable on a normal workstation, the simulation time was limited to the velocity encoding phase t_{dur}, where $t_{dur} = 1/\min(f_{VEG}) = 2\text{ms}$ since $f_{VEG} = \{500, 1000, 1200\}\text{Hz}$. Of note, this mimics instantaneous readout at time t_{dur}, which enables the current work to focus on the effects of motion encoding rather than readout artefacts due to motion[39]. No noise or coil sensitivities were simulated. In addition, particles were seeded on a 2D plane and through-plane velocities were neglected to reduce computational load. The simulation was repeated 10 times and resulting images were averaged.

Gradient Waveform Spectra

The VEG spectrum $S(\omega, t)$ (Equation (4.11)) was evaluated after the gradient was played out, i.e. at $t = t_{dur}$. The VEG waveforms used in the simulation are depicted in Figure 4.2A. The gradient waveforms were centered around $t_{dur}/2$. The VEG spectra depicted

in Figure 4.2B were normalized to their maximum value, which is proportional to their first gradient moment[106].

Intravoxel Mean Velocity Variations (MVV)

The estimation of Intravoxel Mean Velocity Variations (MVV) as given by Dyverfeldt[11] reads

$$\sigma_{turb} = \sqrt{\sigma_{IVSD}^2 - \frac{2}{k_v^2}\ln\left(\frac{S_{MVV}(0)}{S_{MVV}(k_v)}\right)}\ , \tag{4.22}$$

where σ_{turb} and σ_{IVSD} denote the IVSD due to turbulence and the measured IVSD, respectively. Estimation of the term inside the brackets is based on a linear velocity gradient across a voxel[11]. This estimation is valid as long as magnetization does not move across several voxels during motion encoding. As the current manuscript is concerned with high-flow regimes, it is estimated that, for severe stenosis ($v_{max} \geq 4$m/s [18]) and typical motion encoding durations (0.5 – 1ms), magnetization moves by more than one voxel (typ. resolution 2.5mm) in the jet region.

The IVSD due to mean velocity only is given as

$$\sigma_{MVV}^2 = \frac{2}{k_v^2}\ln\left(\frac{S_{MVV}(0)}{S_{MVV}(k_v)}\right)\ , \tag{4.23}$$

and can be assessed by performing the simulation without fluctuating velocities. As massless tracer particles are used, any spatial gradient in the mean velocity field will contribute to σ_{MVV}^2 (see Appendix; Particle Motion Equation). For correction, σ_{MVV}^2 is subtracted from σ_{IVSD}^2 to obtain results devoid of IVSD due to mean velocity. Resulting IVSD from mean velocity σ_{MVV} is presented in Supplementary Information Figure S3 online.

VACF and VACF spectrum $D(\omega)$

The Lagrangian velocity autocorrelation function VACF is given by calculating the autocorrelation of velocity samples of probe velocities. The particles were selected at $t = 0$ at given locations shown in Figure 5 within a radius of $r = 1$mm,

$$VACF_{m,m,p}(t_s) = \langle u_{m,p}(r_s, t_s)\ u_{m,p}(r_s, t_s)\rangle\ , \quad m \in \{x, z\} \tag{4.24}$$

where r_s, t_s denote the probe position and probed time, respectively, and $p \in \{\textit{particle indices within } r\}$. Taking the mean $VACF_{m,m}(t_s) = \frac{1}{|p|}\sum_{p'=1}^{|p|} VACF_{m,m,p'}(t_s)$, multiplying it with a Tuckey window of the same length and applying the Discrete Fourier Transform (DFT) results in the velocity autocorrelation spectrum (VACF spectrum) $D_{m,m}(\omega)$.

MRI Simulation VCG

For probing the VACF spectrum, the MRI simulation was conducted assuming a high-performance gradient system (max. gradient amplitude 80mT/m, max. slew rate 210T/m/s), gradient frequencies were set to $f_{VCG} = [100{,}200, \ldots, 5000]$Hz resulting in 50 probing frequencies and waveforms were repeated for

$$N_{f_{VCG}} = 2\left\lfloor \frac{f_{VCG}}{\max(f_{VCG})} \right\rfloor \tag{4.25}$$

to achieve approximately the same spectral bandwidth. Given a fixed-time encoding window $t_{dur} = \min(N_{f_{VCG}}) / \min(f_{VCG}) = 20\text{ms}$ and $N_{f_{VCG}}$ repetitions for VCG of frequency f_{VCG}, the spectral width of the response lobe becomes independent of f_{VCG}, allowing the entire spectrum to be probed by changing the gradient frequency. VCG waveforms were calculated such that their maximum first moment $M_{1,max} = \max_{t}(M_1(t)) = \int_{t_0}^{t_0+t} G(t)(t-t_0)\,\mathrm{d}t$ corresponded to $v_{enc} = \pi/(\gamma M_{1,max}) = 450\text{cm/s}$ (see Supplementary Information Figure S4 online), where again $t_0 = 0$ was assumed.

Resulting gradient spectra and waveforms are depicted in Figure 4.9C and Figure 4.9D, respectively. Due to integer rounding in Equation (4.25), the relationship between first moment and peak values in the spectra holds only approximatively. The resulting images were calculated according to Equation (4.18) where σ_{zz} denotes the encoding of the intravoxel standard deviation along the direction z.

For probing the VACF spectrum, mean velocities were set to zero to avoid changes in turbulence parameters due to mean particle motion and to enable comparison to ground truth (GT). As particles are expected to stay within a region with spatially homogeneous parameters, Lagrangian (moving particles) and Eulerian (voxel) spectra yield the same result. To ensure spatial and temporal homogeneity, $f_{eddy} = 1\text{kHz}$ and $\sigma_{zz} = 0.3\text{m/s}$ were fixed for all CFD input data time frames for all voxels.

Spectral Correction Method

By employing knowledge about the spectrum $D(\omega)$ and the gradient spectrum $S(\omega, t)$, the limited spectral encoding ability of the VEG gradients was corrected on a voxel basis. For given flow this results in a quantitative correct estimate of standard deviations σ_{mn}, $m, n \in \{x, y, z\}$.

The per-voxel estimate of VACF spectra $\widetilde{D}(\omega)$ was calculated from simulations with VCGs by linearly interpolating between probed frequencies (Figure 4.3B). The relative encoding power $\tilde{\alpha}(t)$ per voxel was given by the full version of Equation (4.17) and used for correction by employing

$$\sigma_{corrected} = \sigma_{f_{VEG}} \,/\, \tilde{\alpha}_{f_{VEG}} \quad , \tag{4.26}$$

given an uncorrected measurement of $\sigma_{f_{VEG}}$ resulting in the corrected estimate $\sigma_{corrected}$ of IVSD for a given VEG frequency f_{VEG} using Equation (4.18).

Without additional VCG measurements, the VEG spectrum $S(\omega, t)$ could be estimated from gradient waveforms exclusively. Assuming $D(\omega) \approx \text{const.}\ \forall\,\omega$, Equation (4.18) resulted in an estimate for the encoding power for a given VEG

$$\tilde{\alpha}_{f_{VEG}}(t) = \int_{-\infty}^{\infty} S(\omega, t)\,\mathrm{d}\omega \tag{4.27}$$

which was used to correct for experiments employing VEGs. Phase-contrast sequences with high and low v_{enc} values to account for nonlinearities in Equation (4.18) may result in different VEG frequencies and, if uncorrected for, inconsistencies in σ_{mn} estimation across v_{enc} values[157]. The spectra $S(\omega, t)$ of VEGs $f_{VEG} = \{500, 1000, 1200\}\text{Hz}$ were

calculated according to Equation (4.11) and the encoding power across v_{enc} values was normalized using

$$\tilde{\alpha}'_{f_{VEG}} = \frac{\tilde{\alpha}_{f_{VEG}}}{\tilde{\alpha}_{\max(f_{VEG})}} \,. \tag{4.28}$$

4.7 Results

VACF Spectrum

The VACFs in x and z direction and their spectra at different probe positions are depicted in Figure 4.5. Depending on the specific probe position r_s as a function of time and corresponding $f_{eddy}(r_s, t)$, the VACF spectrum follows the shape of exemplary model spectra defined in Equation (4.16) with the roll-off frequency related to the eddy frequency. The spectrum is inherently multiplied by a *sinc* function due to the discrete random walk model used; the local minima are given by the update rate f_{eddy} the magnetization experiences during simulation time. Due to the high flow velocity in z direction (Figure 4.6C and Figure 4.6D), it can be seen that probe 1 has a low correlation during $t = [0, 0.1]$ms, as the probed particles start in a high f_{eddy} region and are transported to a lower f_{eddy} region. This results in reduced correlation due to spatial inhomogeneity of velocity and turbulence parameters and, subsequently, a higher frequency coverage in the spectrum.

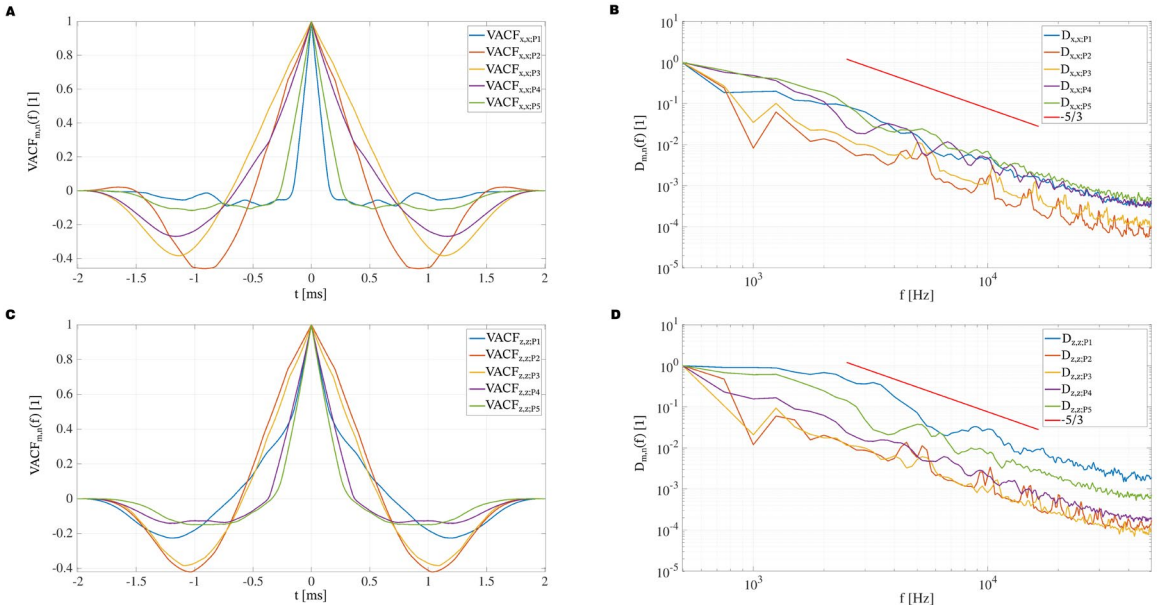

Figure 4.6: Lagrangian velocity autocorrelation functions (VACF) in (A) x direction (index xx) and (B) z direction (index zz) for different probe positions P1 to P5. (B), (D): VACF spectra in x and z direction. Different probe positions relate to regions of different eddy frequencies and therefore different autocorrelation functions and spectra. Particles in regions of high f_{eddy} show fast decaying VACFs (e.g. Probe 1, 2). Transport to a different region due to mean flow results in a kink in the VACF (e.g. VACF in z direction Probe 1). Highest frequency of start of the inertial range in (D) (stream-wise) is found at 2kHz for Probe 1.

Mean Velocity and Turbulence Parameter Estimation

In the plots shown in Figure 4.7, results of estimated mean velocities are similar for different VEG frequencies. Spatial misregistration due to finite VEG duration is found when compared to ground truth. The spatial misregistration corresponds to the distance $\Delta z = V_z \tau$ a particle would move during time $t_{dur}/2$, as VEGs are centered at $t_{dur}/2$. The misregistration is given by $\Delta z = 2\text{mm}$ in a region where the mean velocity is approximately 2 m/s and $t_{dur} = 2\text{ms}$. For the IVSD results depicted in Figure 4.8, σ_{zz} is seen to be reduced by 50% when compared to ground truth when using a VEG of 500Hz. On the other hand, increasing the VEG frequency decreases the difference between σ_{zz} and ground truth. Using histogram analysis in Figure 4.8B, a difference of mean value of 29% between 500Hz and 1200Hz gradient is found, while mean velocity distributions show no difference. Of note, the model by Dyverfeldt[11] would predict the same values of σ_{zz} for all tested VEG frequencies because of the same v_{enc} used.

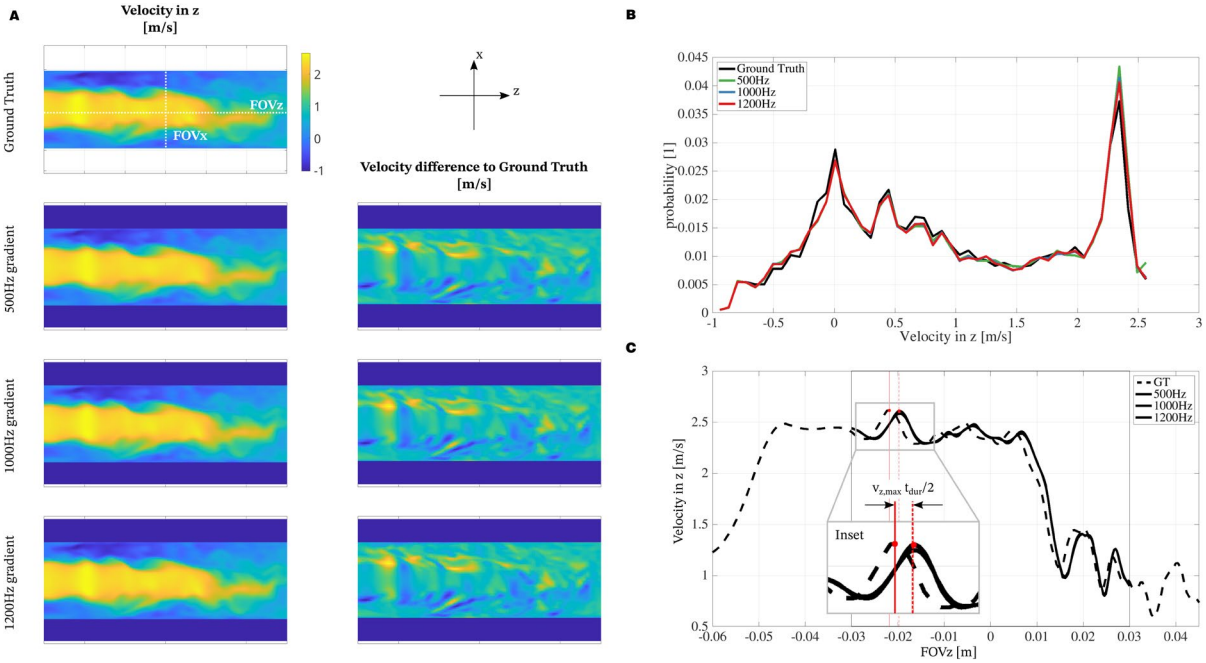

Figure 4.7: (A) Comparison of velocity simulation output for $f_{VEG} = \{500, 1000, 1200\}$ Hz to ground truth yields that the mean velocity is found to be imaged correctly and results in comparable images for different f_{VEG}. (B) The mean velocity distribution does not depend on f_{VEG}. (C) The mean velocity profile shows only spatial misregistration artefacts compared to ground truth, which relates to $v_{z,max}\ t_{dur}/2$ as instantaneous imaging is assumed at the end of the VEG (Inset).

Mean Flow Influence on Turbulence Estimation

Conducting the simulation without random motion components $\begin{bmatrix} x' \\ z' \end{bmatrix}$ in Equation (4.21) results in an estimate of σ_{zz} due to mean velocity only. Resulting σ_{zz} plots and their respective histograms can be found in Supplementary Information Figure S3 online. Given mass-less tracer particles were assumed, the imaged σ_{zz} due to mean velocity only corresponds to the mean velocity gradient in VEG direction and is not dependent on the VEG frequency. Tracer particle dynamics are further discussed in the Appendix.

Corrected Turbulence Estimation

In Figure 4.9A, good agreement is found between normalized VACF spectra given by Lagrangian probes and the VACF spectrum estimated from VCG probing measurements, therefore confirming the feasibility of probing the VACF spectra. Using the correction method employing knowledge about both the VEG spectra and the probed VACF spectra using VCG measurements, Figure 4.9B shows that the estimation error reduces from -49% to -10% for $f_{VEG} = 500$Hz and from -21% to -5% for $f_{VEG} = 1200$Hz. Figure 4.9C and Figure 4.9D show spectra and waveforms of VCGs with varying frequencies used in the probing measurement. Due to their narrow bandwidth of approx. 100Hz, point-wise probing of the VACF spectrum is possible.

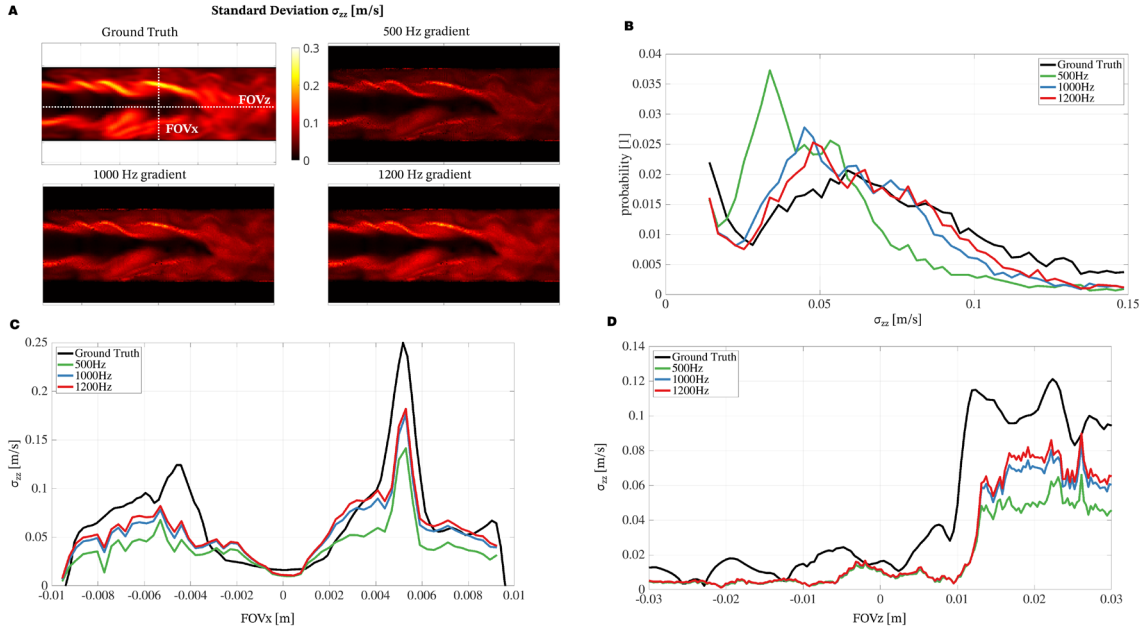

Figure 4.8: Comparison of standard deviation σ_{zz} for $f_{VEG} = \{500, 1000, 1200\}$ Hz in z direction with ground truth (GT) shows that σ_{zz} is systematically underestimated and its estimated values differ for different f_{VEG}. (A) Increasing f_{VEG} results in an improved estimation of σ_{zz} compared to ground truth. (B) The σ_{zz} distribution is shifted towards lower values as f_{VEG} decreases. This results in increased underestimation of standard deviation values for decreased f_{VEG}. σ_{zz} profiles are depicted along FOV_x (C) and FOV_z (D). Level of underestimation compared to GT is increased in regions of high eddy frequency (compare Figure 4.5). Due to mean velocities, misregistration artefacts are found in (D) (compare also Figure 4.7).

In Figure 4.10A, estimates of IVSD are presented which have been corrected without additional probing but by employing Equation (4.28). The IVSD estimates are coherent across different values of v_{enc} but underestimate ground truth. This is confirmed in the

histogram analysis in Figure 4.10B and profiles in Figure 4.10C and Figure 4.10D.

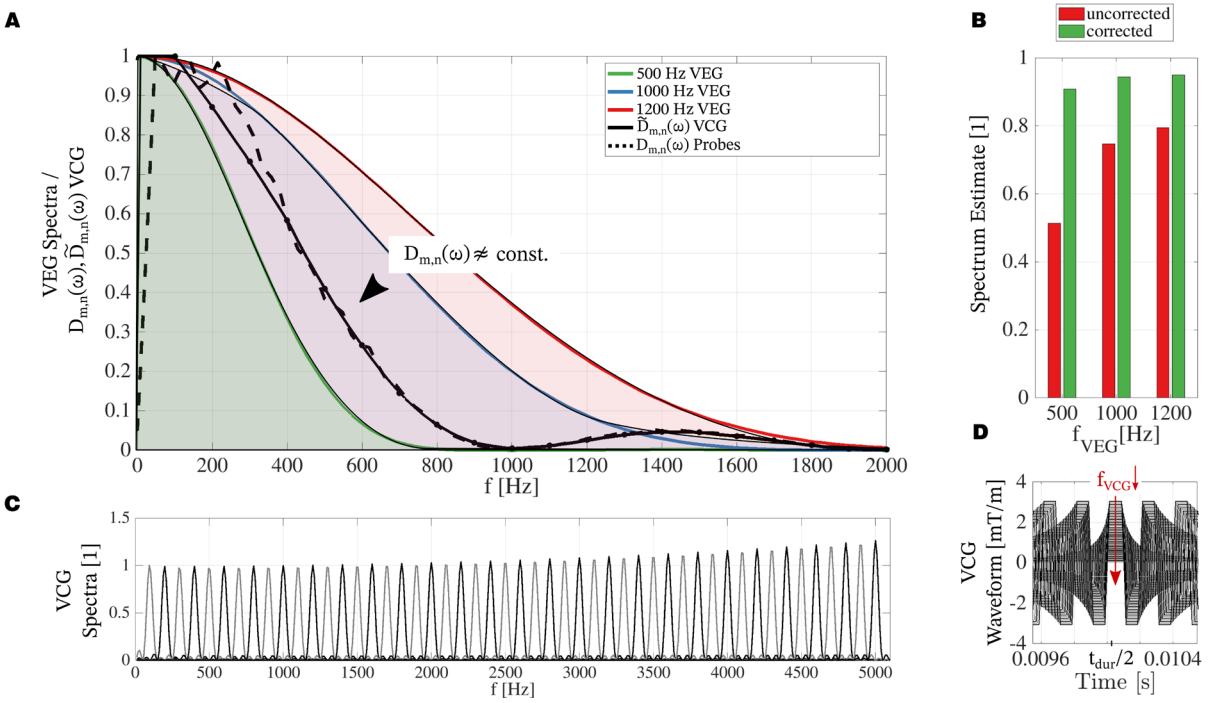

Figure 4.9: (A) Estimated VACF spectrum $\widetilde{D}_{m,n}(\omega)$ (black continuous line) compared to VACF spectra $D_{m,n}(\omega)$ (black dotted line) using spatially invariant input data and zero mean velocity to enable direct comparison. Each point of the continuous curve relates to a simulation run with the respective VCG. Good agreement between the Lagrangian VACF spectrum and the estimated spectrum is found. (B) Applying the correction method employing both $\widetilde{D}_{m,n}(\omega)$ (estimated from VCG measurements) and $S(\omega)$ (calculated from VEG parameters), the underestimation is reduced from 49% to 10% for 500Hz VEG. (C) Normalized spectra of VCGs used for probing the VACF spectrum. Due to integer rounding in Equation (4.25), different numbers of repetitions may result in differences in spectral bandwidth. Spectra are normalized in the plot by the initial probing gradient where, due to slew rate limitations, maximum spectra values increase for higher frequencies. (D) VCG waveforms used for probing. The plot depicts details of the full waveforms for $t = [0, t_{dur}]$.

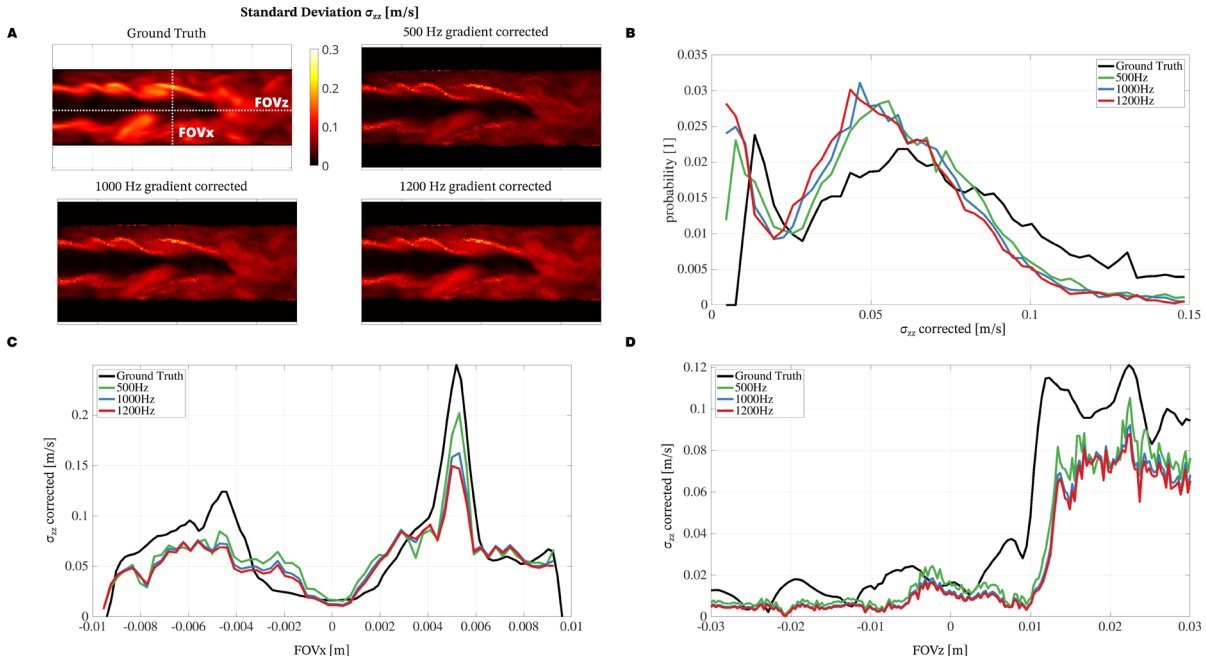

Figure 4.10: (A) Estimated standard deviation σ_{zz} for VEG frequencies $f_{VEG} = \{500, 1000, 1200\} Hz$ with applied VEG spectrum correction according to Equation (4.28) without prior probing of the VACF spectrum by VCG measurements. (B) The σ_{zz} distribution is consistent within different f_{VEG}. Compared to ground truth, the distribution is underestimated as $max(f_{VEG}) < \infty$. σ_{zz} profiles along FOV_x (C) and FOV_z (D) show coherent estimates of the standard deviation across different f_{VEG} after applying the correction method.

4.8 Discussion

Based on the framework presented, velocity encoding gradients (VEG) and their spectral response in relation to probing turbulent flow have been investigated.

Assuming velocity autocorrelation function spectra of turbulent flow[112], and VEG gradients with a v_{enc} of 450cm/s and 1ms duration, current models for turbulence quantification[11] are shown to systematically underestimate turbulence parameters given a typical image resolution of 2.5mm. In addition, depending on the particular position in the turbulent region, the degree of underestimation varies with the VEG frequency. Higher VEG frequencies are shown to reduce the underestimation. At the maximum frequency given by the maximum slew rate and gradient strength available on clinical MRI systems, significant underestimation of turbulence parameters remained. Increasing the voxel size, however, is expected to counteract this effect and may even result in overestimation of turbulence parameters[138]. Estimation of the mean velocity was not affected, besides misregistration errors due to finite time duration of the VEG.

Current turbulence quantification models[11] assume that the Lagrangian correlation time scale is much longer than the time duration of the VEG. In the current manuscript, based on CFD simulations assuming realistic flow regimes and viscosity, the first zero crossing of the VACF was found before 1ms, which relates to correlation time scales shorter than typical VEG durations. In vitro experiments using a blood fluid analog report the first zero crossing around 3ms[131], depending on the temporal phase of the pulsatile flow and

the position upstream of their artificial aortic valve. Other in vitro[158] and in vivo[149] works report significant energy density above 500Hz in their spectra.

On current MRI systems, the v_{enc} value is set by the user while gradient timings are optimized depending on other sequence parameters. As the spectral response depends on the VEG duration, such an approach does not provide full control for quantifying turbulence parameters. For VEG of 900Hz ($t_{dur} \approx 1$ms), it was found that the turbulence parameter estimation uncertainty for a range of VACF spectra can exceed ±10% in addition to the systematic, quantitative underestimation of turbulence parameters.

It is important to note that, depending on the duration of the VEG, estimation of turbulence parameter results in different values. This effect is not dependent on v_{enc} and cannot be completely corrected for without information of both the VEG spectrum and the velocity autocorrelation function (VACF) spectrum.

To address systematic underestimation of turbulence parameters using VEGs, a method using velocity-compensated waveforms has been presented. Velocity-compensated gradients (VCGs) exhibit a narrow peak in the gradient spectrum and hence are suitable for encoding and reconstructing the VACF spectrum with improved accuracy. Comparison to spectra of simulated probes yielded very good agreement. As VACF spectra vary spatially in turbulent flows[145], the presented method holds potential to correct for systematic errors in turbulence quantification on a voxel basis.

To ensure applicability of the correction method in practice without the need for additional measurements, the possibility of correction using only VEG spectra without probing the VACF spectrum was investigated. It was found that the RST estimates could be corrected to be coherent throughout different VEG frequencies.

Limitations

The current work is limited in terms of its restriction to non-pulsatile flow boundary conditions in the CFD simulation. However, as the MRI simulation concerned with VEGs focuses on the velocity encoding time span ($t_{dur} \leq 2$ms), realistic aortic inlet conditions would only result in negligible changes of flow rate during ${t_{dur}}^2$. Of note, the VEG MRI simulation itself employs time-varying input data from CFD. The 2D MRI simulation with input data from 3D CFD does not consider through-plane velocities. Nevertheless, as the evaluation only included in-plane parameters, no effects on the results are to be expected. No noise or coil sensitivities were simulated. Due to limited slew rates, depending on their frequency, VEGs or VCGs may have small gradient amplitudes which hamper the applicability in a real experiment due to the presence of noise. In vitro experiments and optimized waveforms[159] will be subject to future research. While the VCG waveforms used in this work respected gradient slew rate / amplitude limits of available MRI gradient systems, they employed increased encoding times ($t_{dur} = 20$ms). Accordingly, echo times are long leading to reduced SNR due to T_2* decay. Practical investigation of SNR related limitations of turbulent flow encoding using VCGs are planned for our future research.

The reference segment $v_{enc} = \infty$ and encoded segments $v_{enc} \neq 0$ have not been separated in time during the simulation process. As readout effects were the focus of another work[39]

and have not been considered, no signal attenuation and phase accumulation result for $v_{enc} = \infty$, rendering the reference segment start time independent. If readout effects were to be considered, particle tracing must be performed for $v_{enc} = \infty$ and $v_{enc} \neq 0$ segments separately and input data time frames must be separated depending on the assumed interleaving strategy of the MRI sequence.

Assumptions about the VACF spectra are based on CFD results using realistic flow parameters, however, the VACF spectrum may differ from the simulated spectra in reality. The probing of VACF spectra in vitro will be a subject of future research. Previous works[36] employed a similar particle tracing approach, but did not provide any information about VACF spectra. The current work is employing a discrete random walk model (DRW), however, alternatives such as continuous random walk (CRW) models could be used[160]. In addition, altering the viscosity of the working fluid changes the VACF spectrum, which hampers comparability of different works. In this work, the viscosity of whole blood and a realistic Reynolds number was used, intended to mimic in-vivo flow parameters.

Relying on a particle tracing approach, particles' dynamics influence the simulation results. Rather than imposing specific particle parameters (e.g. particle drag force outlined in Equation (4.53)), mass-less particles were used. These particles do not suppress any dynamics which may be important for tracing, however, are susceptible to gradients of the mean velocity field. To overcome this limitation, mean velocity variation correction was applied (Supplementary Information Figure S3 online).

4.9 Conclusion

Theoretical considerations and computer simulations as presented in this work suggest that bipolar velocity encoding gradients in phase-contrast MRI of stenotic flows with short correlation times result in systematic and significant underestimation of turbulence parameters. To address this shortcoming, tailored velocity-compensated gradients are proposed to offer an approach to improved quantitative mapping of turbulent blood flow characteristics.

4.10 Appendix

Derivation of the Ensemble Mean Phase

If a Gaussian distribution with first and second order moments different from zero ($n = \{1, 2\}$) is assumed, Equation (4.3) can be simplified to

$$E(t) = \exp\left[\underbrace{-\int_0^t \langle \mathrm{j}\varphi(t_1)\rangle \,\mathrm{d}t_1}_{1} + \underbrace{\tfrac{1}{2}\int_0^t \int_0^t \langle\, \mathrm{j}\varphi(t_1)\mathrm{j}\varphi(t_2)\rangle_{LC} \,\mathrm{d}t_1 \mathrm{d}t_2}_{2}\right] . \tag{4.29}$$

Assuming a stationary ensemble, the integral and ensemble average of term 1 in Equation (4.29) is given as

$$\int_0^t \langle \mathrm{j}\varphi(t_1)\rangle \,\mathrm{d}t_1 = \mathrm{j}\gamma \int_0^t \vec{G}(t') \cdot \overline{\vec{r}(t')} \,\mathrm{d}t' . \tag{4.30}$$

Term 2 in Equation (4.29) can be written as[136]

$$\langle\, \mathrm{j}\varphi(t_1)\mathrm{j}\varphi(t_2)\rangle_{LC} = \langle\, \mathrm{j}\varphi(t_1)\mathrm{j}\varphi(t_2)\rangle - \langle\, \mathrm{j}\varphi(t_1)\rangle\langle\, \mathrm{j}\varphi(t_2)\rangle \;, \tag{4.31}$$

where the first term on the RHS is given as

$$\langle\, \mathrm{j}\varphi(t_1)\mathrm{j}\varphi(t_2)\rangle = -\gamma^2 \int_0^t \int_0^t \vec{G}(t_1)\cdot\overline{\vec{r}(t_1)\;\vec{r}(t_2)}\cdot\;\vec{G}(t_2)\;\mathrm{d}t_1\mathrm{d}t_2 \tag{4.32}$$

and the second term, again, assuming a stationary ensemble with $\langle\, \mathrm{j}\varphi(t_1)\rangle = \langle\, \mathrm{j}\varphi(t_2)\rangle$, results in

$$\langle\, \mathrm{j}\varphi(t_1)\rangle\langle\, \mathrm{j}\varphi(t_2)\rangle = \left[\gamma \int_0^t \vec{G}(t')\cdot\;\overline{\vec{r}(t')}\;\mathrm{d}t'\right]^2 \;. \tag{4.33}$$

The location correlation[133] in Equation (4.31) is denoted by index LC and corresponds to the definition of the standard deviation ($\sigma^2 = \langle w^2\rangle - \langle w\rangle^2$ or $\sigma^2 = \mathbb{E}(w^2) - \mathbb{E}(w)^2$). Combination of Equation (4.32) and (4.33) results in an expression for the signal of an ensemble of magnetization with Gaussian distribution according to

$$E(t) = \exp\left[-\mathrm{j}\,\underbrace{\gamma \int_0^t \vec{G}(t')\cdot\overline{\vec{r}(t')}}_{\varphi_0(t)+\varphi_v(t)}\,\mathrm{d}\tau - \underbrace{\tfrac{1}{2}\gamma^2 \int_0^t\int_0^t \vec{G}(t_1)\cdot\overline{\vec{r}(t_1)\;\vec{r}(t_2)}_{LC}\cdot\vec{G}(t_2)\;\mathrm{d}t_1\mathrm{d}t_2}_{\alpha(t)}\right] \;. \tag{4.34}$$

Autocorrelation Function of Turbulent Flow

As defined in the main manuscript, the autocorrelation of a random process u is given by

$$R(t_1,t_2) = \langle u(t_1)\;u(t_2)\rangle \;, \tag{4.35}$$

where the angle brackets denote the mean (in ergodic processes either ensemble or temporal). In the case of a stationary random process only the time difference $\tau = t_2 - t_1$ matters resulting in

$$R(\tau) = \langle u(t)\;u(t+\tau)\rangle \;. \tag{4.36}$$

Following Kundu et al.[117], the normalized autocorrelation function is defined as

$$r(\tau) = \tfrac{\langle u(t_1)\;u(t_2)\rangle}{\langle u^2\rangle} \;. \tag{4.37}$$

If the autocorrelation function decays to zero for infinite times, it is possible to define the convergent integral

$$\tau_c = \int_0^\infty r(\tau)\,\mathrm{d}\tau \;. \tag{4.38}$$

If the random variable of interest is the vector-valued velocity, the two-point velocity autocorrelation function (VACF) can be defined as

$$VACF_{m,n}(\tau) = \langle u'_m(t)\;u'_n(t+\tau)\rangle \;, \tag{4.39}$$

where $u'_{m,n}$ denote the velocity fluctuations for spatial indices m,n. The two-point cross correlation of the velocity fluctuation forms a Fourier transform pair with the Lagrangian energy spectrum $E(\omega)$

$$E_{m,n}(\omega) = \tfrac{1}{2\pi}\int_{-\infty}^{\infty} R_{m,n}(\tau)\;\mathrm{e}^{-i\omega\tau}\,\mathrm{d}\tau \tag{4.40}$$

$$R_{m,n}(\tau) = \int_{-\infty}^{\infty} E_{m,n}(\omega)\ \mathrm{e}^{i\omega\tau}\,\mathrm{d}\omega\ . \tag{4.41}$$

The kinetic energy of turbulent fluctuations per unit mass[112] is defined as

$$k = \tfrac{1}{2}\langle u'_m\ u'_m\rangle = \tfrac{1}{2}\left\langle {u'}^2_m\right\rangle\ , \tag{4.42}$$

which has the unit $[k] = 1\ \mathrm{m}^2/\mathrm{s}^2$. The turbulent kinetic energy as used in 4D Flow MRI literature is defined as

$$TKE = \rho k = \frac{\rho}{2}\left\langle {u'}^2_m\right\rangle\ , \tag{4.43}$$

where ρ is the density and $[TKE] = 1\,\frac{\mathrm{J}}{\mathrm{m}^3}$.

It is found by setting $\tau = 0$ and $m = n$

$$\left\langle {u'}^2_m\right\rangle = \int_{-\infty}^{\infty} E_{m,m}(\omega)\,\mathrm{d}\omega\ , \tag{4.44}$$

$$k = \int_{0}^{\infty} E_{m,m}(\omega)\,\mathrm{d}\omega\ , \tag{4.45}$$

such that TKE per unit mass corresponds to the area under the Lagrangian energy spectrum curve. This emphasizes the importance of probing the VACF spectrum to its full extent in order to quantitatively estimate TKE in 4D Flow MRI.

Derivation of Spectrum

Starting with the expression for $\alpha(t)$ given in Equation (4.5) (repeated here for convenience)

$$\alpha(t) = \tfrac{1}{2}\gamma^2 \int_0^t \int_0^t \vec{q}(t)\cdot\overline{\vec{v}(t)\ \vec{v}(t+\tau)}_{LC}\cdot\vec{q}(\mathrm{t}+\tau)\ \mathrm{d}\tau, \tag{4.46}$$

the factors can be permuted using the rule $b\otimes(Ta) = (b\otimes a)T^{\mathrm{T}}$, where the symmetry of the velocity autocorrelation function matrix $\overline{\vec{v}(\tau_1)\ \vec{v}(\tau_2)}_{LC} = \left(\overline{\vec{v}(\tau_1)\ \vec{v}(\tau_2)}_{LC}\right)^{\mathrm{T}}$ is leveraged by inserting of Equation (4.9) into Equation (4.46);

$$\alpha(t) = \tfrac{1}{2\pi}\gamma^2 \int_0^t \int_0^t\ \vec{q}(t)\vec{q}(t+\tau)\int_{-\infty}^{\infty} D_{m,n}(\omega)\,\mathrm{e}^{\mathrm{j}\omega\tau}\,\mathrm{d}\tau\ \mathrm{d}\omega\ . \tag{4.47}$$

Assuming gradient signals of limited energy and being deterministic, the Wiener-Khintchine theorem can be applied yielding

$$\int_{-\infty}^{\infty} \underbrace{\vec{q}^*(t)\vec{q}(t+\tau)}_{R_q(\tau)}\ \mathrm{d}\tau = \tfrac{1}{2}\int_{-\infty}^{\infty}|q(\omega,t)|^2\,\mathrm{e}^{\mathrm{j}\omega t}\,\mathrm{d}\omega\ , \tag{4.48}$$

where the complex conjugate can be neglected since the integrated gradient waveforms are real-valued. Therefore, it is found that the autocorrelation function $R_q(\tau)$ of the gradient is given by the absolute Fourier coefficients $q(\omega,t)$ being squared resulting in the expression for $\alpha(t)$ as in Equation (4.10) with

$$S(\omega,t) = |q(\omega,t)|^2\ . \tag{4.49}$$

Self-similar flows, Reynolds number, Viscosity

When comparing different flow scenarios, the dimensionless Reynolds number

$$Re = \frac{ud}{\nu} \tag{4.50}$$

is used, where u, d and v are the mean inlet velocity, the unoccluded diameter and the dynamic viscosity, respectively. For self-similar flows, if the Reynolds number is kept the same, the resulting solution will be the same for appropriately scaled (= normalized) variables[112]. Of note, this enables one to compare experiments with e.g. different viscosities if the Reynolds number is equal by using appropriately scaled velocity variables. Important to note, however, is that non-normalized variables such as TKE and eddy frequency *are not comparable* without prior scaling. Therefore, simulations conducted with same *Re* but smaller viscosity will exhibit smaller TKE than those with higher values of viscosity.

The dimensionless Strouhal number

$$St = \frac{2\pi fd}{u} \tag{4.51}$$

is used as normalized "frequency" axis in CFD spectra plots (e.g. [145] and [143]), where f, d and u are the non-normalized frequency, minimum diameter (stenotic throat) and mean velocity at the stenosis throat (e.g. 4x mean inlet velocity for 75% reduction in area).

However, when changing viscosity but *Re* number and *Str* axis remain unchanged, one finds the non-normalized frequency axis f to be scaled by viscosity. Of note, this changes f_{eddy} at which e.g. the inertial range starts. The transition frequency f_{eddy} is of great importance for encoding theory discussed in the main manuscript.

Particle Equations of Motion

The equations of motion for an inert particle model are given by[161]

$$\frac{\mathrm{d}u_p}{\mathrm{d}t} = F_D(u - u_p) + g_x \frac{\rho_p - \rho}{\rho_p} + F_x \quad , \tag{4.52}$$

where the first RHS term denotes the drag force per unit particle mass and

$$F_D = \frac{18\mu}{\rho_p d_p^2} \frac{C_D Re_p}{24} \quad , \tag{4.53}$$

where u, u_p, μ, ρ, ρ_p, d_p, Re_p and C_D is fluid phase velocity, particle's velocity, molecular viscosity of the fluid, fluid density, particle density, particle diameter, particle Reynolds number and drag coefficient, respectively. Previous works have shown that these parameters have an influence on particle dynamics[161]. As F_D essentially describes how fast the particle would adjust its velocity to the fluid velocity, the particle's trajectory is affected by the set parameters, especially for particle tracing in turbulent flow. In the current manuscript, massless tracer particles have been used. On one hand, this does not use any assumptions on particle parameters, on the other hand, due to instantaneous velocity changes due to $u - u_p$, in the MRI simulation, spatial gradients in the mean velocity field will result in increased levels of imaged turbulence. This is discussed in the main manuscript in the mean velocity variation (MVV) section and accounted for in the Results section.

5 MRI System Characteristics

The main requirements for MRI are a strong, homogeneous main magnetic field (described by magnetic flux density $\vec{B}_0$), time-varying magnetic field gradients in three orthogonal directions ($\vec{G}_x, \vec{G}_y, \vec{G}_z$) and components for radio frequency (RF) transmission and reception. An overview of the components is given in Figure 5.1.

5.1 Mechanical Setup

The main magnetic field of current clinical MRI systems is generated by superconducting coils cooled by liquid helium at very low temperatures. Super conduction permits very high current density resulting in high magnetic field strengths while thermal insulation and controlled cooling allow for minimal temperature drift[63]. Sufficient homogeneity of the main field is ensured both by active shielding and shim coils was well as passive shimming depending on the specific system configuration.

Separate gradient coils for each axis respectively are mounted on glass fiber reinforced plastic, stacked along their common axis and linked by epoxide resin to increase stiffness[63], inserted into the bore and cooled by a separate water circulation. Due to their common structure and strict demands on the linearity of the magnetic field gradient for imaging, small mechanical deflections of one coil can result in diminished gradient performance of the same or other gradient coils. In addition, heating of coils due to gradient intensive imaging sequence may change the mechanical properties of the structure[54,162].

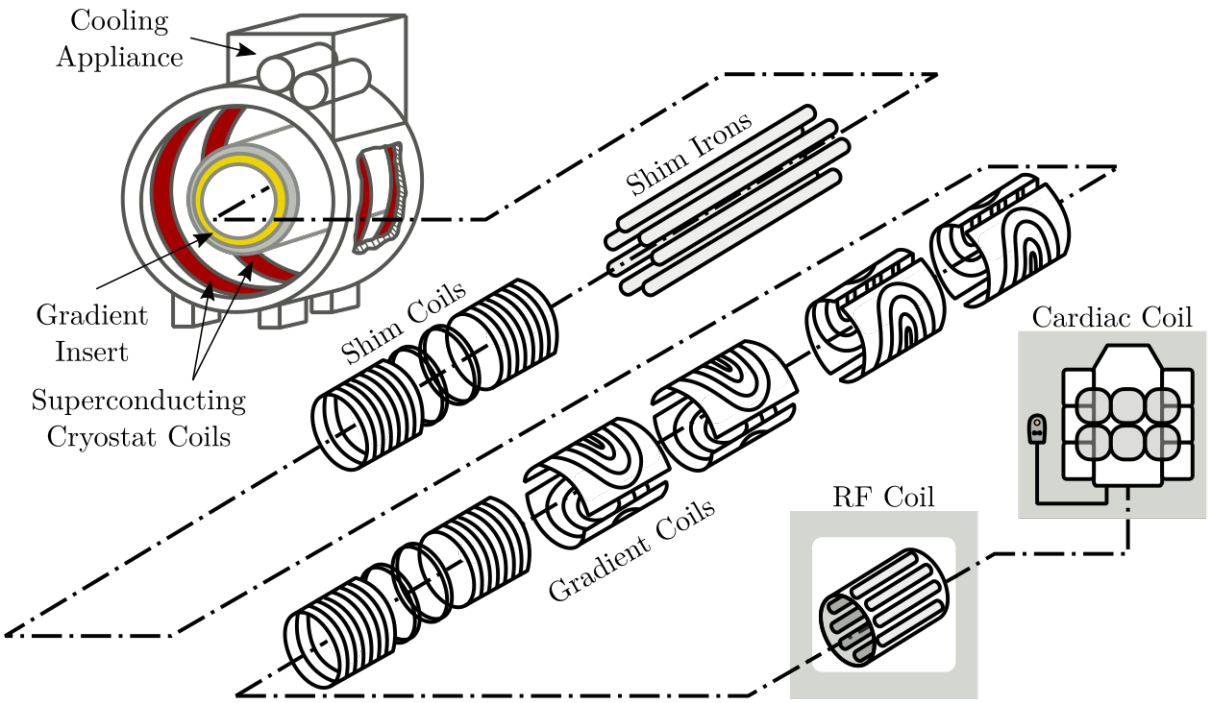

Figure 5.1: Simplified depiction of components of an MRI system. Superconducting coils in the cryostat create a strong main magnetic field aligned with the axial direction. Shim irons and coils are employed for increasing main field homogeneity. Gradient coils create time-varying magnetic field gradients. Radiofrequency transmit and receive (e.g. cardiac) coils are used for radiofrequency transmission and reception (Figure adapted from Allen D. Elster[163]).

5.2 Lorentz Forces

Current clinical MRI systems achieve magnetic field gradients in the order of 45 mT/m at slew rates of 200 mT/m/s by employing currents and voltages of 1 kA and 2 kV[63]. As the gradient coils are positioned within the main magnetic field, significant Lorentz forces $\vec{F}(t)$ given by

$$\vec{F}(t) = I(t) \int_{\mathcal{C}(t)} \mathrm{d}\vec{l} \times \vec{B}(t) \ , \tag{5.1}$$

result, where $I(t)$, $\mathcal{C}(t)$, $\mathrm{d}\vec{l}$ and $\vec{B}(t)$ denote the current in the gradient coil wires, the curve which is given along the wire, the directed infinitesimal length element and the magnetic flux density in which the wire is located, respectively. Complex mechanical modes in the gradient structure can be excited[44], where frequencies at which increased Lorentz forces occur result in high deflection amplitudes and are called mechanical resonance frequencies of the gradient system. The stiffness of the mechanical structure is intentionally increased during manufacturing to place mechanical resonance frequencies of the gradient system in a high frequency regime. Given the fast switching rates of gradients in EPI readouts, however, mechanical resonances may be excited.

5.3 Acoustic Noise

Deflections of the gradient system result in vibrations which generate sound pressure waves in the bore and examination room. The sound pressure level (SPL) of gradient intensive sequences can reach up to 133dB[164]. SPLs are known to be correlated to the gradient waveforms and are highly repeatable[165]. Double ear protection is advised to reduce SPLs in the ear canal, however, a significant SPL level can be experienced by mechanical coupling between the subject and the MRI system[166].

5.4 Characterization of Gradient Imperfections

Due to economical and practical limitations of manufacturing of gradient hardware, imperfections of the gradient chain[42,43,54] are to be expected. Concurrent field monitoring[167,168] allows to measure these imperfections. However, the approach requires additional hardware adding a significant financial overhead. To this end, one-time characterization of the gradient characteristics using dedicated MRI sequences may be used as an alternative.

By assuming the gradient system to be linear and time invariant (LTI), a single in / multiple out (SIMO) gradient impulse response function (GIRF) $h_{m,n}(\vec{r},t)$ can be defined. Due to the characteristics of the gradient system, the desired spatially invariant gradient $G_m(t)\ \vec{e}_m$ played on a single axis $m=\{x,y,z\}$ (i.e. in the direction of $\vec{e}_m$) results in spatially varying gradients $G'_n(\vec{r},t)=\int_{t_0}^{t} h_{m,n}(\vec{r},t-\tau)\ G_m(\tau)\ \mathrm{d}\tau$ on several axes $n=\{x,y,z\}$. Of note, the spatial dependence of $G'_n(\vec{r},t)$ is undesired as it disturbs the linear mapping in the reconstruction model given in Equation (3.3). In order to characterize the spatial dependence of the GIRF and circumvent the necessity of incorporating it separately in the reconstruction model, spatial basis functions are fitted[168,169]. Assuming a first order spatial fit, the modified k-space trajectory

$$\vec{k}'(t)=\gamma\int_{t_0}^{t}\left[G'_0(\tau),G'_x(\tau),G'_y(\tau),G'_z(\tau)\right]\ \mathrm{d}\tau \tag{5.2}$$

with the modified spatial position $\vec{r}'(t)=[1,\vec{r}(t)]^{\mathrm{T}}=[1,r_x(t),r_y(t),r_z(t)]^{\mathrm{T}}$ yields the signal model

$$d(\vec{k},t)=\int_{\mathcal{V}} M_{xy}(\vec{r},t)\ \mathrm{e}^{\alpha(\vec{r},t)}\ \mathrm{e}^{\mathrm{j}\varphi(\vec{r},t)}\ \mathrm{e}^{\mathrm{j}\vec{\mathrm{k}}'(t)\cdot\vec{r}'(t)}\ \mathrm{d}\vec{r}+\text{noise}\ . \tag{5.3}$$

As it can be seen, the phase contribution due to $G'_0(\tau)$ in the signal model is not dependent on the spatial position $\vec{r}(t)$. It is referred to as term contributing to the main magnetic field described by the magnetic flux density $\vec{B}_0$, which is also considered to be spatially invariant.

Analogous to the GIRF description in the time domain, the characteristics of the gradient system can be described in the frequency domain by the gradient modulation transfer function (GMTF). The GMTF is defined given a desired gradient spectrum $G_m(\nu)\ \vec{e}_m$ played on axis $m=\{x,y,z\}$ resulting in a spatially varying gradient spectrum $G'_n(\vec{r},\nu)\ \vec{e}_n$ as

$$GMTF_{m,n}(\vec{r},\nu) = \frac{G'_n(\vec{r},\nu)}{G_m(\nu)}\ , \tag{5.4}$$

where ν denotes the normalized frequency. The notation includes self-terms such as $GMTF_{m,m}(\vec{r},\nu)$ (ideal case: $GMTF_{m,m}(\vec{r},\nu) = 1\ \forall\nu$), but also contributions to cross-talk between axes such as $GMTF_{m,n}(\vec{r},\nu)$ for $m \neq n$ (ideal case: $GMTF_{m,n}(\vec{r},\nu) = 0\ \forall\nu$ and $m \neq n$). Similar to the description of the GIRF, spatial basis functions of first order are fitted for $GMTF_{m,n}(\vec{r},\nu)$ resulting in zeroth-order terms $GMTF_{m,B0}(\nu)$ and first-order order terms $GMTF_{m,n}(\nu)$, which are both spatially invariant.

Currently available correction approaches for gradient system imperfections employ an open-loop control approach where a set of fixed pre-emphasis filters are applied to the desired gradient waveforms at scan time for each axis. Given the long-term stability of the GMTF[55], this is a valuable approach, however the temperature dependence can have significant effects on PC-MRI even for shorter scans[162]. In addition, the characteristics of the gradient system may vary on a time scale comparable to TR and are not compensated.

5.5 Implications of Mechanical Motion during Spatial Encoding

In Section 1, changes in the position of isochromats $\vec{r}(t)$ were identified as a source of erroneous phase resulting in inconsistencies of the assumed and actual k-space trajectory data. In addition, deviations from the desired temporal evolution of the magnetic field gradient $\vec{G}(t)$ and deflection of the gradient coils result in a non-linear mapping between k-space and sampled data. If the magnetic field gradient behavior is not accurately predicted or monitored, these deviations may result in non-negligible image artefacts. Of note, effects from gradient imperfections can be dependent on the distance of the isochromat from the isocenter of the magnet. This includes non-zero order eddy currents[170], concomitant fields[171], static field inhomogeneity[172] or spatial nonlinearity effects[173].

Even though the resonant behavior of gradient coil structures has been subject to many simulations and experiments[174–187,187–192] (secondary references taken from Winkler et al.[44]), its implication for imaging has not been satisfactorily discussed in the literature. In addition, the excitation of a stiff mechanical system near its eigenfrequency results in a superimposed beat phenomenon[193], which, in addition, renders the gradient amplitude time dependent. This aspect is subject to Section 5.6, where the mechanically resonant behavior of the gradient structure is demonstrated using measurements of the beat phenomenon during spatial encoding.

5.6 Beat Phenomena in MRI - Theoretical and Experimental Description of the Impact of Mechanical Resonances on Fast Readouts

Introduction

Fast readout strategies such as echo planar[194] or spiral imaging employ rapidly switching gradient waveforms during extended acquisition windows which are subject to B0[195], susceptibility[196] and trajectory imperfection artefacts[55]. Previous work by Kasper et al.[197] has employed concurrent field monitoring and observed periodic variations of the signal phase when using EPI trajectories. The authors concluded that these field fluctuations

have a non-negligible impact on the resulting images and attributed this effect to heating of the gradient coils. In the present work, we propose a different theoretical explanation of the beat phenomenon and validate it by phantom experiments and simulations.

Theory

In previous works light has been shed on the mechanically resonant behavior of MRI gradient systems[198] and its impact on PC-MRI gradient-echo sequence design[199]. Oscillating readouts, on the other hand, such as EPI or spiral trajectories, relate to forced excitation of (several) second-order systems (mechanical resonances). Following Lifschitz and Landau[193], it is found that the deflection must follow a beat phenomenon whose amplitude is modulated over time with a period that equals the inverse of the difference frequency (Figure 5.2A), if the excitation frequency is near the natural frequency (= mechanical resonance frequency, Figure 5.2B).

Given that the gradient modulation transfer function (GMTF) exhibits peaks at the mechanical eigenfrequencies in both 1st (symmetric around isocenter) and 0th order terms (shift of isocenter, Figure 5.2C), in theory, both terms can be monitored such that

$$\Delta\varphi(t) \propto \Delta k_{1st}\; x + \Delta B0_{0th}\; t\;, \tag{5.5}$$

where $\Delta\varphi(t)$ represents the erroneous phase, Δk_{1st} the erroneous kspace position due to 1st order GMTF terms, x the spatial position, $\Delta B0_{0th}$ the erroneous B0 offset due to 0th order GMTF terms and t the acquisition time. It is known that 1st and 0th order terms result in k-space shifts[199] and phase accrual over acquisition time, respectively.

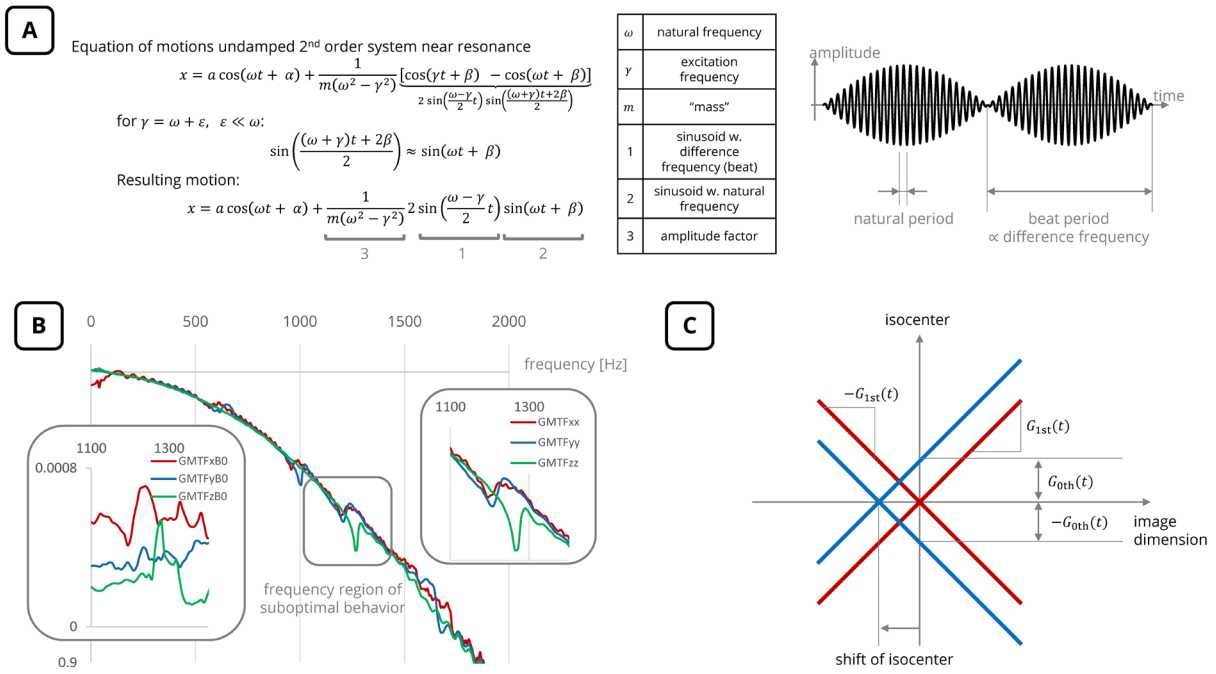

Figure 5.2: (A) Equations of motion for a forced excitation of an undamped system of 2nd order. (B) GMTF of S1 showing suboptimal frequency regions due to mechanical resonances. (C) 0th order components relate to a shift of the isocenter.

Methods

A vendor supplied EPI sequence (Figure 5.3A) was employed to acquire a non-oblique slice of a stationary spherical phantom on two 3T MRI systems (S1, S2) of the same model (Philips Healthcare, Best, the Netherlands) at {S1: isocenter offset by 5.5cm} {S2: at isocenter}. The readout bandwidth (EPI BW) was varied between 1121Hz and 1579Hz in 24 steps by adjusting the water-fat shift (WFS) in pixels, keeping echo time (TE) constant. The phase encoding blips were deactivated such that $ky(t) = 0 \; \forall \; t$. This allows monitoring the readout process of the y-projected image over time (ky profiles). The frequency encoded direction (gradient axis along which the EPI waveform will be played out) was set to either z (S1,S2) or y (S2).

In order to distinguish between $\Delta B0$ arising from spatial variations of the main magnetic field and $\Delta B0_{0th}$ from the GMTF, for every EPI BW the gradient waveforms were played out with normal (WFS1) and inverted sign (WFS2). The resulting image phases were subtracted such that $\Delta B0$ would cancel out (Figure 5.2C). Shimming was optimized to minimize dephasing due to long readout durations.

To isolate the effects due to $\Delta B0_{0th}$ rather than Δk_{1st}, the phases of even and odd echoes were subtracted such that the phase portion $\Delta k_{1st} \; x$ would cancel out.

Data was reconstructed using MRecon (GyroTools LLC, Winterthur, Switzerland) without EPI phase correction and inverse Fourier transform in ky direction.

A GMTF of both systems was acquired[169] (for S2: in the same scan session) to identify the mechanical resonances of the systems.

The acquisition process was simulated in MATLAB R2019a (MathWorks, Natick, MA), assuming a simplified EPI readout trajectory with a beat amplitude modulation.

Results & Discussion

Figure 5.3 presents (B) a B0 map and magnitude images and (C) the reconstructed GMTF of 0th order for systems S1 and S2.

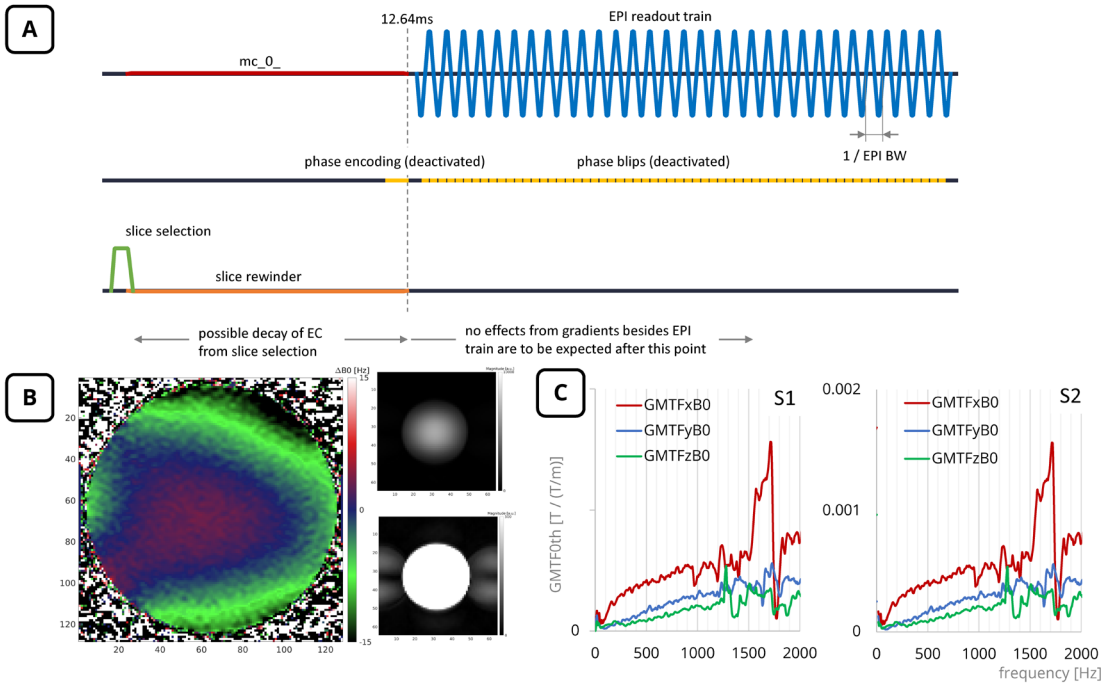

Figure 5.3: (A) EPI sequence used in conjunction with deactivated phase-encoding blips. (B) B0 map; magnitude image including rescaled version acquired with the EPI sequence. (C) GMTFs of 0th order for systems S1 and S2, which are comparable due to the same system architecture.

In Figure 5.4, phase difference planes for varying EPI BW for S1 and S2 are depicted (mean of the surface has been subtracted for better interpretability). As expected, a beat of varying frequency in the ky profile direction (= over time) can be seen. Also, the beat amplitude increases over time as predicted due to $B0_{0th}$ phase accumulation.

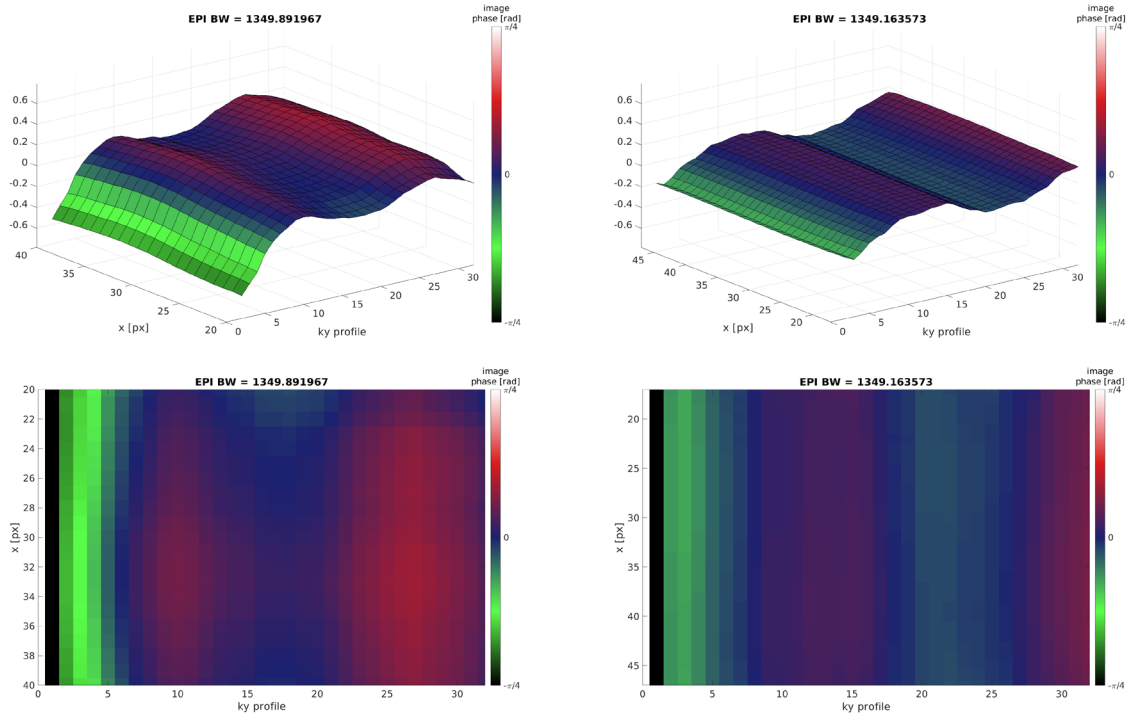

Figure 5.4: Phase difference maps for varying EPI BWs for S1 (left column) and S2 (right column). A beat phenomenon which varies with EPI BW can be observed and is explained by forced excitation of a mechanical resonance. The mean of the phase maps has been subtracted respectively for aiding visual display. The animated image version can be found online.

In Figure 5.5, the beat frequency in the data is related to the difference of the mechanical resonance and the excitation frequency for an axis with a single mechanical resonance (z axis) as described in the Theory section. The results hold for varying EPI BW. In addition, it is found also for axes with multiple resonances (y axis, Figure 5.5C) that multiple beat phenomena are super positioned.

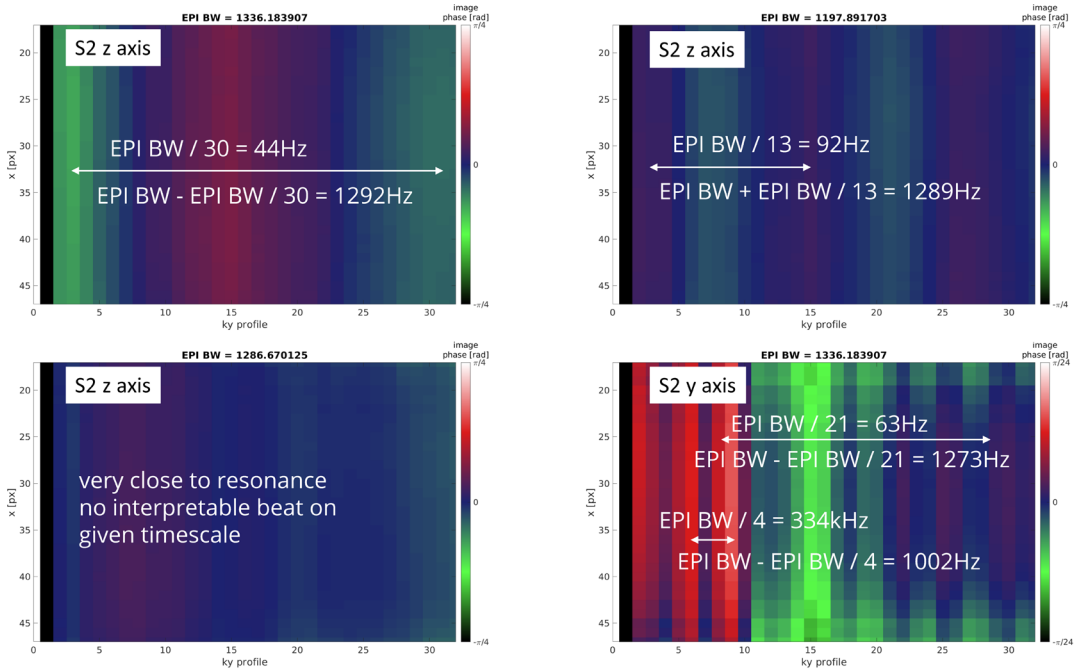

Figure 5.5: Evaluation of the beat frequency which relates to the difference frequency given in Figure 5.2A. Despite some uncertainty of localising the maxima in the phase maps, the mechanical resonance frequency can be determined. Bottom right: for axes with several mechanical resonances, superpositioning of beat phenomena is observed and evaluated.

In Figure 5.6, the simulation output is shown where qualitatively the same beat as in the experiments can be observed. Differences in beat amplitude can be explained by the difference in the simulated versus the actual EPI trajectory and the amplitude factor given in Figure 5.2A. Comparing nominal and beat magnitude images for a slotted phantom, varying signal pile up is found which relates to blurring phase encoding direction if blips would be employed.

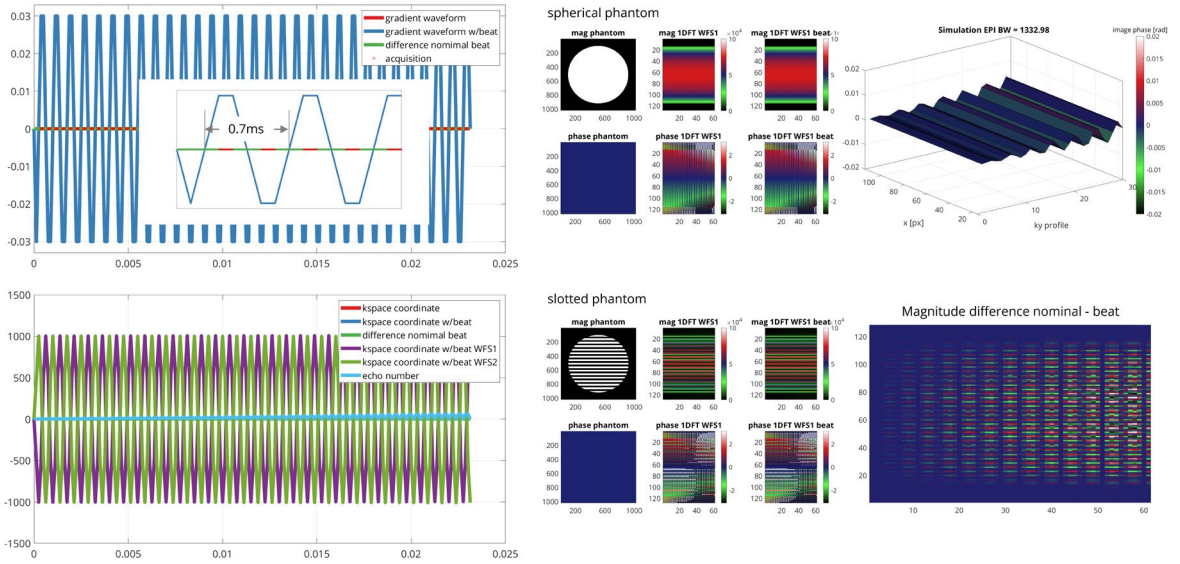

Figure 5.6: Simulation output assuming a simplified EPI trajectory. For a spherical phantom, a similar beat phenomenon as in the experiments can be observed. For a slotted phantom varying signal pile up across the image dimension is found which relates to blurring if phase blips would be employed.

Conclusion

In this work, we identified GMTF 0th order terms arising from mechanical resonances as a source of erroneous, time-varying B0 phase when employing EPI readouts. The beat phenomenon, which was observed in other works[197], is explained by forced excitation of mechanical resonances of the MRI gradient system. Sequence design and correction methods could benefit as pre-emphasis on current MRI systems is based on oscillating compensation terms with constant amplitude over time.

5.7 Implications of Mechanical Motion due to Velocity Encoding

As presented in Section 1.3, the phase modulation function is given by (repeated here for convenience)

$$\varphi(\vec{r},t) = \varphi_{prep}(\vec{r},t) + \varphi_{background}(\vec{r},t) + \varphi_{system}(\vec{r},t) \ , \tag{5.6}$$

where $\varphi_{prep}(\vec{r},t)$ denotes phase contribution due to velocity while $\varphi_{background}(\vec{r},t)$ and $\varphi_{system}(\vec{r},t)$ denote undesired sample related and system characteristic phase contributions, respectively. $\varphi_{background}(\vec{r},t)$ and $\varphi_{system}(\vec{r},t)$ were assumed not dependent on the velocity encoding during t_{prep} itself and would cancel out after complex division of images from two acquisitions with different first moments.

The bipolar gradient $\vec{G}_{prep}(t)$ used for velocity encoding can be considered a single period of a square-like waveform with duration T_{MEG} resulting in a fundamental frequency $f_{MEG} = 1/T_{MEG}$. As presented in Section 5.6, the gradient system exhibits characteristics of a stiff mechanical system which, if f_{MEG} and a resonance frequency f_{res} coincide, renders the assumption that $\varphi_{system}(\vec{r},t)$ does not depend on the velocity encoding invalid. Due to long-lived mechanical deflections as a result of mechanical excitation of the system

using the velocity encoding gradient, $\varphi_{system}(\vec{r}, t)$ does not cancel out and results in an erroneous, time varying phase component. This is referred to as "Intra-TR" effects in Section 5.8 and depicted in Figure 5.7.

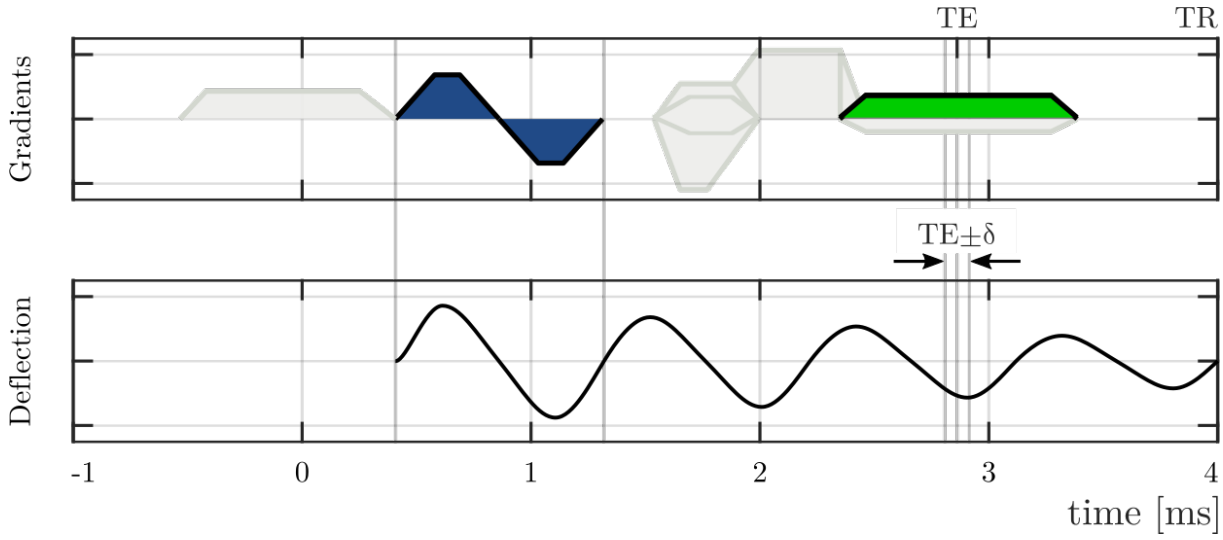

*Figure 5.7: Schematic depiction of **Intra-TR** effects. Due to its unfavorable chosen timing, the bipolar gradient used for velocity encoding excites a mechanical resonance resulting in deflection of the gradient assembly over time. Depending on the amplitude and slope of the deflection around the echo time TE, undesired background phase and misalignment artefacts in the resulting image occur.*

In fact, due to the repetitive nature of MRI sequences, the mechanical excitation can even swing up resulting in further increased deflection amplitudes if the resonance condition (positive feedback) $TR = n\ 1/f_{res},\ n \in \mathbb{N}$ is met. This is referred to as "Inter-TR" effects in Section 5.8 and should not be confused with spoiling related issues[200]. As depicted in Figure 5.8, by setting the repetition time TR to TR' accordingly, the resonance condition can be interrupted for a single mechanical resonance frequency. In Section 6, evaluation of the gradient modulation transfer function yields multiple mechanical resonances exist at different frequencies for each axis respectively. However, even if the resonance condition may be met only for a single mechanical resonance on one gradient axis, several encoding directions may be affected depending on the velocity encoding interleaving strategy.

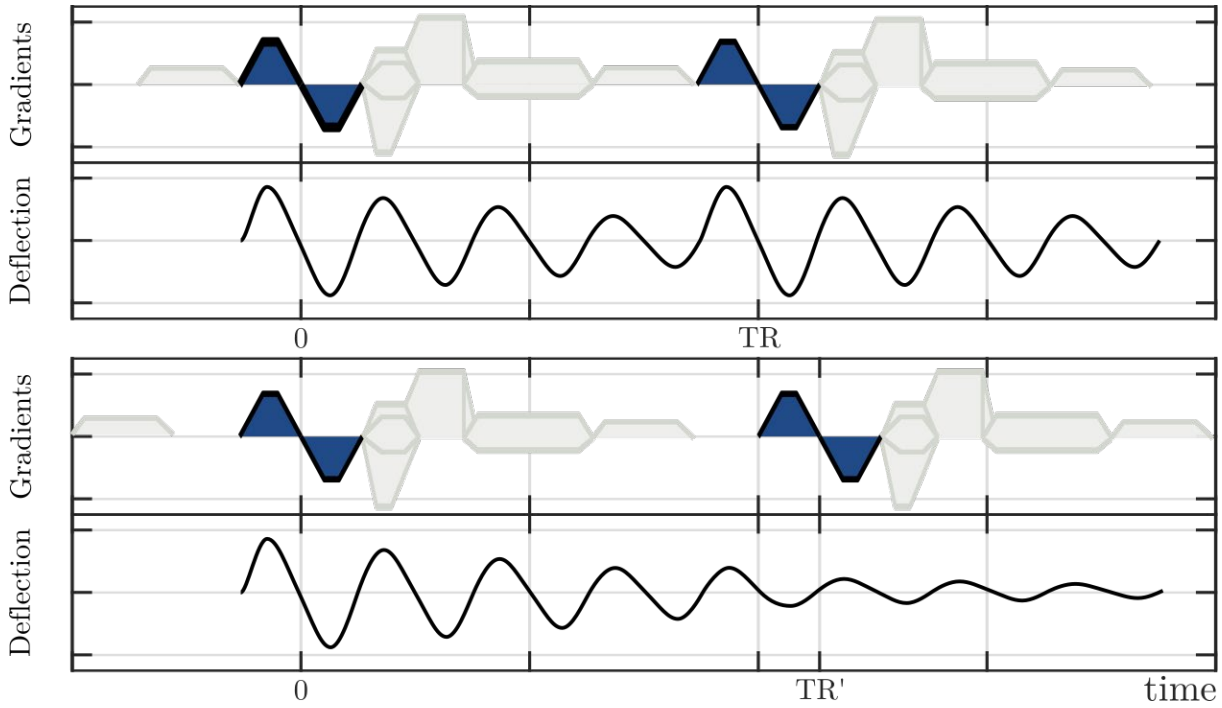

*Figure 5.8: Schematic depiction of **Inter-TR** effects. Due to unfavorable chosen repetition time TR and bipolar gradient timing, the mechanical oscillation is excited over several TRs resulting in a swing up of the deflection amplitude. By extending the repetition time to TR′, the swing up of deflection is suppressed. Given typical bipolar gradient timings in the order of 0.5ms, the maximum prolongation of TR is given by 0.25ms.*

If the undesired phase component $\varphi_{system}(\vec{r},t)$ does not cancel after phase subtraction, it contributes to $\varphi(\vec{r},t)$ and distort the estimated velocity. As result, velocity images comprise non-zero velocities in VOI regions where static tissue would be expected.

The temporal evolution of the zeroth moment for spatial encoding $\overrightarrow{m}_0(t)$ and contributions $\widetilde{\overrightarrow{m_0}}(t)$ due to $\varphi_{system}(\vec{r},t)$ is given by

$$\overrightarrow{m}_0'(t) = \overrightarrow{m}_0(t) + \widetilde{\overrightarrow{m_0}}(t) = \int_{t_0}^{t} \underbrace{\vec{G}(t') + \tilde{\vec{G}}(t')}_{\vec{G}'(t')} \, \mathrm{d}t' \ , \tag{5.7}$$

where $\vec{G}'(t) = \vec{G}(t) + \tilde{\vec{G}}(t)$ denotes the temporal evolution of the gradient played out including the intended and undesired contributions $\vec{G}(t)$ and $\tilde{\vec{G}}(t)$ at time t during $\mathrm{t_{prep}}$ and $\mathrm{t_{enc}}$, respectively. According to the relation properties of k-space (Fourier space) and image space, a pure offset of $\overrightarrow{m}_0'(t)$ corresponding to a time shift of the spatial encoding process, for example by $\tilde{\vec{G}}(t') = \mathrm{const}\ \forall t$, results in a spatial phase ramp in image space. Depending on the amplitude and slope of $\widetilde{\overrightarrow{m_0}}(t)$ in a region around the echo time $TE \pm \delta$, where $\delta \ll TE$, resulting phases may be of higher spatial order. Of note, the region $TE \pm \delta$ corresponds to low spatial frequencies in image space, therefore deviations of $\overrightarrow{m}_0'(t)$ from the ideal temporal evolution of $\overrightarrow{m}_0(t)$ at $TE \pm \delta$ are highly undesirable.

For practical VOI sizes, the incorrectly estimated velocity can reach up to 10% of v_{enc}[52]. This is in contrast to clinical requirements for the estimation of stroke volume from cardiac MRI, which limits the acceptable error to less than 0.4% of v_{enc}[45].

Subsequently, correction methods have been proposed based on polynomial fitting of different orders of phase in regions of static tissue, where no phase due to velocity encoding is to be expected[201]. Current approaches employ polynomials up to fourth order[202], where Busch et al. have shown that the limited amount of static tissue in the VOI and the combination of low SNR and high order polynomial fitting hamper the practicability of the correction[103]. Therefore, in order to increase the accuracy of PC-MRI estimated velocities, minimization of the amplitude and order of the background phase is desired. This could be achieved by optimizing gradient waveforms such that no resonances are excited, however, this may pose impractical limitations on sequence design. Another approach by increasing *TE* by a short time interval to minimize the deflection at *TE* and adapt *TR* such that resonance condition for positive feedback is invalidated are practically feasible and evaluated in Section 5.8. As presented in Section 6, mechanical resonance frequencies are correlated with peaks in the SPL spectra, which enabled the identification of mechanical resonances exclusively by mobile phone audio recordings in Section 5.8.

5.8 Background Phase Error Reduction in Phase-Contrast MRI based on Acoustic Noise Recordings

Introduction

Velocity biases in phase-contrast (PC) velocity mapping, such as 4D flow MRI, can compromise accuracy and reproducibility[29]. These offsets stem from phase differences between the flow encoded and reference segment and are due to unwanted, non-flow sources. Giese et al.[52] demonstrated that the phase offset is influenced by mechanical resonances of the gradient system. Despite the availability of valuable approaches for background phase error correction and sequence optimization[203], clinical acceptance with a maximum phase offset of 0.4% of venc[45] may only be achieved when applying higher order corrections[103]. In this work we demonstrate background phase error reduction by acoustic noise-guided adjustment of the echo and repetition time of PC sequences.

Theory

Switching of electric currents leads to Lorentz forces acting on the gradient coils (Figure 5.9A). The deflection results in a change of the magnetic field gradient, which is identified as a peak in the Gradient Modulation Transfer Function (GMTF). The mechanical resonance causes the gradient system to vibrate, which results in acoustic noise (Figure 5.9B). This enables the identification of mechanical resonances by acoustic noise measurements.

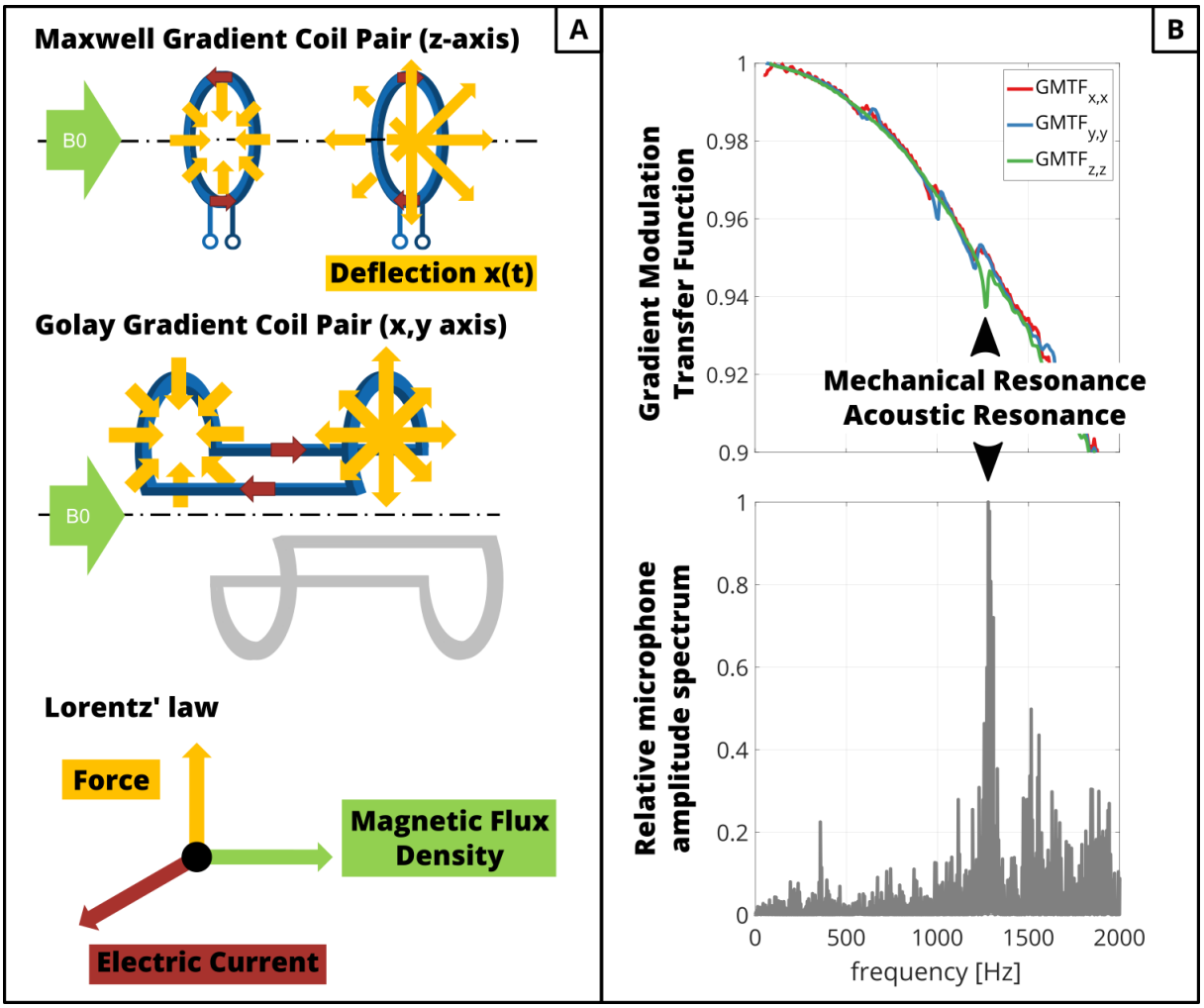

Figure 5.9: (A) Rapidly switching electric currents in the gradient coils cause mechanical deflection according to Lorentz' law. The deflection causes the magnetic field gradient to oscillate with mechanical resonance frequencies. These can be identified (B) using either the Gradient Modulation Transfer Function (GMTF) or the Relative Microphone Amplitude Spectrum (RAMS). Of note, the RAMS during scanning can be acquired without special equipment (audio recording with mobile phone).

Changes in the magnetic field gradient lead to an erroneous k-space position $\Delta\vec{k}(t)$ (Figure 5.10A). In phase-contrast images, $\Delta\vec{k}(t)$ is given by the changes in gradient waveforms between encoded and reference segments (bipolar gradient). Depending on $\Delta\vec{k}(TE)$ at echo time TE, the k-space center is shifted resulting in phase ramps in the direction of flow encodings. We term this error "intra-TR effects" and distinguish between "good" TEs ($\Delta\vec{k}(TE) = 0$) or "bad" TEs ($\Delta\vec{k}(TE) = \max$), with small or large phase ramps in image space, accordingly. If the inverse of the bipolar gradient duration coincides with a mechanical resonance frequency (f_{res}, Figure 5.10A,C), it is likely that the resonance is excited.

Due to the repetitive nature of MR sequences, the gradient waveform spectrum and the audio spectrum are inherently multiplied by frequency comb $f_{comb} = 1/TR$ (TR: repetition time; Figure 5.10B). If comb maxima coincide with peaks of the mechanical resonance spectrum, constructive interference occurs and all axes can be influenced. We term this

behavior "inter-TR effects". Depending on the resonance frequency f_{res}, we can distinguish between "bad" *TR*s (overlap of f_{res} and f_{comb}) and "good" *TR*s (no overlap).

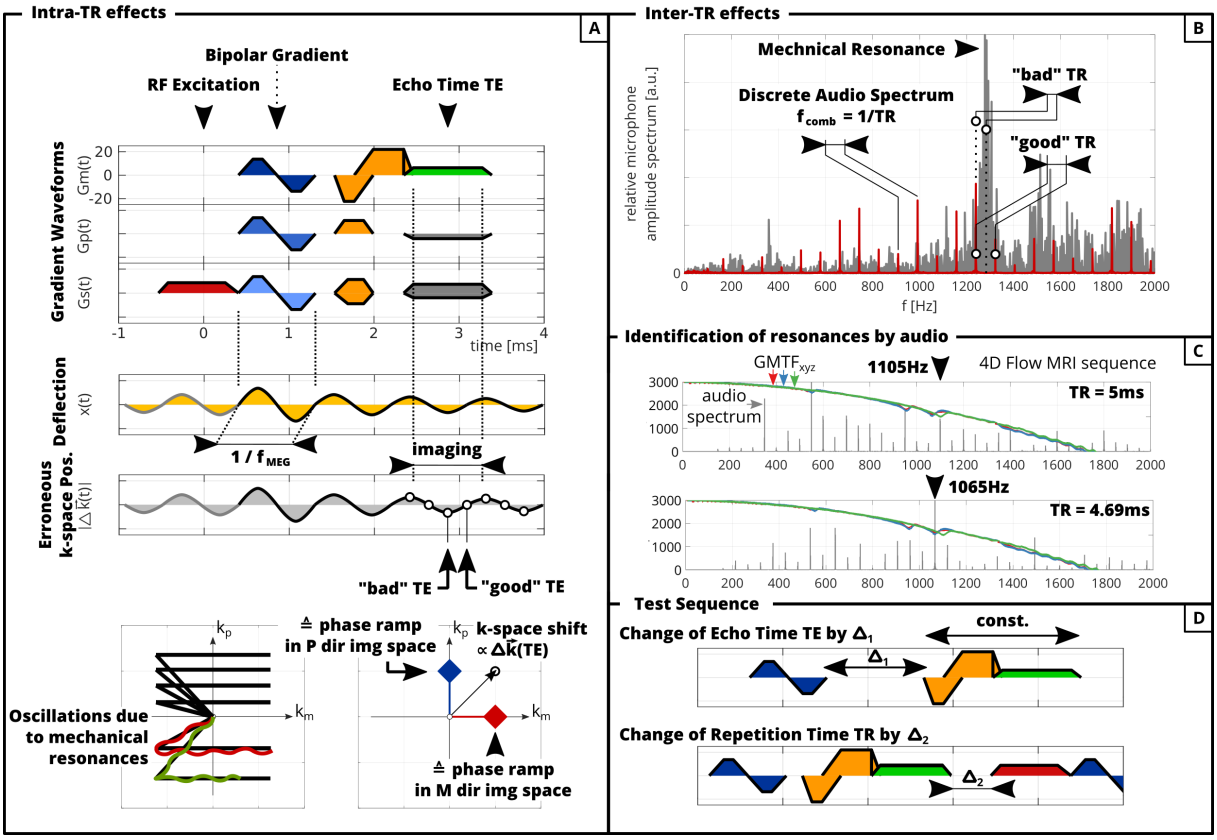

Figure 5.10: (A) Gradient waveform frequency coinciding with a mechanical resonance frequency results in an erroneous k-space position causing a phase ramp in image space. This effect is limited to one TR (intra-TR). (B) The repetitive nature of MRI sequences lead to a discrete audio spectrum. If frequency comb and the mechanical resonances overlap, deflection can build up from TR to TR (inter-TR). (C) 4D Flow MRI sequence for identification of mechanical resonances. (D) GRE test sequence.

Methods

A gradient-echo sequence[204] (Figure 5.10A,D) was adapted to include bipolar motion encoding gradients (MEG) of frequency f_{MEG} to acquire sagittal, non-oblique 3D PC MRI images with referenced flow encoding. A static phantom (TX/water,1:12 doped with 0.16ml/l Gadolinium, $T1 \approx 1s$) was scanned on a 3T system (Ingenia; Philips Healthcare, Best, the Netherlands) and offset from the isocenter (32mm in M,P). The acquisition was interleaved in a ky-kz-flow-encoding manner and reconstructed using MRecon (GyroTools LLC, Winterthur, Switzerland). Concomitant field correction was performed and coil channels were combined after complex division of the flow encoding segments.

Two scan sets were acquired for which the bipolar gradient frequency was matched to one of two mechanical resonance frequencies ($f_{res} = \{1065\text{Hz}, 1105\text{Hz}\}$ Figure 5.10C) derived from audio recordings. Scans were repeated for different combinations of *TE* and *TR*. To measure "intra TR" effects with varying *TE*, a time delay Δ_1 was introduced (Figure 5.10D) by shifting all gradients after the MEG towards the end of the sequence.

To measure "inter TR" effects with varying TE, a time delay Δ_2 at the end of each sequence block was inserted, keeping TE constant.

For the audio recording, a mobile phone (iPhone6; Apple Inc., Cupertino, CA, USA) was placed inside the scanner room and its voice recorder was used (sampling rate: 44.1kHz). Recordings were Fourier transformed and normalized to the mean of their spectrum. A vendor-supplied 4D Flow MRI sequence ($v_{enc} = 100$cm/s, asymmetric encoding) was played exclusively for identifying mechanical resonances (Figure 5.10C). Due to its flow-first interleaving strategy, its comb frequency is given by $1/(4TR)$.

In order to quantify the image phase, a polynomial of first order was fitted to 1D centered profiles along frequency and phase encoding direction and resulted in a slope (Figure 5.11, Figure 5.12; red broken lines, value given in the plots) for each TE, TR.

Results & Discussion

Figure 5.11 presents the spatial phase evolution for fixed $TR = 5$ms ($f_{res} = 1065$Hz not on frequency comb, Figure 1C) and compares $TE = 2.35$ms (good) vs. $TE = 2.97$ms (bad). Depending on the flow encoding direction, increased slopes of the first order fit result are noted in the corresponding profile direction. Orthogonal profiles do not differ between TEs.

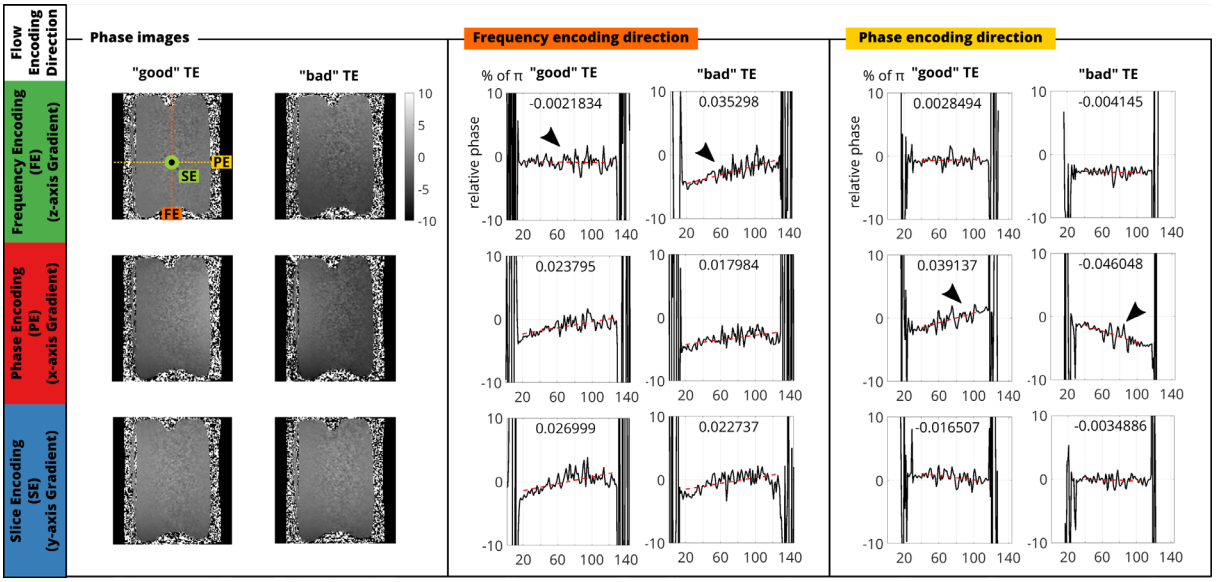

Figure 5.11: Comparison of TE=2.35ms ('good') and TE=2.97ms ('bad') for same TR=5ms and MEG frequency 1065Hz. Reconstructed phase images are shown together with profiles along FH (frequency encoding direction) and AP (phase encoding direction) and corresponding linear fit (red dashed line). For bad TE, we find an increased phase ramp compared to good TE (black arrows). As for intra-TR effects, complying with the Theory section, flow encoding in M direction only influences FH direction for bad TE.

Figure 5.12 presents the spatial phase evolution for fixed $TE = 2.35$ms and compares $TR = 5$ms (good) vs. $TR = 4.69$ms (bad). The slope is increased in phase encoding direction between good and bad TR (x3.6). Flow encoding in phase and slice encoding direction results in quadratic background phase in frequency encoding direction.

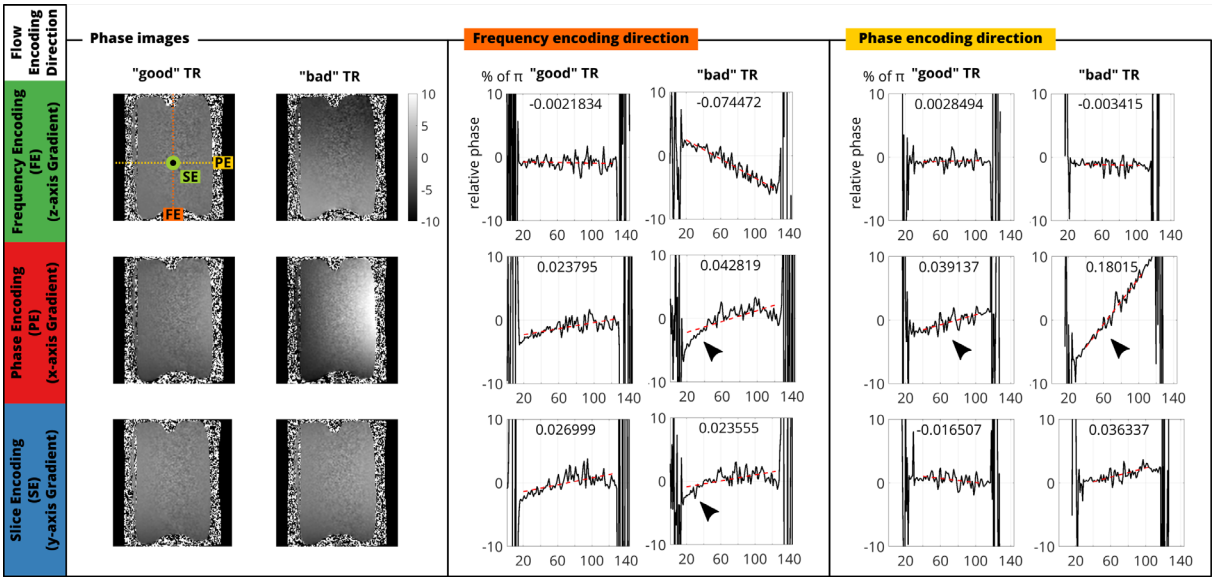

Figure 5.12: Comparison of TR=5ms ('good') and TR=4.69ms ('bad') for TE=2.35ms and fMEG=1065Hz. Phase images are shown with profiles along frequency- and phase-encode direction (FE/PE) and corresponding linear fit (red line). For "bad" TE, an increased slope is seen, which is quadratic in the FE direction (arrows). As predicted for inter-TR effects, flow encoding in one axis influences other axes. Of note, X and Y gradient axes (Golay pairs) show similar behaviour due to similar mechanical properties.

In Figure 5.13, the slope of the fit is presented for varying *TE*s and two MEG frequencies 1105Hz and 1065Hz with $TR = 10$ms and $TR = 5$ms, respectively. Only the phase profile in flow-encode direction changes its slope. The period of the change is given by $1/f_{res}$ and complies to Figure 5.10A. We find increased slopes of up to 15-fold when comparing "good" to "bad" *TE*.

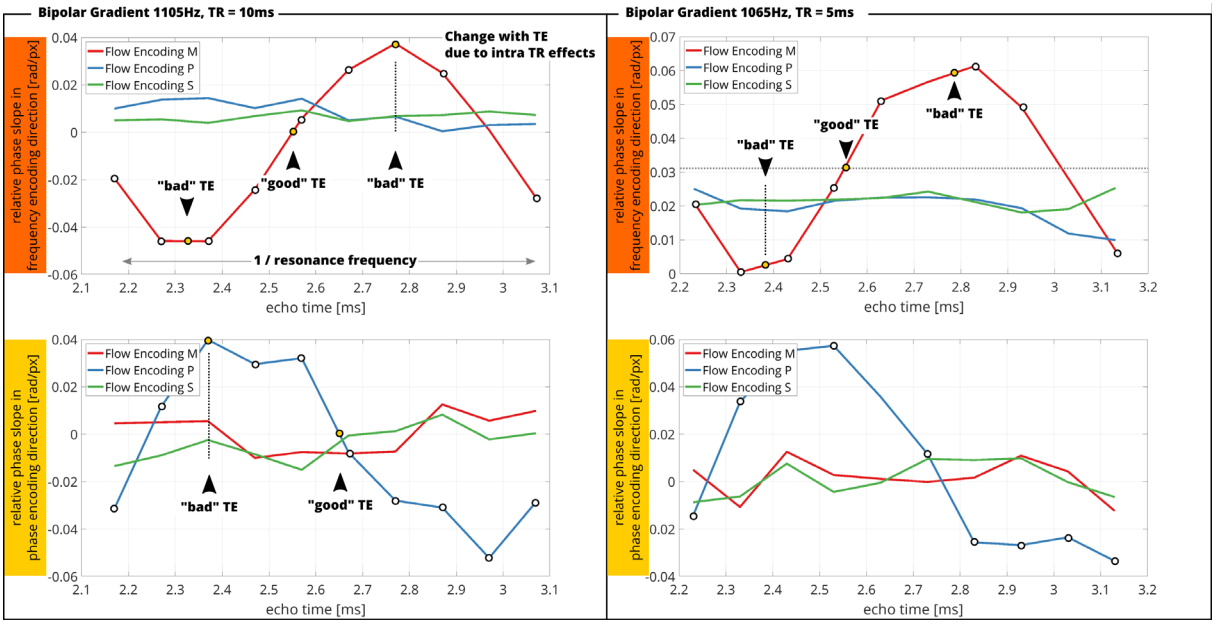

Figure 5.13: Background phase slope vs TE with fixed TR for MEGs at resonance frequencies 1105Hz and 1065Hz. A sinusoidal dependence of the phase ramp slope can be observed, which is attributed to the erroneous k-space position introduced in Figure 5.10A. The periodicity is approximately given by the reciprocal of the resonance frequency. Increased slopes are found in the direction of flow encoding, whereas other directions are not influenced (Intra-TR effects, Figure 5.11).

Conclusion

In this work, we identified mechanical resonances as a source of erroneous background phases when using PC-MRI. By mapping mechanical resonances using simple audio recordings before imaging, we were able to identify beneficial combinations of *TR* and *TE* for which the background phase error was kept minimal. For suboptimal choices of *TR*, the spatial background phase resulted in quadratic dependencies. By shifting *TE* by 0.6ms or *TR* by 0.31ms, we were able to achieve a minimal background phase. For future MRI systems, audio recordings could be used to track mechanical resonance frequencies during short preparation phases to fine-tune sequence parameters.

5.9 Signal-to-Noise in MRI

The signal model in Equation (1.1) is based on the transverse magnetization $M_{xy}(\vec{r},t)$ which is at maximum equal to the equilibrium magnetization given by

$$M_{eq} = \frac{1}{2}\hbar\gamma\rho P \ , \tag{5.8}$$

where $\hbar$, γ, ρ and P denote Planck's constant, the gyromagnetic ratio, the spin density and the polarization, respectively. The polarization is given by

$$P = \tanh\left(\frac{\hbar\gamma}{2k_bT}B_0\right) \ , \tag{5.9}$$

where k_b and T denote the Boltzmann constant and the sample temperature, respectively. As $\frac{\hbar\gamma}{2k_bT}B_0 \ll 1$ and $\frac{\hbar\gamma}{2k_bT} \ll B_0$ hold, $P \propto B_0$ and $M_{xy}(\vec{r},t) \propto B_0$ follows.

The voltage detected in an RF coil is therefore linearly dependent on the Larmor frequency $\omega = \gamma B_0$, which results in

$$\left|S(\vec{r},\vec{k}_v,\vec{q},t)\right| \propto \omega M_{xy}(\vec{r},t)\Delta V \propto B_0^2 \Delta V, \tag{5.10}$$

where ΔV is assumed to be the volume of a single voxel. The quadratic dependence of the signal on B_0^2 has motivated the design of high-field MRI systems utilizing magnetic flux densities even greater than 7 Tesla.

The noise voltage spectral densities (or termed noise variance) due to coil losses v_{coil}^2 and sample dissipation v_{sample}^2 are given by the Johnson noise formula[205]

$$\begin{aligned} v_{coil}^2 &\propto 4k_b R_{coil} T_{coil} \\ v_{sample}^2 &\propto 4k_b R_{sample} T_{sample} \ , \end{aligned} \tag{5.11}$$

where $R_{coil,sample}$ and $T_{coil,sample}$ denote the resistance and temperature of the coil and the sample, respectively. For a given acquisition bandwidth BW, the root mean square voltage (or noise standard deviation) of the sum of both losses is given as

$$\sigma_{noise} \propto \sqrt{4k_b(R_{coil}T_{coil} + R_{sample}T_{sample})BW} \ . \tag{5.12}$$

The resistances are found[206] to fulfil $R_{coil} \propto \sqrt{\omega}$ and $R_{sample} \propto \omega^2$, where sample noise dominates for magnetic flux densities greater than 1.5 Tesla[207] assuming clinical receive coil configurations. Therefore, amplifier and coil noise can be neglected assuming $B_0 >$ 1.5T resulting in $\sigma'_{noise} \propto \sqrt{\omega^2 BW}$.

Assuming constant temperature of amplifiers, coils and the sample, the signal-to-noise ratio (SNR) at spatial position $\vec{r}$ and at time t is given as

$$SNR(\vec{r},t) \propto \frac{|S(\vec{r},t)|}{\sigma'_{noise}} \propto \frac{\left|\omega M_{xy}(\vec{r},t)\Delta V\right|}{\sqrt{\omega^2 BW}} \propto \frac{|\mathrm{B}_0 \Delta V|}{\sqrt{BW}} \ . \tag{5.13}$$

Of note, the acquisition bandwidth BW is inversely related with the acquisition time T_{acq}, yielding an analogous definition of the signal-to-noise ratio

$$SNR(\vec{r},t) \propto |\mathrm{B}_0 \Delta V| \sqrt{T_{acq}} \ . \tag{5.14}$$

It can be seen that four-fold averaging of the signal increases SNR by the same amount as increasing the voxel size two-fold, for example.

To minimize flow artefacts, a minimum readout duration is desirable (highest bandwidth). However, the acquisition bandwidth has to be traded against the SNR. Based on the description of SNR, the velocity-to-noise ratio can be defined as

$$VNR(\vec{r},t) \propto SNR(\vec{r},t)\ \vec{k}_v \cdot \vec{v}(\vec{r},t) \ , \tag{5.15}$$

where $\vec{k}_v$ and $\vec{v}(\vec{r},t)$ denote the velocity encoding vector and the velocity, respectively. To maximize VNR given SNR, $\vec{k}_v$ must be maximized while fulfilling Equation (1.4).

5.10 Opportunities of Lower Field Systems

Scaling of the noise standard deviation for field strengths greater than 1.5 Tesla is dominated by sample noise resulting in $\sigma_{noise} \propto B_0$. However, as the field strength is reduced, the amplifier and coil noise become more important, weakening the linear

dependence of σ_{noise} on field strength. This offers the possibility of using improved low-noise amplifiers and cooling the circuits and coils to reduce their contribution to σ_{noise}.

The deposition of energy in the sample is described by the specific absorption rate (SAR), which, in terms of patient safety, is a particular concern at higher magnetic flux densities[208]. SAR is monitored and limits the performance of MRI systems which could be unleashed using the same hardware when neglecting patient safety limits. Due to $SAR \propto B_0^2$, a gain in flexibility for sequence optimization at lower B_0 emerges. The drawbacks of inherently lower SNR at decreased field strength[209] may be partly compensated by field-strength dependent changes of tissue properties[209], reduced susceptibility artefacts[210], shorter RF-pulses[211] (secondary reference from Marques et al.[209]) and reduced heating of metallic parts inside the body[212].

In addition, lower-field systems may be more cost-effective compared to standard field strength systems and can still employ high-performance gradient systems. For the latter, as the Lorentz force acting on the gradient coils is linearly dependent on the static field strength, better performance is to be expected for lower-field systems. Disadvantageous effects of Lorentz forces, resulting in mechanical motion of the gradient system, and possible approaches for sequence optimization by mitigating the excitation of mechanical resonances for standard field systems have been discussed in Section 5.6 and Section 5.8.

Lower-field systems (< 1.5T) should exhibit improved gradient accuracy as mechanical resonance amplitudes are reduced due to reduced Lorentz forces. In addition, sound pressure levels are expected to decrease for lower-field as Lorentz forces are reduced[213]. This could beneficially impact patient comfort and remove the need for hearing protection during MRI examinations. However, a direct comparison of gradient performance of the same MRI system at different field strengths has not been performed so far. Section 6 therefore focuses on the characterization of a clinical MRI at 0.75T and 3T configuration, providing evidence that mechanical resonance effects and sound pressure levels are in fact reduced.

6 Direct Comparison of Gradient Fidelity and Acoustic Noise of the Same MRI System at 3T and 0.75T

Hannes Dillinger[1], Sebastian Kozerke[1], Christian Guenthner[1]

[1] Institute for Biomedical Engineering, University and ETH Zurich, Zurich, Switzerland

Submitted to: *Magn Reson Med.*

6.1 Introduction

Acoustic noise during MRI examinations can limit the acceptance in particular by elderly or pediatric patients as they experience compromised comfort and may suffer from anxiety or even require sedation[214]. In addition, safety issues may arise during sequences exhibiting elevated sound pressure levels (SPL) up to 133dB at 3T including fMRI[164], diffusion-weighted imaging (DWI)[215] and Dixon-type water/fat imaging[216].

Besides contributions from subsidiary systems (vacuum pump etc.), acoustic noise during MRI examinations is dominated by rapidly switching gradients leading to changing Lorentz forces that act on the gradient coils themselves[214]. Hence, audio noise levels are dependent on sequence type and timings, field strength, and gradient coil design[165,213,214,217,218]. As vibrations deform the gradient coils, their magnetic field is modulated leading to deviations from the nominal k-space trajectory or temporal variations of the uniform static field[44]. In addition, the mechanical deflection may stimulate complex mechanical modes in the gradient coil and its supporting structures[44,192,219,220] of which some may couple vibroacoustically[221] resulting in large sound pressure levels (SPLs). Hence, noise levels can also be an indicator of gradient performance and fidelity, e.g. in fMRI, where louder EPI sequences resulted in field drifts and spurious motion artefacts[222]. Since the SPL is approximately linearly related to the logarithm of field strength (< 3T)[213], reduced field strength is accompanied by less acoustic noise emission and potentially higher gradient fidelity.

Given practical and economical design limitations of clinical MRI gradient hardware[42], magnetic field imperfections need to be characterized, mitigated, and ultimately corrected for by prospective[223–225] or retrospective methods[55]. Gold standard is concurrent field monitoring[226,227], which measures the magnetic field distribution in real time using dedicated field probes[227]. Even though research has been conducted on different probe materials[227,228], to the best of our knowledge, no concurrent field measurement system is available for lower field systems (< 3T) so far. Alternatively, dedicated MRI acquisition protocols can be used to measure the magnetic field distribution indirectly through its effect on the MR signal phase[229]. If the gradient system is assumed to be linear and time invariant (LTI), the definition of the Gradient Modulation Transfer Function (GMTF)[53] allows to derive magnetic field distributions from nominal gradient waveforms. GMTF-based trajectory corrections have been successfully applied to EPI and spiral readouts[55], shim preemphasis[230], and steady state imaging[49,50], which resulted in increased image quality. In addition, the GMTF is long-term stable[55] and thus allows for once-in-a-time system characterization and subsequent application. Violation of the LTI assumption was investigated by Nussbaum et al.[43], who measured nonlinearities in the gradient amplifier

chain. In addition, time invariance was found to be violated due to heating of the gradient coils[162]. Nevertheless, current monitoring and thermal modelling can be employed to reinstate the LTI condition[54].

The GMTF comprises the product of four main transfer functions[43] with contributions from: (a) amplifier and (b) gradient coil characteristics, (c) eddy currents, and (d) mechanical resonances. If the main field strength is altered while the hardware remains unchanged, gradient amplifier, gradient coil and eddy current characteristics remain constant. When ramping down a standard MRI system to lower fields, however, passive shims from standard configuration have to be partly reoptimized in order to increase main field homogeneity to an acceptable level[231]. This is achieved by altering the amount and placement of shim irons on the shim rails within the bore. Subsequently, the amount of conducting material around the gradient coils influences the resulting eddy currents. If not accounted for by adaptation of eddy current compensation parameters, changes in eddy current characteristics is to be expected.

Mechanical resonances result from Lorentz forces acting on the gradient coils, which are linearly dependent on the main field strength. Thus, upon field-strength change, the GMTF is expected to differ only at frequencies, where mechanical resonances occur apart from eddy current dependent characteristics.

In this work, we evaluate gradient fidelity and audio noise characteristics of the same MRI operated sequentially at 3T and at a lower field strength of 0.75T by comparing GMTFs and audio noise measurements. Special focus is put on the mechanical resonance frequencies of the gradient system.

6.2 Methods

Product Field Strength and Lower-Field Scanner Setup

All measurements were performed on a 3T Philips Achieva (Philips Healthcare, Best, the Netherlands) MRI with a gradient system delivering 200 T/m/s slew rate and a maximum gradient strength of 40 mT/m. A spherical phantom ("MRS Sphere with Solution Phantom", GE Healthcare, Chicago, IL, United States) was placed in the isocenter. Figure 6.1A presents a summary of the setup used for the product (3T) and lower-field (0.75T) configuration, respectively.

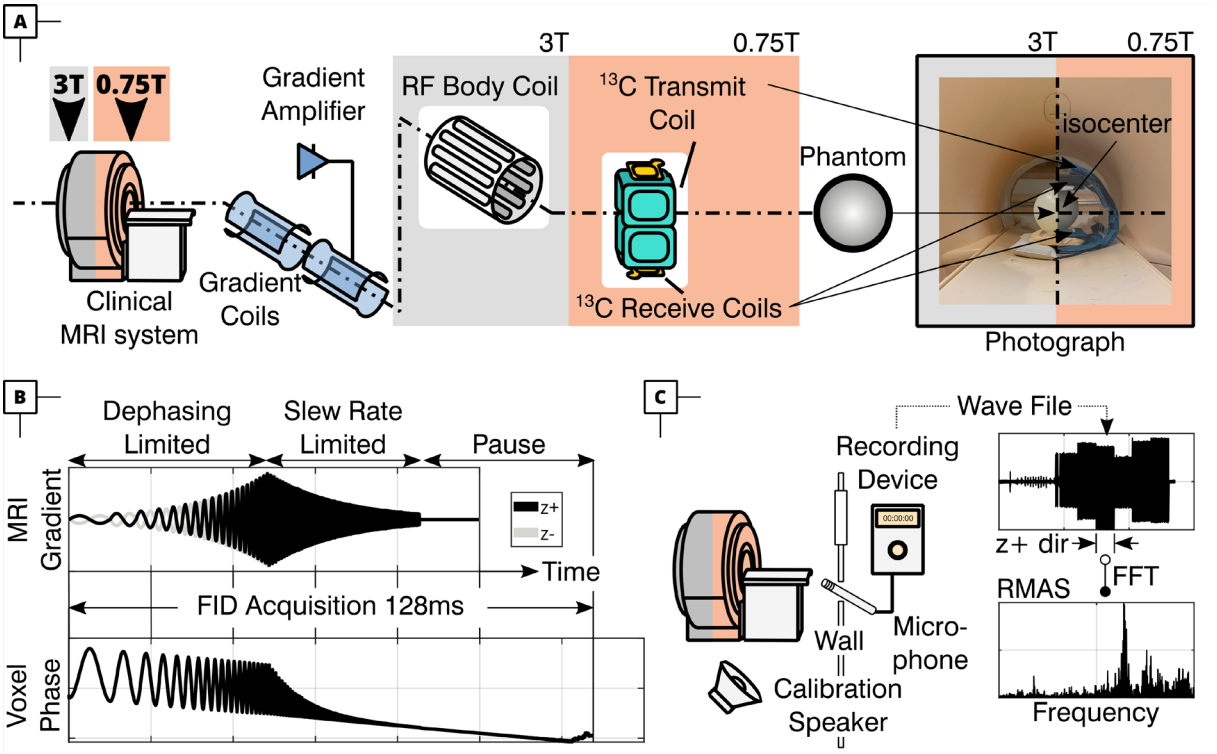

Figure 6.1: Schematic depiction of the methods. (A) A clinical MRI system was consecutively operated at its product (3T) and down-ramped (0.75T) configuration, while gradient amplifiers, gradient coils and phantom remained unchanged. For transmit & receive, the body coil (3T) and 3T-^{13}C coils (for ^{1}H at 0.75T) were used. (B) Designed chirp waveform for limited dephasing and maximizing signal in the low- and high frequency region, respectively. Data acquisition started at the beginning of the chirp and continued for a total time of 128ms. (C) The audio measurement setup consisted of a recorder and microphone positioned in the waveguide located in the radiofrequency cage of the scanner room. The recorded wave file was divided into snippets and Fourier-transformed to obtain relative microphone amplitude spectra (RMAS).

3T Product Field Strength System Configuration: The body coil was used for excitation and signal reception.

0.75T Lower-Field System Configuration: The magnet was ramped-down to 0.75T to allow use of the 3T-^{13}C channel of the Achieva's multi-nuclei interface for transmit and receive on protons at 32 MHz. To increase the main-field homogeneity, shim iron placement on the removable shim rails was reoptimized for the lowered field strength. For transmission, a custom-built double Helmholtz-like coil (Clinical MR Solutions, Brookfield, WI, USA) was employed, while a four-channel receive array (Clinical MR Solutions, Brookfield, WI, USA) with two posterior and two anterior elements was used for signal reception. The 3T body coil remained disconnected inside the scanner. Preparation phases including frequency determination, power optimization, and shimming were performed using the local transmit and receive coils. Eddy current related preemphasis parameters remained at their product field strength settings.

GMTF Measurement and Processing

A modification of the thin-slice method proposed by Rahmer et al. was used to measure the gradient modulation transfer function (GMTF)[169]. Four 2 mm slices were acquired symmetrically around the isocenter in an interleaved fashion using a multi-slice 2D spectroscopic imaging sequence. To achieve isotropic coverage, a slice gap of 34 mm was used and 7x7 voxels were phase-encoded with an effective in-plane resolution of 36 mm x 36 mm. The FID after the 90° excitation pulse was sampled at 512 kHz for 128 ms. Concurrent to the readout, in the direction of the slice-select gradient, a chirp gradient was played out for the first 85 ms. The pulse was designed by concatenation of sinusoids to discretely sweep from 100 Hz to 10 kHz, while adhering to gradient slew and strength limits as well as minimizing intra-voxel dephasing to a maximum of 20% signal loss (Figure 6.1B). The chirp pulse was played out with positive and negative sign to increase sensitivity and to remove phase contributions from off-resonance as well as lowest-order concomitant fields. To acquire the response for all three gradient axes, the entire acquisition scheme was rotated in succession to align slice-excitation and chirp-pulse gradients along the x, y, and z axes, respectively.

Raw data was stored using additional metadata and processed in MATLAB 2020b (Mathworks, Natick, MA, United States) using MRecon (Gyrotools LLC, Winterthur, Switzerland). Following the processing steps proposed in Rahmer et al.[169], singular value decomposition (SVD-)based coil compression was performed for the multi (lower-field) and single (standard configuration)-coil data after 3D Fourier transform[232]. The phase of the FID of each voxel was extracted and unwrapped in the temporal dimension. Phase differences of the opposing gradient sign measurements were obtained and then numerically differentiated using centered finite differences. Voxels were selected based on magnitude thresholding, removing any voxel with signal below 0.1% of the maximal signal amplitude at any temporal point. Zeroth- to third-order spherical harmonic basis functions were fitted using a weighted pseudo-inverse penalizing noisy voxel signals (for details see Rahmer et al.[169], Equation 3). The chirp waveform was adjusted to the acquisition sampling rate and acquisition duration by zero padding and upsampling using spline interpolation in the time domain. Finally, the GMTF was calculated as the measured response spectrum divided by the spectrum of the chirp.

To obtain an estimate of the eddy current characteristics, i.e. the low-pass behavior in the first-order GMTF self-terms, a heuristic model was fitted to the GMTF magnitude data. A polynomial of degree 8 was chosen, capturing low-pass behavior in the frequency range [50, 5000] Hz where SNR was acceptable for fitting and without reproducing mechanical resonances. Mechanical resonances (R) and anti-resonances (AR) were identified visually at the 3T configuration. Their relative amplitude was quantified by reporting difference values between polynomial fit and magnitude GMTF. This is referred to as magnitude difference (MD) in online Supplementary Information Table S2, where MD(A, B) is evaluated with A,B = {AR, R, fit}. For a comparison between field strengths, MD was evaluated at AR and R frequencies identified at 3T for GMTFs of 0.75T and 3T configuration, where the reduction of MD in percent between field strengths is given by $(MD_{0.75T}(AR, R) - MD_{3T}(AR, R)) / MD_{3T}(AR, R)$.

Audio Recordings

Sound pressure was recorded using a Sennheiser ME 66 microphone (Sennheiser, Wedemark, Germany) connected to a Tascam DR-100 recording device (Los Angeles, CA, United States). The microphone was positioned in the waveguide connecting the scanner with the control room (Figure 6.1C). Microphone amplitudes were calibrated at the beginning of each experiment by recording a 1kHz tone from a known audio source placed inside the scanner room below the waveguide. The sample rate was set to 48kHz mono and data was saved as uncompressed .wav files. The dependence of SPL on spatial position and linearity with gradient strength was investigated by Hamaguchi et al.[220] allowing to correlate our measurements with the SPL inside the bore.

The audio recording of the chirp sequence was divided into 6 audio snippets, each corresponding to the nominal and inverted chirp waveforms played out along the x, y and z axes. Fourier transform of the snippets resulted in relative microphone amplitude spectra (RMAS, see Figure 6.1C).

In addition to RMAS of the GMTF sequence, RMASs were obtained for exemplary clinical sequences (Cartesian Multi-Acquisition, MA; Multi-Echo Dixon, ME; and Spiral MA Dixon) to evaluate audio characteristics of the 0.75T and 3T configurations. Here, the timing at 0.75T was used for the acquisitions at 3T to enable direct comparison of audio levels.

6.3 Results

Figure 6.2 shows the estimated GMTF self-terms for 0.75T and 3T. The low-pass characteristics of the GMTF self-terms for x and y axis changed between standard and lower-field configuration whereas the influence on the z axis is negligible (fit curves shown in online Supplementary Information Figure S1). At frequencies of mechanical resonances, the lower-field configuration showed consistently decreased relative amplitudes (see also online Supporting Information Table S2 and Supporting Information Figure S3). The prominent z-axis magnitude differences of antiresonance and resonance with respect to the fitted curve at 1275 Hz was found to be reduced by 87% at 0.75T compared with 3T. Resonances of the x- and y-axis at 0.75T were reduced by up to 95% rendering them indistinguishable from the 0.75T low-pass behavior. Detailed data is listed online in Supporting Information Table S2, where magnitude differences for all marked resonances can be found. Online Supporting Information Figure S4 and S5 present the evaluation of antiresonances and resonances for 0.75T and 3T, respectively. Online supporting Information Figure S6 presents magnitude and phase of GMTF self-terms for 0.75T and 3T. Online supporting Information Figure S7 presents a zoom-in view. Online supporting Information Figure S8 shows GMTF cross-terms.

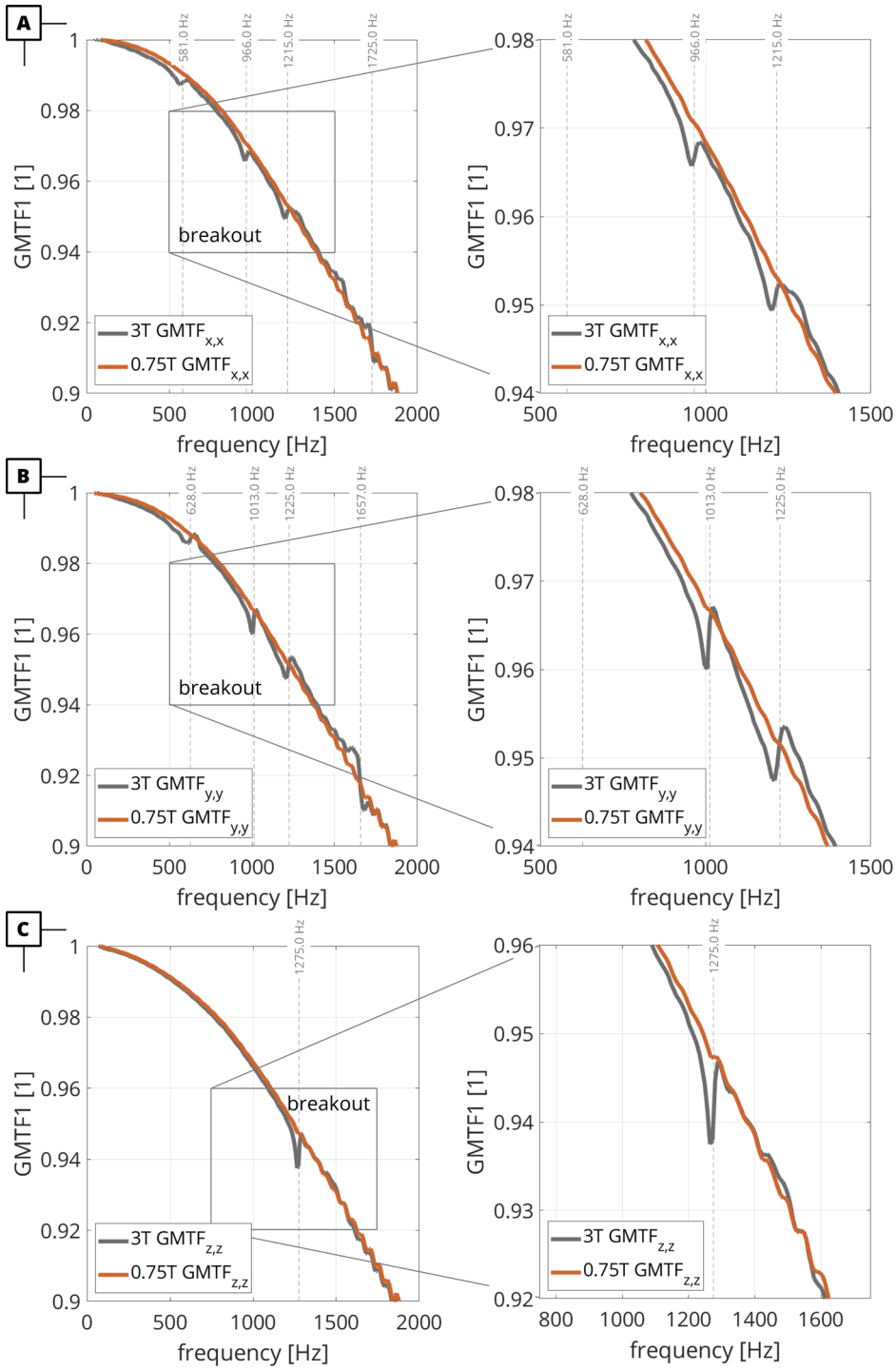

Figure 6.2: Comparison of Gradient Modulation Transfer Functions (GMTF) self-terms for the (A) x-, (B) y- and (C) z-axis for 0.75T (orange) and 3T (grey) configurations. Right column: Detailed views of breakout regions found in the left column. Mechanical resonances (dashed lines) are identified by local dips (anti-resonances) and peaks (resonances) in the GMTF that deviate from the ideal GMTF. A reduction by up to 95% for 0.75T is found for antiresonance / resonance magnitude difference on the x and y axes GMTFs and 87% on the z axis GMTF. The low-pass behavior of the GMTFs between field strengths is altered for x and y axes while changes in the z axis are negligible. Ripples at frequencies above approx. 1 kHz differ between 0.75T and 3T.

Figure 6.3 shows the zeroth-order GMTF terms, where the resonance in the x-axis at 1725 Hz dominates the spectrum for the 3T configuration. The peaks in the x-axis and z-axis spectrum correspond with the major mechanical resonances at 1725 Hz and 1275 Hz, respectively, and are correspondingly reduced at the lower-field configuration. For example, the z-axis GMTF peak to dip ratio for the resonance is reduced by 94% at 0.75T. For the x- and y-axis, the zeroth-order GMTF main characteristics remain similar, whereas for the z-axis the slope is reduced.

Figure 6.4 shows the GMTFs and corresponding relative microphone amplitude spectra (RMAS). Peaks in the RMAS correspond with the mechanical resonances in the GMTF and RMAS values are consistently lower at 0.75T. Peaks in the RMAS are found to be reduced for 0.75T compared to 3T by x-axis: 87% at 1221 Hz, y-axis: 72% at 1200 Hz and z-axis: 50% at 1279 Hz.

In Figure 6.5, RMAS for the vendor-supplied clinical three-point Dixon sequences are shown. Due to the repetitive nature of MRI sequences, a frequency comb is observed in the RMAS, which is given by the inverse of the sequence's periodicity, i.e. 1/TR for multi-echo and 1/(3TR) for multi-acquisition encoding (neglecting phase encode gradients). The integral over RMAS values in the depicted frequency region (up to 2 kHz, high sensitivity frequency region of human hearing[164]) is found to be reduced by factors of 4.14 (Figure 6.5A; Cartesian Multi-Acquisition Dixon), 3.80 (Figure 6.5B; Spiral MA Dixon), and 5.78 (Figure 6.5C; Cartesian Multi-Echo Dixon) between the 3T and 0.75T configurations, respectively.

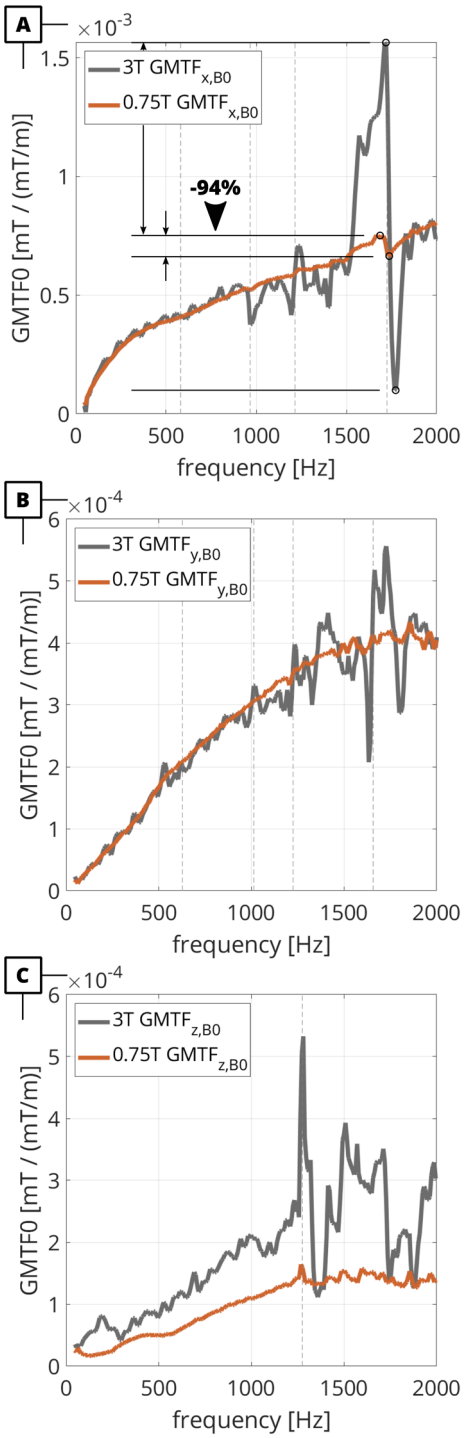

Figure 6.3: Comparison of the zeroth-order Gradient Modulation Transfer Functions (GMTF) for the (A) x-, (B) y- and (C) z-axis for 0.75T (orange) and 3T (grey) configurations. Resonances are found to be reduced for the 0.75T configuration. Dashed lines correspond to mechanical resonances in Figure 6.2. For the z-axis zeroth-order component also the slope is reduced.

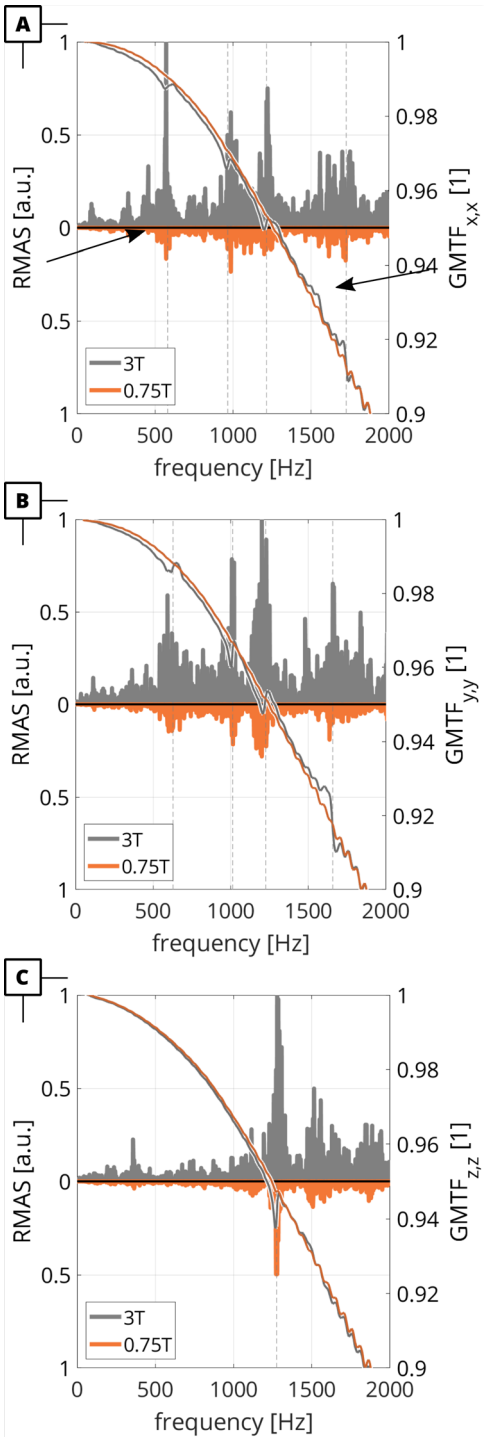

Figure 6.4: Comparison of relative microphone amplitude spectra (RMAS) for the chirp sequence at 0.75T and 3T for (A) x-, (B) y- and (C) z-axis, respectively. For each gradient axis, RMAS were normalized to the maximum value at 3T. Peaks in the RMAS correspond to the mechanical resonances identified in the GMTF. RMAS are reduced for 0.75T by up to 87% depending on the gradient axis when compared to 3T. Dashed lines correspond to mechanical resonances in Figure 6.2.

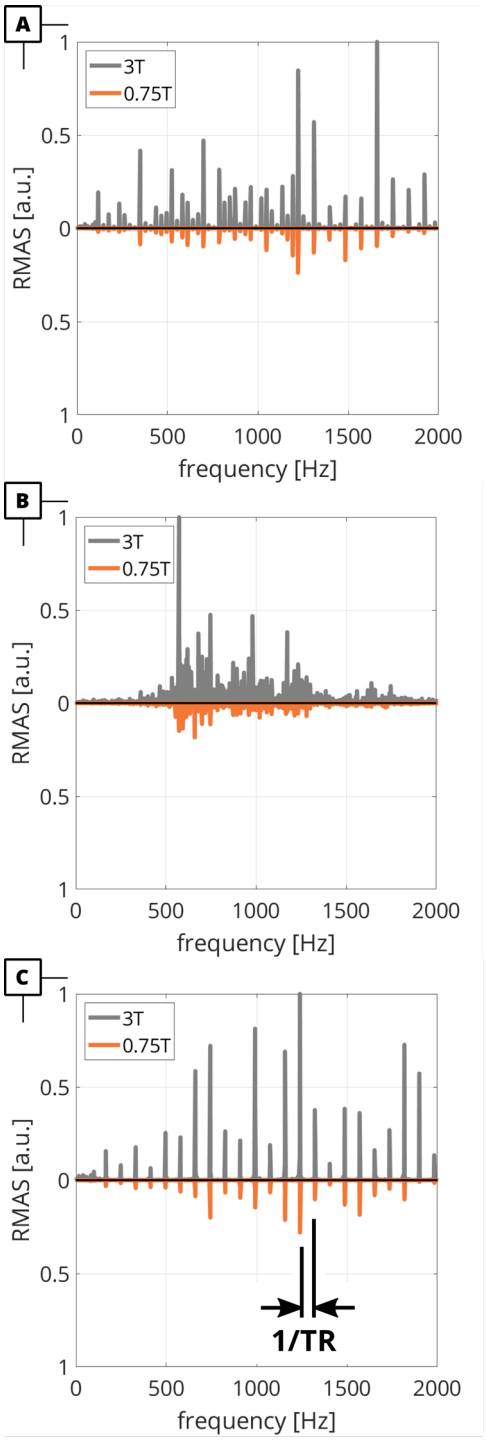

Figure 6.5: Comparison of relative microphone amplitude spectra (RMAS) for 0.75T three-point Dixon sequences played out at 0.75T (orange) and 3T (grey) configurations. (A) Dixon Multi AQ, TR=11.5ms; (B) Spiral Dixon Multi-AQ, TR=50ms; (C) Dixon Multi-Echo TR=12.1ms. Due to the repetitive nature of the MR sequences, RMAS is inherently multiplied with a frequency comb given by 1/TR of the sequence (black arrows, comb frequency 1/TR for ME and 1/(3TR) for Multi AQ). RMAS were normalized to the RMAS at 3T for each sequence type. The RMAS area in the shown frequency range is reduced by a factor (A) 4.1, (B) 3.8, and (C) 5.8.

6.4 Discussion

In this work, GMTFs and RMA spectra of a 3T MRI in its product and down-ramped 0.75T configuration have been presented. While the general transfer characteristics remained similar, mechanical resonances in the GMTF were found to be reduced by up to 92% for the x-axis, 95% for the y-axis and 87% for the z-axis at 0.75T leading to higher gradient fidelity and lower acoustic noise levels. The latter was confirmed by acoustic measurements. For both chirp and Dixon sequences, the 0.75T configuration exhibited significantly decreased sound levels.

Closer inspection of the low-pass behavior of the GMTFs between field-strengths shows a slight increase in fidelity for the lower-field configuration. While hardware components remained unchanged during the ramp-down, passive shims had to be optimized to increase static field homogeneity to an acceptable level. This altered the eddy currents in the conducting materials, which was not accounted for by updated eddy current compensation parameters. Hence, a change in the general transfer characteristics can be expected.

Here, we reported RMAS and first-order GMTFs of the same MR system, which allows to correlate gradient characteristics and acoustic noise emission. Thereby, a direct correspondence of peaks in the RMAS and resonances and antiresonances in the first-order GMTFs for both configurations has been observed. This is in line with simulations by Shao et al.[233] demonstrating that peaks in SPL spectra correspond to mechanical resonances of the gradient coils. With this knowledge, RMAS can be used as a qualitative substitute for GMTFs in sequence design allowing to optimize gradient shapes[217] or pulse trains[222] to reduce acoustic noise exposure of the patient.

Given the possibility of reverse coupling from mechanics to electromagnetics[54] and resulting adverse effects on e.g. sidebands in spectroscopy[234] or field drifts in EPI sequences[222], reducing mechanical resonances by reduction of the field strength may lead to an increase in imaging fidelity. As shown in the current manuscript, mechanical resonances were reduced by up to 92% by a 4-fold reduction in field strength. This not only benefits patient comfort by reducing SPL but may render no-fly zones for oscillating readouts such as EPI superfluous.

In the case of zeroth-order GMTF, the general frequency behavior remained similar after the ramp-down (besides a decreased slope on the z-axis), while variation in the vicinity of mechanical resonances were found to be reduced for the lower-field configuration. For the most prominent mechanical resonance on the x-axis, a reduction of 94% was measured. Online supporting Information Figure S8 presents first-order GMTF cross terms, where cross-talk between gradient axes has been reduced for most axes at 0.75T. Vannesjoe et al.[53] used a dynamic field camera measurement on the same 3T scanner and inferred that asymmetries (GMTFy,z vs. GMTFz,y) in cross-terms between axes may be related to the shared structure embedding the different axes. For the 0.75T configuration, we can confirm that cross-terms for e.g. the z-axis resonance at 1275Hz (GMTFz,y) are reduced. Due to the inherent low-SNR regime of current lower-field systems, further interpretation of cross-terms, however, remains vague and will not be continued here.

Moelker et al. presented a logarithmic dependence of SPL on the main magnetic field strength[213] for most of the investigated sequences. In the current work, 3T / 0.75T = 4, which should result in a decrease of SPL by around 4 (= 12dB)[213] when comparing acoustic noise between down-ramped and product configuration. Here, we report RMAS ratios for the Dixon-type sequences in the range of 3.80 and 5.78, which is in the same ball-park. In addition to the reported SPL reduction, additional sequence timing differences between lower-field and product configuration can play a significant role in the reduction of SPL from standard to lower-field configuration. Guenthner et al. report up to 6-fold reduced microphone amplitudes for three-point Dixon Water/Fat separation sequences at 0.75T versus 3T[235].

This work is limited in terms of its simplified audio recording setup. We used a single microphone that was positioned in the waveguide connecting console and scanner room. This provides only a far-field measurement of the acoustic scanner noise. However, for analyzing patient comfort, SPL inside the bore is required. While far-field SPL and in-bore SPL can be correlated according to Hamaguchi et al.[220], room acoustics modify the RMA spectrum. However, given that for both configurations the scanner and room architecture, microphone position, and its recording amplitude remained the same, our qualitative comparison between field strengths remains valid and equivalent scaling can be expected for in-bore SPL. GMTF acquisition and RMAS recording was performed in separate scan sessions (N.B.: same ramp-down for 0.75T). However, due to its long-term stability[55], the GMTF is not expected to change. Correspondence between GMTF resonance peaks and RMAS peaks support the consistency of the GMTF between scan sessions.

Also, for acquisition of the GMTF, only one type of input sequence (chirp) was used. Previous works have demonstrated the limitations of the LTI assumption depending on the input waveform and temperature of the gradient coils[43] and proposed approaches to reinstate it[54]. Here, ripples in the first-order GMTF above 1 kHz can be observed, which may be indicative of gradient amplifier non-linearities. Despite using the same MRI system (including gradient amplifiers) and using the same test waveforms for lower-field and product configuration GMTF acquisition, differences in the ripple amplitude between configurations can be observed. With the presented GMTF data alone, conclusions on where the differences in non-linearities arises from cannot be drawn, which will need to be subject of future research.

6.5 Conclusion

Lower static fields lead to reduced Lorentz forces on the gradient coil and, in turn, to reduced mechanical resonances, thereby improving gradient fidelity. Simultaneously, the reduction of acoustic noise may help to improve patient comfort.

Discussion & Outlook

In the work at hand, velocity and spatial encoding characteristics of PC-MRI have been critically evaluated by means of simulations and experiments. In theory, very compact sequence designs with shortest echo time are required to reduce spatial and velocity misregistration in particular in high flow regimes[69]. Otherwise significant artefacts result, which have been subject to previous studies on e.g. EPI[72,91–94,96,236–238]. Recent work has evaluated EPI experimentally for high flow in aortae[17]. The authors employed subjective image quality metrics and concluded that EPI is suitable for 4D Flow MRI. Our findings, however, revealed the velocity dependency of the point spread function of EPI in high flow regimes resulting in a velocity-dependent loss of spatial resolution. Our insights also explain results of a subsequent study by Viola et al.[102] who found an underestimation of left ventricle outflow when using EPI for flow measurements across cardiac valves and in the aorta. Westenberg et al.[239] have also confirmed the dependence of velocity errors with EPI, depending on the orientation of the main flow direction relative to spatial encoding gradients in EPI. As EPI poses several challenges in relation to even/odd echo rephasing[70] and ghosting[240–249], for example, alternative methods for shortening scan durations are preferred. To this end, acceleration methods including parallel imaging[250,251] or approaches exploiting spatiotemporal correlations and sparisty[252–254] are suitable options. Compressed sensing[15] and related methods have therefore become indispensable for 4D Flow MRI. Future research might be directed towards comprehensive simulation of the full encoding and reconstruction process for 4D Flow MRI including the optimization of undersampling patterns.

The encoding process of random motion and its application to turbulent flows has been derived and generalized for Gaussian random motion processes with timescales comparable to the duration of velocity encoding gradients. Our simulation results revealed systematic underestimation of turbulence parameters with current models[11]. However, as the simulation was inherently limited by the chosen random motion model and not aimed at reproducing the whole imaging process, experimental verification is needed. The proposed method to probe the Lagrangian motion spectrum may be used to evaluate and tune experimental parameters. However, currently available clinical MR systems lack the necessary gradient system performance. Therefore, pre-clinical or high-performance gradients[255] may be used meanwhile. To reduce underestimation of turbulence parameters in 4D Flow MRI, a correction method has been proposed, which does not include probing of the full motion spectrum, rendering the correction applicable on clinical MRI systems. Accordingly, application of the correction methods to multi-v_{enc} data can reduce inconsistencies in turbulence parameter estimation[157].

Our evaluation of the MRI gradient system based on its GMTF allowed a thorough analysis of mechanical characteristics of the gradient system and their influence on spatial and velocity encoding. The description of the gradient system as a stiff, oscillating mechanical system allowed for the optimization of EPI readouts as well as echo and repetition times in PC-MRI. Work on EPI in particular confirmed the existence of a beat phenomenon with implications for current EPI phase correction approaches[256], which do

not account for time-varying beat phenomena. Future work may focus on the implementation of a robust, time-varying oscillation-aware phase correction method.

Optimization of PC-MRI through minimization of the deflection amplitude at the echo time and mitigation of resonance phenomena by adjusting the repetition time yielded reduced background phases thereby alleviating requirements of retrospective phase correction methods[103]. Accordingly, a reduction of the order of background phase by taking into account insight about mechanical resonances may result in more robust background phase correction in practice.

The field of imaging at lower-field systems has received renewed interest. In the current work, by ramping down a 3T system to 0.75T, undesired characteristics of the gradient system such as deflections due to mechanical resonances were found to be reduced at lower field strength and correlated with sound pressure measurements. Beyond these encouraging findings, lower fields may also offer the possibility to bring additional electronics such as appliances for active noise cancellation or motion detection into the bore, thereby potentially improving patient comfort and the robustness of imaging. Along with the reduced cost of purchase and operation of lower-field systems, a fresh impetus to the wider dissemination of PC-MRI also as part of digital twinning[257] can be expected.

References

1. Lauterbur PC. Image formation by induced local interactions: examples employing nuclear magnetic resonance. *Nature*. 1973;242(5394):190-191.
2. Stankovic Z, Allen BD, Garcia J, Jarvis KB, Markl M. 4D flow imaging with MRI. *Cardiovasc Diagn Ther*. 2014;4(2):173-192. doi:10.3978/j.issn.2223-3652.2014.01.02
3. Sigovan M, Hope MD, Dyverfeldt P, Saloner D. Comparison of four-dimensional flow parameters for quantification of flow eccentricity in the ascending aorta. *J Magn Reson Imaging*. 2011;34(5):1226-1230. doi:10.1002/jmri.22800
4. Rodríguez-Palomares JF, Dux-Santoy L, Guala A, et al. Aortic flow patterns and wall shear stress maps by 4D-flow MRI in the assessment of aortic dilatation in bicuspid aortic valve. *Jcmr*. 2018:1-15. doi:10.1186/s12968-018-0451-1
5. Guzzardi DG, Barker AJ, Van Ooij P, et al. Valve-Related Hemodynamics Mediate Human Bicuspid Aortopathy: Insights From Wall Shear Stress Mapping. *J Am Coll Cardiol*. 2015;66(8):892-900. doi:10.1016/j.jacc.2015.06.1310
6. Markl M, Wallis W, Brendecke S, Simon J, Frydrychowicz A, Harloff A. Estimation of global aortic pulse wave velocity by flow-sensitive 4D MRI. *Magn Reson Med*. 2010;63(6):1575-1582. doi:10.1002/mrm.22353
7. Rengier F, Delles M, Eichhorn J, et al. Noninvasive 4D pressure difference mapping derived from 4D flow MRI in patients with repaired aortic coarctation: comparison with young healthy volunteers. *Int J Cardiovasc Imaging*. 2015;31(4):823-830. doi:10.1007/s10554-015-0604-3
8. Sierra-Galan LM, François CJ. Clinical Applications of MRA 4D-Flow. *Curr Treat Options Cardiovasc Med*. 2019;21(10). doi:10.1007/s11936-019-0758-8
9. Crandon S, Elbaz MSM, Westenberg JJM, van der Geest RJ, Plein S, Garg P. Clinical applications of intra-cardiac four-dimensional flow cardiovascular magnetic resonance: A systematic review. *Int J Cardiol*. 2017;249:486-493. doi:10.1016/j.ijcard.2017.07.023
10. Hope MD, Meadows AK, Hope TA, et al. Clinical evaluation of aortic coarctation with 4D flow MR imaging. *J Magn Reson Imaging*. 2010;31(3):711-718. doi:10.1002/jmri.22083
11. Dyverfeldt P, Gårdhagen R, Sigfridsson A, Karlsson M, Ebbers T. On MRI turbulence quantification. *Magn Reson Imaging*. 2009;27(7):913-922. doi:10.1016/j.mri.2009.05.004
12. Binter C, Gotschy A, Sündermann SH, et al. Turbulent Kinetic Energy Assessed by Multipoint 4-Dimensional Flow Magnetic Resonance Imaging Provides Additional Information Relative to Echocardiography for the Determination of Aortic Stenosis Severity. *Circ Cardiovasc Imaging*. 2017;10(6). doi:10.1161/CIRCIMAGING.116.005486
13. Kwong RY. *Cardiovascular Magnetic Resonance Imaging.*; 2011. doi:10.1016/B978-0-7020-3426-8.00007-1
14. Moschetti K, Muzzarelli S, Pinget C, et al. Cost evaluation of cardiovascular magnetic resonance versus coronary angiography for the diagnostic work-up of coronary artery disease: Application of the European Cardiovascular Magnetic Resonance registry data to the German, United Kingdom, Swiss, and U. *J*

Cardiovasc Magn Reson. 2012;14(1):1-9. doi:10.1186/1532-429X-14-35

15. Donoho DL, Santos JM, Pauly JM. Compressed Sensing MRI. (March 2008):72-82. doi:10.1109/MSP.2007.914728
16. Walheim J, Dillinger H, Gotschy A, Kozerke S. 5D Flow Tensor MRI to Efficiently Map Reynolds Stresses of Aortic Blood Flow In-Vivo. *Sci Rep*. 2019;9(1):1-12. doi:10.1038/s41598-019-55353-x
17. Garg P, Westenberg JJM, van den Boogaard PJ, et al. Comparison of fast acquisition strategies in whole-heart four-dimensional flow cardiac MR: Two-center, 1.5 Tesla, phantom and in vivo validation study. *J Magn Reson Imaging*. 2018;47(1):272-281. doi:10.1002/jmri.25746
18. Baumgartner H, Falk V, Bax JJ, et al. 2017 ESC/EACTS Guidelines for the management of valvular heart disease. *Eur Heart J*. 2017;38(36):2739-2791. doi:10.1093/eurheartj/ehx391
19. Akins CW, Travis B, Yoganathan AP. Energy loss for evaluating heart valve performance. *J Thorac Cardiovasc Surg*. 2008;136(4):820-833. doi:10.1016/j.jtcvs.2007.12.059
20. Levine RA, Jimoh A, Cape EG, McMillan S, Yoganathan AP, Weyman AE. Pressure recovery distal to a stenosis: Potential cause of gradient "verestimation" by Doppler echocardiography. *J Am Coll Cardiol*. 1989;13(3):706-715. doi:10.1016/0735-1097(89)90615-3
21. Rijsterborgh H, Roelandt J. Doppler assessment of aortic stenosis: Bernoulli revisited. *Ultrasound Med Biol*. 1987;13(5):241-248.
22. Garcia D, Pibarot P, Dumesnil JG, Sakr F, Durand LG. Assessment of aortic valve stenosis severity: A new index based on the energy loss concept. *Circulation*. 2000;101(7):765-771. doi:10.1161/01.CIR.101.7.765
23. Garcia D, Dumesnil JG, Durand LG, Kadem L, Pibarot P. Discrepancies between catheter and doppler estimates of valve effective orifice area can be predicted from the pressure recovery phenomenon: Practical implications with regard to quantification of aortic stenosis severity. *J Am Coll Cardiol*. 2003;41(3):435-442. doi:10.1016/S0735-1097(02)02764-X
24. Coats AJS. Doppler ultrasonic measurement of cardiac output: Reproducibility and validation. *Eur Heart J*. 1990;11(SUPPL. I):49-61. doi:10.1093/eurheartj/11.suppl_i.49
25. Hachicha Z, Dumesnil JG, Bogaty P, Pibarot P. Paradoxical low-flow, low-gradient severe aortic stenosis despite preserved ejection fraction is associated with higher afterload and reduced survival. *Circulation*. 2007;115(22):2856-2864. doi:10.1161/CIRCULATIONAHA.106.668681
26. Markl M, Wallis W, Harloff A. Reproducibility of flow and wall shear stress analysis using flow-sensitive four-dimensional MRI. *J Magn Reson Imaging*. 2011;33(4):988-994. doi:10.1002/jmri.22519
27. Dyverfeldt P, Bissell M, Barker AJ, et al. 4D flow cardiovascular magnetic resonance consensus statement. *J Cardiovasc Magn Reson*. 2015;17(1):1-19. doi:10.1186/s12968-015-0174-5
28. Inati SJ, Naegele JD, Zwart NR, et al. ISMRM Raw data format: A proposed standard for MRI raw datasets. *Magn Reson Med*. 2017;77(1):411-421.

doi:10.1002/mrm.26089

29. Gatehouse PD, Rolf MP, Bloch KM, et al. A multi-center inter-manufacturer study of the temporal stability of phase-contrast velocity mapping background offset errors. *J Cardiovasc Magn Reson*. 2012;14(1):1-7. doi:10.1186/1532-429X-14-72
30. Kan HE, Heunis S, Taylor S, Wagner A, White T. ESMRMB annual meeting roundtable discussion: "Challenges and solutions in data sharing—an MRI perspective." *Magn Reson Mater Physics, Biol Med*. 2021;34(4):483-486. doi:10.1007/s10334-021-00942-z
31. SR 810.30 - Bundesgesetz vom 30. September 2011 über die Forschung am Menschen (Humanforschungsgesetz, HFG). https://www.fedlex.admin.ch/eli/cc/2013/617/de#art_16. Accessed January 17, 2022.
32. Bloch F. Nuclear induction. *Phys Rev*. 1946;70(7-8):460-474. doi:10.1103/PhysRev.70.460
33. Kumar A, Welti D, Ernst RR. NMR Fourier zeugmatography. *J Magn Reson*. 1975;18(1):69-83. doi:10.1016/0022-2364(75)90224-3
34. Guerquin-Kern M, Lejeune L, Pruessmann KP, Unser M. Realistic analytical phantoms for parallel magnetic resonance imaging. *IEEE Trans Med Imaging*. 2012;31(3):626-636. doi:10.1109/TMI.2011.2174158
35. Cheng GK, Sarlls JE, Özarslan E. Three-dimensional analytical magnetic resonance imaging phantom in the Fourier domain. *Magn Reson Med*. 2007;58(2):430-436. doi:10.1002/mrm.21292
36. Petersson S, Dyverfeldt P, Gårdhagen R, Karlsson M, Ebbers T. Simulation of phase contrast MRI of turbulent flow. *Magn Reson Med*. 2010;64(4):1039-1046. doi:10.1002/mrm.22494
37. Jurczuk K, Kretowski M, Bellanger JJ, Eliat PA, Saint-Jalmes H, Bézy-Wendling J. Computational modeling of MR flow imaging by the lattice Boltzmann method and Bloch equation. *Magn Reson Imaging*. 2013;31(7):1163-1173. doi:10.1016/j.mri.2013.01.005
38. Mirzaee H, Henn T, Krause MJ, et al. MRI-based computational hemodynamics in patients with aortic coarctation using the lattice Boltzmann methods: Clinical validation study. *J Magn Reson Imaging*. 2017;45(1):139-146. doi:10.1002/jmri.25366
39. Dillinger H, Walheim J, Kozerke S. On the limitations of echo planar 4D flow MRI. *Magn Reson Med*. 2020;84(4):1806-1816. doi:10.1002/mrm.28236
40. Dillinger H, McGrath C, Guenthner C, Kozerke S. Fundamentals of turbulent flow spectrum imaging. *Magn Reson Med*. 2022;87(3):1231-1249. doi:10.1002/mrm.29001
41. Rose JN, Nielles-Vallespin S, Ferreira PF, Firmin DN, Scott AD, Doorly DJ. Novel insights into in-vivo diffusion tensor cardiovascular magnetic resonance using computational modeling and a histology-based virtual microstructure. *Magn Reson Med*. 2019;81(4):2759-2773. doi:10.1002/mrm.27561
42. Brunner DO, Dietrich BE, Çavuşoğlu M, et al. Concurrent recording of RF pulses and gradient fields – comprehensive field monitoring for MRI. *NMR Biomed*. 2016;29(9):1162-1172. doi:10.1002/nbm.3359

43. Nussbaum J, Rösler MB, Dietrich BE, Pruessmann KP. Nonlinearity and thermal effects in gradient chains: a cascade analysis based on current and field sensing. In: *Proc. Intl. Soc. Mag. Reson. Med.* Vol 27. ; 2019:213.
44. Winkler SA, Schmitt F, Landes H, et al. Gradient and shim technologies for ultra high field MRI. *Neuroimage*. 2018;168(November 2016):59-70. doi:10.1016/j.neuroimage.2016.11.033
45. Gatehouse P, Rolf M, Graves M, et al. Flow measurement by cardiovascular magnetic resonance: A multi-centre multi-vendor study of background phase offset errors that can compromise the accuracy of derived regurgitant or shunt flow measurements. *J Cardiovasc Magn Reson*. 2010;12(1):1-8. doi:10.1186/1532-429X-12-5
46. Evensen G. The Ensemble Kalman Filter: Theoretical formulation and practical implementation. *Ocean Dyn*. 2003;53(4):343-367. doi:10.1007/s10236-003-0036-9
47. Iglesias MA, Law KJH, Stuart AM. Ensemble kalman methods for inverse problems. *Inverse Probl*. 2013;29(4). doi:10.1088/0266-5611/29/4/045001
48. De Marinis D, Obrist D. Data Assimilation by Stochastic Ensemble Kalman Filtering to Enhance Turbulent Cardiovascular Flow Data From Under-Resolved Observations. *Front Cardiovasc Med*. 2021;8:1486. doi:10.3389/fcvm.2021.742110
49. Fischer RF, Barmet C, Rudin M, Boesiger P, Pruessmann KP, Kozerke S. Monitoring and compensating phase imperfections in cine balanced steady-state free precession. *Magn Reson Med*. 2013;70(6):1567-1579. doi:10.1002/mrm.24606
50. Bruijnen T, Stemkens B, van den Berg CAT, Tijssen RHN. Prospective GIRF-based RF phase cycling to reduce eddy current-induced steady-state disruption in bSSFP imaging. *Magn Reson Med*. 2020;84(1):115-127. doi:10.1002/mrm.28097
51. Middione MJ, Wu HH, Ennis DB. Convex gradient optimization for increased spatiotemporal resolution and improved accuracy in phase contrast MRI. *Magn Reson Med*. 2014;72(6):1552-1564. doi:10.1002/mrm.25059
52. Giese D, Haeberlin M, Barmet C, Pruessmann KP, Schaeffter T, Kozerke S. Analysis and correction of background velocity offsets in phase-contrast flow measurements using magnetic field monitoring. *Magn Reson Med*. 2012;67(5):1294-1302. doi:10.1002/mrm.23111
53. Vannesjo SJ, Haeberlin M, Kasper L, et al. Gradient system characterization by impulse response measurements with a dynamic field camera. *Magn Reson Med*. 2013;69(2):583-593. doi:10.1002/mrm.24263
54. Nussbaum J, Dietrich BE, Wilm BJ, Pruessmann KP. Thermal variation in gradient response: measurement and modeling. *Magn Reson Med*. 2021;(July):1-15. doi:10.1002/mrm.29123
55. Vannesjo SJ, Graedel NN, Kasper L, et al. Image reconstruction using a gradient impulse response model for trajectory prediction. *Magn Reson Med*. 2016;76(1):45-58. doi:10.1002/mrm.25841
56. Conant RC, Ross Ashby W. Every good regulator of a system must be a model of that system. *Int J Syst Sci*. 1970;1(2):89-97. doi:10.1080/00207727008920220
57. Haase A, Frahm J, Matthaei D, Hanicke W, Merboldt K-D. FLASH imaging. Rapid NMR imaging using low flip-angle pulses. *J Magn Reson*. 1986;67(2):258-266. doi:10.1016/0022-2364(86)90433-6

58. Hargreaves B. Rapid gradient-echo imaging. *J Magn Reson Imaging*. 2012;36(6):1300-1313. doi:10.1002/jmri.23742
59. Stehling MK, Turner R, Mansfield P. Echo-Planar Imaging: Magnetic Resonance Imaging in a Fraction of a Second. *Science (80-)*. 1991;254(5028):43-50. doi:10.1126/science.1925560
60. Barger A V., Block WF, Toropov Y, Grist TM, Mistretta CA. Time-resolved contrast-enhanced imaging with isotropic resolution and broad coverage using an undersampled 3D projection trajectory. *Magn Reson Med*. 2002;48(2):297-305. doi:10.1002/mrm.10212
61. Sigfridsson A, Petersson S, Carlhäll CJ, Ebbers T. Four-dimensional flow MRI using spiral acquisition. *Magn Reson Med*. 2012;68(4):1065-1073. doi:10.1002/mrm.23297
62. Kadbi M, Negahdar MJ, Cha JW, et al. 4D UTE flow: A phase-contrast MRI technique for assessment and visualization of stenotic flows. *Magn Reson Med*. 2015;73(3):939-950. doi:10.1002/mrm.25188
63. Webb AG. *Magnetic Resonance Technology*. The Royal Society of Chemistry; 2016. doi:10.1039/9781782623878
64. Bernstein MA, Shimakawa A, Pelc NJ. Minimizing TE in moment-nulled or flow-encoded two-and three-dimensional gradient-echo imaging. *J Magn Reson Imaging*. 1992;2(5):583-588. doi:10.1002/jmri.1880020517
65. Chai P, Mohiaddin R. How we perform cardiovascular magnetic resonance flow assessment using phase-contrast velocity mapping. *J Cardiovasc Magn Reson*. 2005;7(4):705-716. doi:10.1081/JCMR-200065639
66. Moran PR. A flow velocity zeugmatographic interlace for NMR imaging in humans. *Magn Reson Imaging*. 1982;1(4):197-203. doi:10.1016/0730-725X(82)90170-9
67. Walheim J, Dillinger H, Kozerke S. Multipoint 5D Flow Cardiovascular Magnetic Resonance - Accelerated Cardiac- and Respiratory-Motion Resolved Mapping of Mean and Turbulent Velocities. *J Cardiovasc Magn Reson*. 2019. doi:10.1186/s12968-019-0549-0
68. Haacke EM, Lenz GW. Improving MR image quality in the presence of motion by using rephasing gradients. *Am J Roentgenol*. 1987;148(6):1251-1258. doi:10.2214/ajr.148.6.1251
69. O'Brien KR, Gabriel RS, Greiser A, Cowan BR, Young AA, Kerr AJ. Aortic valve stenotic area calculation from phase contrast cardiovascular magnetic resonance: The importance of short echo time. *J Cardiovasc Magn Reson*. 2009;11(1):1-12. doi:10.1186/1532-429X-11-49
70. Katz J, Peshock RM, Malloy CR, Schaefer S, Parkey RW. Even-echo rephasing and constant velocity flow. *Magn Reson Med*. 1987;4(5):422-430. doi:10.1002/mrm.1910040503
71. Butts K, Riederer SJ. Analysis of flow effects in echo-planar imaging. *J Magn Reson Imaging*. 1992;2(3):285-293. http://www.ncbi.nlm.nih.gov/pubmed/1627863.
72. Nishimura DG, Irarrazabal P, Meyer CH. Velocity k-Space Analysis of Flow Effects in Echo- Planar and Spiral Imaging. *Magn Reson Med*. 1995;33:549-556. papers3://publication/uuid/8FC9F293-EA91-45A0-8F26-828171C6C528.

73. Markl M, Schnell S, Wu C, et al. Advanced flow MRI: emerging techniques and applications. *Clin Radiol*. 2016;71(8):779-795. doi:10.1016/j.crad.2016.01.011
74. Ha H, Kvitting J-PE, Dyverfeldt P, Ebbers T. 4D Flow MRI quantification of blood flow patterns, turbulence and pressure drop in normal and stenotic prosthetic heart valves. *Magn Reson Imaging*. 2019;55:118-127. doi:10.1016/j.mri.2018.09.024
75. Ziegler M, Lantz J, Ebbers T, Dyverfeldt P. Assessment of turbulent flow effects on the vessel wall using four-dimensional flow MRI. *Magn Reson Med*. 2017;77(6):2310-2319. doi:10.1002/mrm.26308
76. Haraldsson H, Kefayati S, Ahn S, et al. Assessment of Reynolds stress components and turbulent pressure loss using 4D flow MRI with extended motion encoding. *Magn Reson Med*. 2018;79(4):1962-1971. doi:10.1002/mrm.26853
77. Casas B, Lantz J, DyverfeldT P, Ebbers T. 4D Flow MRI-based pressure loss estimation in stenotic flows: Evaluation using numerical simulations. *Magn Reson Med*. 2016;75(4):1808-1821. doi:10.1002/mrm.25772
78. Markl M, Frydrychowicz A, Kozerke S, Hope M, Wieben O. 4D flow MRI. *J Magn Reson Imaging*. 2012;36(5):1015-1036. doi:10.1002/jmri.23632
79. Ma LE, Markl M, Chow K, et al. Aortic 4D flow MRI in 2 minutes using compressed sensing, respiratory controlled adaptive k-space reordering, and inline reconstruction. *Magn Reson Med*. 2019;(October 2018):1-16. doi:10.1002/mrm.27684
80. Valvano G, Martini N, Huber A, et al. Accelerating 4D flow MRI by exploiting low-rank matrix structure and hadamard sparsity. *Magn Reson Med*. 2016;00(June):1-12. doi:10.1002/mrm.26508
81. Driessen MMP, Schings MA, Sieswerda GT, et al. Tricuspid flow and regurgitation in congenital heart disease and pulmonary hypertension: Comparison of 4D flow cardiovascular magnetic resonance and echocardiography. *J Cardiovasc Magn Reson*. 2018;20(1):1-10. doi:10.1186/s12968-017-0426-7
82. Marsan NA, Westenberg JJM, Ypenburg C, et al. Quantification of Functional Mitral Regurgitation by Real-Time 3D Echocardiography. Comparison With 3D Velocity-Encoded Cardiac Magnetic Resonance. *JACC Cardiovasc Imaging*. 2009;2(11):1245-1252. doi:10.1016/j.jcmg.2009.07.006
83. Elbaz MSM, van der Geest RJ, Calkoen EE, et al. Assessment of viscous energy loss and the association with three-dimensional vortex ring formation in left ventricular inflow: In vivo evaluation using four-dimensional flow MRI. *Magn Reson Med*. 2017;77(2):794-805. doi:10.1002/mrm.26129
84. She HL, Roest AAW, Calkoen EE, et al. Comparative Evaluation of Flow Quantification across the Atrioventricular Valve in Patients with Functional Univentricular Heart after Fontan's Surgery and Healthy Controls: Measurement by 4D Flow Magnetic Resonance Imaging and Streamline Visualization. *Congenit Heart Dis*. 2017;12(1):40-48. doi:10.1111/chd.12397
85. Calkoen EE, Westenberg JJM, Kroft LJM, et al. Characterization and quantification of dynamic eccentric regurgitation of the left atrioventricular valve after atrioventricular septal defect correction with 4D Flow cardiovascular magnetic resonance and retrospective valve tracking. *J Cardiovasc Magn Reson*. 2015;17(1):1-9. doi:10.1186/s12968-015-0122-4

86. Elbaz MSM, Calkoen EE, Westenberg JJM, Lelieveldt BPF, Roest AAW, Van Der Geest RJ. Vortex flow during early and late left ventricular filling in normal subjects: Quantitative characterization using retrospectively-gated 4D flow cardiovascular magnetic resonance and three-dimensional vortex core analysis. *J Cardiovasc Magn Reson*. 2014;16(1):1-12. doi:10.1186/s12968-014-0078-9
87. Ewe SH, Delgado V, Van Der Geest R, et al. Accuracy of three-dimensional versus two-dimensional echocardiography for quantification of aortic regurgitation and validation by three-dimensional three-directional velocity-encoded magnetic resonance imaging. *Am J Cardiol*. 2013;112(4):560-566. doi:10.1016/j.amjcard.2013.04.025
88. Kröner ESJ, Van Der Geest RJ, Scholte AJHA, et al. Evaluation of sampling density on the accuracy of aortic pulse wave velocity from velocity-encoded MRI in patients with Marfan syndrome. *J Magn Reson Imaging*. 2012;36(6):1470-1476. doi:10.1002/jmri.23729
89. Brandts A, Bertini M, Van Dijk EJ, et al. Left ventricular diastolic function assessment from three-dimensional three-directional velocity-encoded MRI with retrospective valve tracking. *J Magn Reson Imaging*. 2011;33(2):312-319. doi:10.1002/jmri.22424
90. Marsan NA, Westenberg JJM, Roes SD, et al. Three-dimensional echocardiography for the preoperative assessment of patients with left ventricular aneurysm. *Ann Thorac Surg*. 2011;91(1):113-121. doi:10.1016/j.athoracsur.2010.08.048
91. Steinman DA, Ethier CR, Rutt BK. Combined analysis of spatial and velocity displacement artifacts in phase contrast measurements of complex flows. *J Magn Reson Imaging*. 1997;7(2):339-346. doi:10.1002/jmri.1880070214
92. Wedeen VJ, Wendt RE, Jerosch-Herold M. Motional phase artifacts in fourier transform MRI. *Magn Reson Med*. 1989;11(1):114-120. doi:10.1002/mrm.1910110110
93. Nishimura DG, Jackson JI, Pauly JM. On the nature and reduction of the displacement artifact in flow images. *Magn Reson Med*. 1991;22(2):481-492. doi:10.1002/mrm.1910220255
94. Duerk JL, Simonetti OP. Theoretical aspects of motion sensitivity and compensation in echo-planar imaging. *J Magn Reson Imaging*. 1991;1(6):643-650. doi:10.1002/jmri.1880010605
95. Tkach JA, Ding X, Ruggieri PM, Obuchowski NA, Lieber M, Masaryk TJ. Segmented three-dimensional echo-planar flow imaging of the cervical carotid arteries. *Am J Neuroradiol*. 1997;18(7):1339-1347.
96. O'Brien KR, Cowan BR, Jain M, Stewart RAH, Kerr AJ, Young AA. MRI phase contrast velocity and flow errors in turbulent stenotic jets. *J Magn Reson Imaging*. 2008;28(1):210-218. doi:10.1002/jmri.21395
97. Dyverfeldt P, Sigfridsson A, Kvitting JPE, Ebbers T. Quantification of intravoxel velocity standard deviation and turbulence intensity by generalizing phase-contrast MRI. *Magn Reson Med*. 2006;56(4):850-858. doi:10.1002/mrm.21022
98. R Sibson. A brief description of natural neighbor interpolation. In: *Interpreting Multivariate Data*. John Wiley & Sons; 1981:21–36. http://ci.nii.ac.jp/naid/10022185042/en/. Accessed June 24, 2019.

99. Herráez MA, Burton DR, Lalor MJ, Gdeisat MA. Fast two-dimensional phase-unwrapping algorithm based on sorting by reliability following a noncontinuous path. *Appl Opt*. 2002;41(35):7437. doi:10.1364/ao.41.007437
100. Binter C, Knobloch V, Manka R, Sigfridsson A, Kozerke S. Bayesian multipoint velocity encoding for concurrent flow and turbulence mapping. *Magn Reson Med*. 2013;69(5):1337-1345. doi:10.1002/mrm.24370
101. Baumgartner H, Falk V, Bax JJ, et al. 2017 ESC/EACTS Guidelines for the management of valvular heart disease. *Eur Heart J*. 2017;38(36):2739-2786. doi:10.1093/eurheartj/ehx391
102. Viola F, Dyverfeldt P, Carlhäll CJ, Ebbers T. Data Quality and Optimal Background Correction Order of Respiratory-Gated k-Space Segmented Spoiled Gradient Echo (SGRE) and Echo Planar Imaging (EPI)-Based 4D Flow MRI. *J Magn Reson Imaging*. 2019:1-12. doi:10.1002/jmri.26879
103. Busch J, Giese D, Kozerke S. Image-based background phase error correction in 4D flow MRI revisited. *J Magn Reson Imaging*. 2017;46(5):1516-1525. doi:10.1002/jmri.25668
104. Axel L. Blood Flow Effects Magnetic Resonance Imaging. *Am Roentgen Ray Soc*. 1984;143(84):1436-1157. doi:10.1017/CBO9781107415324.004
105. Peters DC, Korosec FR, Grist TM, et al. Undersampled projection reconstruction applied to MR angiography. *Magn Reson Med*. 2000;43(1):91-101. doi:10.1002/(SICI)1522-2594(200001)43:1<91::AID-MRM11>3.0.CO;2-4
106. Callaghan PT. *Principles of Nuclear Magnetic Resonance Microscopy*. Oxford : Clarendon Press; 1991.
107. Dillinger H, McGrath C, Guenthner C, Kozerke S. Fundamentals of turbulent flow spectrum imaging. *Magn Reson Med*. 2021;(August):223-249. doi:10.1002/mrm.29001
108. Tuch DS. Q-ball imaging. *Magn Reson Med*. 2004;52(6):1358-1372. doi:10.1002/mrm.20279
109. Stejskal EO. Use of Spin Echoes in a Pulsed Magnetic-Field Gradient to Study Anisotropic, Restricted Diffusion and Flow. *J Chem Phys*. 1965;43(10):3597-3603. doi:10.1063/1.1696526
110. Yablonskiy DA, Sukstanskii AL. Theoretical models of the diffusion weighted MR signal. *NMR Biomed*. 2010;23(7):661-681. doi:10.1002/nbm.1520
111. Callaghan PT, Xia Y. Velocity and diffusion imaging in dynamic NMR microscopy. *J Magn Reson*. 1991;91(2):326-352. doi:10.1016/0022-2364(91)90196-Z
112. Pope SB. *Turbulent Flows*. Cambridge: Cambridge University Press; 2000. doi:10.1017/CBO9780511840531
113. Ha H, Ziegler M, Welander M, et al. Age-related vascular changes affect turbulence in aortic blood flow. *Front Physiol*. 2018;9(JAN):1-10. doi:10.3389/fphys.2018.00036
114. Stein PD, Sabbah HN. Turbulent Blood-Flow in Ascending Aorta of Humans with Normal and Diseased Aortic Valves. *Circ Res*. 1976;39(1):58-65. doi:10.1161/01.RES.39.1.58
115. Galanti B, Tsinober A. Is turbulence ergodic? *Phys Lett Sect A Gen At Solid State Phys*. 2004;330(3-4):173-180. doi:10.1016/j.physleta.2004.07.009

116. Nishimura DG, Irarrazabal P, Meyer CH. A Velocity k space Analysis of Flow Effects in Echo Planar and Spiral Imaging. *Magn Reson Med*. 1995;33(4):549-556. doi:10.1002/mrm.1910330414
117. Kundu PK, Cohen IM, Dowling DR. Turbulence. In: Kundu PK, Cohen IM, Dowling DRBT-FM (Sixth E, eds. *Fluid Mechanics*. Boston: Elsevier; 2016:603-697. doi:10.1016/B978-0-12-405935-1.00012-5
118. Hsiao A, Tariq U, Alley MT, Lustig M, Vasanawala SS. Inlet and outlet valve flow and regurgitant volume may be directly and reliably quantified with accelerated, volumetric phase-contrast MRI. *J Magn Reson Imaging*. 2015;41(2):376-385. doi:10.1002/jmri.24578
119. Mahadevia R, Barker AJ, Schnell S, et al. Bicuspid aortic cusp fusion morphology alters aortic three-dimensional outflow patterns, wall shear stress, and expression of aortopathy. *Circulation*. 2014;129(6):673-682. doi:10.1161/CIRCULATIONAHA.113.003026
120. François CJ, Markl M, Schiebler ML, et al. Four-dimensional, flow-sensitive magnetic resonance imaging of blood flow patterns in thoracic aortic dissections. *J Thorac Cardiovasc Surg*. 2013;145(5):1359-1366. doi:10.1016/j.jtcvs.2012.07.019
121. Chen SSM, Kilner PJ. Unilateral pulmonary artery branch stenosis: Diastolic prolongation of forward flow appears to maintain flow to the affected lung if the pulmonary valve is competent. *Int J Cardiol*. 2013;168(4):3698-3703. doi:10.1016/j.ijcard.2013.06.019
122. Ha H, Kvitting JPE, Dyverfeldt P, Ebbers T. Validation of pressure drop assessment using 4D flow MRI-based turbulence production in various shapes of aortic stenoses. *Magn Reson Med*. 2019;81(2):893-906. doi:10.1002/mrm.27437
123. Kuethe DO, Gao JH. NMR signal loss from turbulence: Models of time dependence compared with data. *Phys Rev E*. 1995;51(4):3252-3262. doi:10.1103/PhysRevE.51.3252
124. Kuethe DO. Measuring distributions of diffusivity in turbulent fluids with magnetic-resonance imaging. *Phys Rev A*. 1989;40(8):4542-4551. doi:10.1103/PhysRevA.40.4542
125. Gao J-H, Gore JC. Turbulent flow effects on NMR imaging: Measurement of turbulent intensity. *Med Phys*. 1991;18(5):1045-1051. doi:10.1118/1.596645
126. Gatenby JC. Mapping of Turbulent Intensity by Magnetic Resonance Imaging.
127. Gatenby JC, Gore JC. Characterization of Turbulent Flows by NMR Measurements with Pulsed Gradients. *J Magn Reson Ser A*. 1994;110(1):26-32. doi:10.1006/jmra.1994.1176
128. Gatenby JC, Gore JC. Echo-planar-imaging studies of turbulent flow. *J Magn Reson - Ser A*. 1996;121(2):193-200. doi:10.1006/jmra.1996.0160
129. Clark C. Turbulent velocity measurements in a model of aortic stenosis. *J Biomech*. 1976;9(11):677-687. doi:10.1016/0021-9290(76)90169-X
130. Clark C. Turbulent wall pressure measurements in a model of aortic stenosis. *J Biomech*. 1977;10(8):461-472. doi:10.1016/0021-9290(77)90100-2
131. Liu JS, Lu PC, Chu SH. Turbulence Characteristics Downstream of Bileaflet Aortic Valve Prostheses. *J Biomech Eng*. 2000;122(2):118-124. doi:10.1115/1.429643
132. Stepišnik J. Analysis of NMR self-diffusion measurements by a density matrix

calculation. *Phys B+C*. 1981;104(3):350-364. doi:10.1016/0378-4363(81)90182-0
133. Stepišnik J. Measuring and imaging of flow by NMR. *Prog Nucl Magn Reson Spectrosc*. 1985;17(C):187-209. doi:10.1016/0079-6565(85)80008-X
134. Callaghan PT, Stepišnik J. Frequency-Domain Analysis of Spin Motion Using Modulated-Gradient NMR. *J Magn Reson Ser A*. 1995;117(1):118-122. doi:10.1006/jmra.1995.9959
135. Newling B, Poirier CC, Zhi Y, et al. Velocity imaging of highly turbulent gas flow. *Phys Rev Lett*. 2004;93(15):1-4. doi:10.1103/PhysRevLett.93.154503
136. Kubo R. Generalized cumulant expansion method. *J Phys Soc Japan*. 1962;17(7):1100-1120. doi:10.1143/JPSJ.17.1100
137. Ning L, Setsompop K, Westin CF, Rathi Y. New insights about time-varying diffusivity and its estimation from diffusion MRI. *Magn Reson Med*. 2017;78(2):763-774. doi:10.1002/mrm.26403
138. Binter C, Gülan U, Holzner M, Kozerke S. On the accuracy of viscous and turbulent loss quantification in stenotic aortic flow using phase-contrast MRI. *Magn Reson Med*. 2016;76(1):191-196. doi:10.1002/mrm.25862
139. Ha H, Lantz J, Haraldsson H, et al. Assessment of turbulent viscous stress using ICOSA 4D Flow MRI for prediction of hemodynamic blood damage. *Sci Rep*. 2016;6(September):1-14. doi:10.1038/srep39773
140. Caprihan A, Seymour JD. Correlation Time and Diffusion Coefficient Imaging: Application to a Granular Flow System. *J Magn Reson*. 2000;144(1):96-107. doi:10.1006/jmre.2000.2033
141. Torrey HC. Bloch equations with diffusion terms. *Phys Rev*. 1956;104(3):563-565. doi:10.1103/PhysRev.104.563
142. Stepišnik J. Time-dependent self-diffusion by NMR spin-echo. *Phys B Phys Condens Matter*. 1993;183(4):343-350. doi:10.1016/0921-4526(93)90124-O
143. Jabir E, Lal SA. Numerical analysis of blood flow through an elliptic stenosis using large eddy simulation. *Proc Inst Mech Eng Part H J Eng Med*. 2016;230(8):709-726. doi:10.1177/0954411916644474
144. Mittal R, Simmons SP, Udaykumar HS. Application of large-eddy simulation to the study of pulsatile flow in a modeled arterial stenosis. *J Biomech Eng*. 2001;123(4):325-332. doi:10.1115/1.1385840
145. Varghese SS, Frankel SH, Fischer PF. Direct numerical simulation of stenotic flows. Part 1. Steady flow. *J Fluid Mech*. 2007;582:253-280. doi:10.1017/S0022112007005848
146. Paul MC, Molla MM. Investigation of physiological pulsatile flow in a model arterial stenosis using large-eddy and direct numerical simulations. *Appl Math Model*. 2012;36(9):4393-4413. doi:10.1016/j.apm.2011.11.065
147. Ahmed SA. An experimental investigation of pulsatile flow through a smooth constriction. *Exp Therm Fluid Sci*. 1998;17(4):309-318. doi:10.1016/S0894-1777(98)00009-0
148. Kim BM, Corcoran WH. Experimental measurements of turbulence spectra distal to stenoses. *J Biomech*. 1974;7(4):335-342. doi:10.1016/0021-9290(74)90028-1
149. Paulsen PK, Nygaard H, Hasenkam JM, Gormsen J, Stødkilde-Jørgensen H, Albrechtsen O. Analysis of Velocity in the Ascending Aorta in Humans. *Int J Artif*

Organs. 1988;11(4):293-302. doi:10.1177/039139888801100413

150. Tobin RJ, Chang ID. Wall pressure spectra scaling downstream of stenoses in steady tube flow. *J Biomech*. 1976;9(10):633-640. doi:10.1016/0021-9290(76)90105-6
151. Mancini V, Bergersen AW, Vierendeels J, Segers P, Valen-Sendstad K. High-Frequency Fluctuations in Post-stenotic Patient Specific Carotid Stenosis Fluid Dynamics: A Computational Fluid Dynamics Strategy Study. *Cardiovasc Eng Technol*. 2019;10(2):277-298. doi:10.1007/s13239-019-00410-9
152. Viscosity of Whole Blood – viscosity table and viscosity chart :: Anton Paar Wiki. https://wiki.anton-paar.com/us-en/whole-blood/. Accessed February 9, 2022.
153. Dyverfeldt P, Kvitting J-PE, Sigfridsson A, Engvall J, Bolger AF, Ebbers T. Assessment of fluctuating velocities in disturbed cardiovascular blood flow: In vivo feasibility of generalized phase-contrast MRI. *J Magn Reson Imaging*. 2008;28(3):655-663. doi:10.1002/jmri.21475
154. Deshpande MD, Giddens DP. Turbulence measurements in a constricted tube. *J Fluid Mech*. 1980;97(01):65. doi:10.1017/S0022112080002431
155. Petersson S. Simulation of Phase Contrast MRI Measurements from Numerical Flow Data. *Image (Rochester, NY)*. 2008:45. http://liu.diva-portal.org/smash/record.jsf?searchId=4&pid=diva2:25427.
156. Gosman AD, Ioannides E. Aspects of Computer Simulation of Liquid-Fuelled Combustors. *AIAA Pap*. 1981;7(6):482-490. doi:10.2514/6.1981-323
157. Ha H, Park KJ, Dyverfeldt P, Ebbers T, Yang DH. In vitro experiments on ICOSA6 4D flow MRI measurement for the quantification of velocity and turbulence parameters. *Magn Reson Imaging*. 2020;72(June):49-60. doi:10.1016/j.mri.2020.06.020
158. Hasenkam JM, Nygaard H, Giersiepen M, Reul H, Stødkilde-Jørgensen H. Turbulent stress measurements downstream of six mechanical aortic valves in a pulsatile flow model. *J Biomech*. 1988;21(8):631-645. doi:10.1016/0021-9290(88)90201-1
159. Hennel F, Michael ES, Pruessmann KP. Improved gradient waveforms for oscillating gradient spin-echo (OGSE) diffusion tensor imaging. *NMR Biomed*. 2021;34(2):1-11. doi:10.1002/nbm.4434
160. Mofakham AA, Ahmadi G. On random walk models for simulation of particle-laden turbulent flows. *Int J Multiph Flow*. 2020;122:103157. doi:10.1016/j.ijmultiphaseflow.2019.103157
161. Matida EA, Finlay WH, Lange CF, Grgic B. Improved numerical simulation of aerosol deposition in an idealized mouth-throat. *J Aerosol Sci*. 2004;35(1):1-19. doi:10.1016/S0021-8502(03)00381-1
162. Busch J, Vannesjo SJ, Barmet C, Pruessmann KP, Kozerke S. Analysis of temperature dependence of background phase errors in phase-contrast cardiovascular magnetic resonance. *J Cardiovasc Magn Reson*. 2014;16:97. doi:10.1186/s12968-014-0097-6
163. Actively shielded gradients - Questions and Answers in MRI. https://mriquestions.com/active-shielded-gradients.html. Accessed February 7, 2022.

164. Moelker A, Pattynama PMT. Acoustic Noise Concerns in Functional Magnetic Resonance Imaging. *Hum Brain Mapp*. 2003;20(3):123-141. doi:10.1002/hbm.10134
165. Ravicz ME, Melcher JR, Kiang NY-S. Acoustic noise during functional magnetic resonance imaging. *J Acoust Soc Am*. 2000;108(4):1683-1696. doi:10.1121/1.1310190
166. Ravicz ME, Melcher JR. Isolating the auditory system from acoustic noise during functional magnetic resonance imaging: Examination of noise conduction through the ear canal, head, and body. *J Acoust Soc Am*. 2001;109(1):216-231. doi:10.1121/1.1326083
167. Barmet C, De Zanche N, Pruessmann KP. Spatiotemporal magnetic field monitoring for MR. *Magn Reson Med*. 2008;60(1):187-197. doi:10.1002/mrm.21603
168. Wilm BJ, Barmet C, Pavan M, Pruessmann KP. Higher order reconstruction for MRI in the presence of spatiotemporal field perturbations. *Magn Reson Med*. 2011;65(6):1690-1701. doi:10.1002/mrm.22767
169. Rahmer J, Mazurkewitz P, Börnert P, Nielsen T. Rapid acquisition of the 3D MRI gradient impulse response function using a simple phantom measurement. *Magn Reson Med*. 2019;82(6):2146-2159. doi:10.1002/mrm.27902
170. Walker PG, Cranney GB, Scheidegger MB, Waseleski G, Pohost GM, Yoganathan AP. Semiautomated method for noise reduction and background phase error correction in MR phase velocity data. *J Magn Reson Imaging*. 1993;3(3):521-530. doi:10.1002/jmri.1880030315
171. Bernstein M, Pelc NJ, Bernstein MA, et al. Concomitant gradient terms in phase contrast MR : Analysis and correction . Magn Reson Med Concomitant Gradient Terms in Phase Contrast MR : Analysis and Correction. 1998;(MARCH):300-308.
172. Reichenbach JR, Venkatesan R, Yablonskiy DA, Thompson MR, Lai S, Haacke EM. Theory and application of static field inhomogeneity effects in gradient-echo imaging. *J Magn Reson Imaging*. 1997;7(2):266-279. doi:10.1002/jmri.1880070203
173. Markl M, Bammer R, Alley MT, et al. Generalized reconstruction of phase contrast MRI: Analysis and correction of the effect of gradient field distortions. *Magn Reson Med*. 2003;50(4):791-801. doi:10.1002/mrm.10582
174. Winkler S, Wade TP, McKenzie CA, Rutt BK. Accurate vibroacoustic simulations in high performance gradient coils. *Proc Int Soc Magn Res*. 2014;22:3089.
175. Liu L, Sanchez-Lopez H, Liu F, Crozier S. Flanged-edge transverse gradient coil design for a hybrid LINAC-MRI system. *J Magn Reson*. 2013;226:70-78. doi:10.1016/j.jmr.2012.11.017
176. Mechefske CK, Yao G, Li W, Gazdzinski C, Rutt BK. Modal analysis and acoustic noise characterization of a 4T MRI gradient coil insert. *Concepts Magn Reson Part B Magn Reson Eng*. 2004;22(1):37-49. doi:10.1002/cmr.b.20013
177. Yao GZ, Mechefske CK, Rutt BK. Characterization of vibration and acoustic noise in a gradient-coil insert. *Magn Reson Mater Physics, Biol Med*. 2004;17(1):12-27. doi:10.1007/s10334-004-0041-0
178. Rausch M, Gebhardt M, Kaltenbacher M, Landes H. Computer-aided design of clinical magnetic resonance imaging scanners by coupled magnetomechanical-acoustic modeling. *IEEE Trans Magn*. 2005;41(1 I):72-81. doi:10.1109/TMAG.2004.839727

179. Lerch R, Kaltenbacher M, Landes H, et al. Advanced computer modeling of magnetomechanical transducers and their sound fields. *Proc IEEE Ultrason Symp*. 2000;1:747-758. doi:10.1109/ultsym.2000.922654
180. Mechefske CK, Geris R, Gati JS, Rutt BK. Acoustic noise reduction in a 4 T MRI scanner. *Magn Reson Mater Physics, Biol Med*. 2002;13(3):172-176. https://www.sciencedirect.com/science/article/pii/S1352866101001466.
181. Koch KM, Rothman DL, de Graaf RA. Optimization of static magnetic field homogeneity in the human and animal brain in vivo. *Prog Nucl Magn Reson Spectrosc*. 2009;54(2):69-96. doi:10.1016/j.pnmrs.2008.04.001
182. Edelstein WA, Hedeen RA, Mallozzi RP, El-Hamamsy SA, Ackermann RA, Havens TJ. Making MRI quieter. *Magn Reson Imaging*. 2002;20(2):155-163. doi:10.1016/S0730-725X(02)00475-7
183. Shao W, Mechefske CK. Analysis of the sound field in finite length infinite baffled cylindrical ducts with vibrating walls of finite impedance. *J Acoust Soc Am*. 2005;117(4):1728-1736. doi:10.1121/1.1867832
184. Zorumski WE. Generalized radiation impedances and reflection coefficients of circular and annular ducts. *J Acoust Soc Am*. 1973;54(6):1667-1673. doi:10.1121/1.1914466
185. Taracila V, Edelstein WA, Kidane TK, Eagan TP, Baig TN, Brown RW. Analytical calculation of cylindrical shell modes: Implications for MRI acoustic noise. *Concepts Magn Reson Part B Magn Reson Eng*. 2005;25(1):60-64. doi:10.1002/cmr.b.20031
186. Goora F, Han H, Ouellette M, Colpitts BG, Balcom BJ. Investigation of magnetic field gradient waveforms in the presence of a metallic vessel in magnetic resonance imaging through simulation. *IEEE Trans Magn*. 2013;49(6):2920-2932. doi:10.1109/TMAG.2012.2234758
187. Winkler SA, Warr PA, Stockmann JP, et al. Comparison of new element designs for combined RF-shim arrays at 7 T. *Concepts Magn Reson Part B Magn Reson Eng*. 2018;48B(1). doi:10.1002/cmr.b.21364
188. Jiang L, Havens TJ. Environmental vibration induced magnetic field disturbance in MRI magnet. *IEEE Trans Appl Supercond*. 2011;22(3):4400704.
189. Liu L, Sanchez-Lopez H, Poole M, Liu F, Crozier S. Simulation and analysis of split gradient coil performance in MRI. In: *2011 Annual International Conference of the IEEE Engineering in Medicine and Biology Society*. IEEE; 2011:4149-4152.
190. Winkler SA, Alejski A, Wade T, McKenzie C, Rutt BK. A traveling-wave approach to acoustic noise reduction in MR gradient coils. In: *Proc Intl Soc Mag Reson Med*. Vol 21. ; 2014:4852.
191. Wang Y, Liu F, Crozier S. Simulation study of noise reduction methods for a split MRI system using a finite element method. *Med Phys*. 2015;42(12):7122-7131. doi:10.1118/1.4935864
192. Mechefske CK, Wang F. Theoretical, numerical, and experimental modal analysis of a single-winding gradient coil insert cylinder. *Magn Reson Mater Physics, Biol Med*. 2006;19(3):152-166. doi:10.1007/s10334-006-0038-y
193. Lifschitz EM, Landau D. *Lehrbuch Der Theoretischen Physik: Bd.1 Mechanik*. Europa-Lehrmittel; 1967.

194. Mansfield P. Multi-planar image formation using NMR spin echoes. *J Phys C Solid State Phys*. 1977;10(3):55-58. doi:10.1088/0022-3719/10/3/004
195. Jezzard P, Balaban RS. Correction for geometric distortion in echo planar images from B0 field variations. *Magn Reson Med*. 1995;34(1):65-73. doi:10.1002/mrm.1910340111
196. DeLaPaz RL. Echo-planar imaging. *Radiographics*. 1994;14(5):1045-1058. doi:10.1148/radiographics.14.5.7991813
197. Kasper L, Bollmann S, Vannesjo SJ, et al. Monitoring, analysis, and correction of magnetic field fluctuations in echo planar imaging time series. *Magn Reson Med*. 2015;74(2):396-409. doi:10.1002/mrm.25407
198. Dillinger H, Kozerke S, Guenthner C. Direct Comparison of Gradient Modulation Transfer Functions and Acoustic Noise Spectra of the same MRI at High- (3T) and Lower-Field (0.75T). In: *Proc. Intl. Soc. Mag. Reson. Med. 30*.
199. Dillinger H, Peper ES, Guenthner C, Kozerke S. Background Phase Error Reduction in Phase-Contrast MRI based on Acoustic Noise Recordings. In: *Intl. Soc. Mag. Reson. Med. 30*. ; 2021.
200. Leupold J, Hennig J, Scheffler K. Moment and direction of the spoiler gradient for effective artifact suppression in RF-spoiled gradient echo imaging. *Magn Reson Med*. 2008;60(1):119-127. doi:10.1002/mrm.21614
201. Walker PG, Cranney GB, Scheidegger MB, Waseleski G, Pohost GM, Yoganathan AP. Semiautomated method for noise reduction and background phase error correction in MR phase velocity data. *J Magn Reson Imaging*. 1993;3(3):521-530. doi:10.1002/jmri.1880030315
202. Callaghan FM, Burkhardt B, Geiger J, Valsangiacomo Buechel ER, Kellenberger CJ. Flow quantification dependency on background phase correction techniques in 4D-flow MRI. *Magn Reson Med*. 2020;83(6):2264-2275. doi:10.1002/mrm.28085
203. Rolf MP, Hofman MBM, Gatehouse PD, et al. Sequence optimization to reduce velocity offsets in cardiovascular magnetic resonance volume flow quantification - A multi-vendor study. *J Cardiovasc Magn Reson*. 2011;13(1):1-10. doi:10.1186/1532-429X-13-18
204. Guenthner C, Sethi S, Troelstra M, Dokumaci AS, Sinkus R, Kozerke S. Ristretto MRE: A generalized multi-shot GRE-MRE sequence. *NMR Biomed*. 2019;32(5):1-13. doi:10.1002/nbm.4049
205. Edelstein WA, Glover GH, Hardy CJ, Redington RW. The intrinsic signal-to-noise ratio in NMR imaging. *Magn Reson Med*. 1986;3(4):604-618. doi:10.1002/mrm.1910030413
206. Darrasse L, Ginefri JC. Perspectives with cryogenic RF probes in biomedical MRI. *Biochimie*. 2003;85(9):915-937. doi:10.1016/j.biochi.2003.09.016
207. Hayes CE, Axel L. Noise performance of surface coils for magnetic resonance imaging at 1.5 T. *Med Phys*. 1985;12(5):604-607. doi:10.1118/1.595682
208. Simonetti OP, Ahmad R. Low-Field Cardiac Magnetic Resonance Imaging: A Compelling Case for Cardiac Magnetic Resonance's Future. *Circ Cardiovasc Imaging*. 2017;10(6):1-7. doi:10.1161/CIRCIMAGING.117.005446
209. Marques JP, Simonis FFJ, Webb AG. Low-field MRI: An MR physics perspective. *J Magn Reson Imaging*. 2019;49(6):1528-1542. doi:10.1002/jmri.26637

210. Campbell-Washburn AE, Suffredini AF, Chen MY. High-performance 0.55-T Lung MRI in patient with COVID-19 infection. *Radiology*. 2021;299(2):E246-E247. doi:10.1148/RADIOL.2021204155
211. Zwanenburg JJM, Hendrikse J, Visser F, Takahara T, Luijten PR. Fluid attenuated inversion recovery (FLAIR) MRI at 7.0 Tesla: Comparison with 1.5 and 3.0 Tesla. *Eur Radiol*. 2010;20(4):915-922. doi:10.1007/s00330-009-1620-2
212. Campbell-Washburn AE, Ramasawmy R, Restivo MC, et al. Opportunities in interventional and diagnostic imaging by using high-performance low-field-strength MRI. *Radiology*. 2019;293(2):384-393. doi:10.1148/radiol.2019190452
213. Moelker A, Wielopolski PA, Pattynama PMT. Relationship between magnetic field strength and magnetic-resonance-related acoustic noise levels. *MAGMA Magn Reson Mater Physics, Biol Med*. 2003;16(1):52-55. doi:10.1007/s10334-003-0005-9
214. McJury PhD M, Shellock PhD FG. Auditory Noise Associated With MR Procedures: A Review. *J Magn Reson Imaging*. 2000;12(1):37-45. doi:10.1002/1522-2586(200007)12:1<37::AID-JMRI5>3.0.CO;2-I
215. Hutter J, Price AN, Cordero-Grande L, et al. Quiet echo planar imaging for functional and diffusion MRI. *Magn Reson Med*. 2018;79(3):1447-1459. doi:10.1002/mrm.26810
216. Fischer S, Grodzki DM, Domschke M, et al. Quiet MR sequences in clinical routine: initial experience in abdominal imaging. *Radiol Medica*. 2017;122(3):194-203. doi:10.1007/s11547-016-0710-x
217. Segbers M, Rizzo Sierra C V., Duifhuis H, Hoogduin JM. Shaping and timing gradient pulses to reduce MRI acoustic noise. *Magn Reson Med*. 2010;64(2):546-553. doi:10.1002/mrm.22366
218. Hedeen RA, Edelstein WA. Characterization and prediction of gradient acoustic noise in MR imagers. *Magn Reson Med*. 1997;37(1):7-10. doi:10.1002/mrm.1910370103
219. Jiang L, Havens TJ. Environmental vibration induced magnetic field disturbance in MRI Magnet. *IEEE Trans Appl Supercond*. 2012;22(3):10-13. doi:10.1109/TASC.2011.2177051
220. T. Hamaguchi, T. Miyati, T. Matsushita, N. Ohno; Kanazawa K. Analysis of spatial dependence of acoustic noise transfer function in magnetic resonance imaging. In: *ECR 2014*. ; 2014:C-1988. doi:10.1594/ecr2014/C-1988
221. Li G, Mechefske CK. Structural-acoustic modal analysis of cylindrical shells: Application to MRI scanner systems. *Magn Reson Mater Physics, Biol Med*. 2009;22(6):353-364. doi:10.1007/s10334-009-0185-z
222. Foerster BU, Tomasi D, Caparelli EC. Magnetic field shift due to mechanical vibration in functional magnetic resonance imaging. *Magn Reson Med*. 2005;54(5):1261-1267. doi:10.1002/mrm.20695
223. Campbell-Washburn AE, Xue H, Lederman RJ, Faranesh AZ, Hansen MS. Real-time distortion correction of spiral and echo planar images using the gradient system impulse response function. *Magn Reson Med*. 2016;75(6):2278-2285. doi:10.1002/mrm.25788
224. Robison RK, Li Z, Wang D, Ooi MB, Pipe JG. Correction of B 0 eddy current effects in spiral MRI. *Magn Reson Med*. 2019;81(4):2501-2513.

doi:10.1002/mrm.27583
225. Stich M, Wech T, Slawig A, et al. Gradient waveform pre-emphasis based on the gradient system transfer function. *Magn Reson Med*. 2018;80(4):1521-1532. doi:10.1002/mrm.27147
226. Barmet C, De Zanche N, Wilm BJ, Pruessmann KP. A transmit/receive system for magnetic field monitoring of in vivo MRI. *Magn Reson Med*. 2009;62(1):269-276. doi:10.1002/mrm.21996
227. De Zanche N, Barmet C, Nordmeyer-Massner JA, Pruessmann KP. NMR Probes for measuring magnetic fields and field dynamics in MR systems. *Magn Reson Med*. 2008;60(1):176-186. doi:10.1002/mrm.21624
228. Sipilä P, Greding S, Wachutka G, Wiesinger F. 2H transmit-receive NMR probes for magnetic field monitoring in MRI. *Magn Reson Med*. 2011;65(5):1498-1506. doi:10.1002/mrm.22741
229. Duyn JH, Yang Y, Frank JA, Van Der Veen JW. Simple Correction Method for k-Space Trajectory Deviations in MRI. *J Magn Reson*. 1998;132(1):150-153. doi:10.1006/jmre.1998.1396
230. Vannesjo SJ, Duerst Y, Vionnet L, et al. Gradient and shim pre-emphasis by inversion of a linear time-invariant system model. *Magn Reson Med*. 2017;78(4):1607-1622. doi:10.1002/mrm.26531
231. Lvovsky Y, Zhang Z, Hollis T, Bai Y. Passive Shimming of MRI Magnets with B0 >= 3T at Reduced Field. *Proc Intl Soc Mag Reson Med 20*. 2012;20:2583. https://cds.ismrm.org/protected/12MProceedings/files/2583.pdf.
232. Bydder M, Hamilton G, Yokoo T, Sirlin CB. Optimal phased-array combination for spectroscopy. *Magn Reson Imaging*. 2008;26(6):847-850. doi:10.1016/j.mri.2008.01.050
233. Shao W, Mechefske CK. Acoustic analysis of a gradient coil winding in an MRI scanner. *Concepts Magn Reson Part B Magn Reson Eng*. 2005;24(1):15-27. doi:10.1002/cmr.b.20023
234. Clayton DB, Elliott MA, Leigh JS, Lenkinski RE. 1H spectroscopy without solvent suppression: Characterization of signal modulations at short echo times. *J Magn Reson*. 2001;153(2):203-209. doi:10.1006/jmre.2001.2442
235. Guenthner C, Dillinger H, Boernert P, Kozerke S. Three-Point Dixon Abdominal Water/Fat Separation using a Lower-Field 0.75T MRI. In: *Intl. Soc. Mag. Reson. Med. 29*. ; 2021:1283.
236. Wedeen VJ, Weisskoff RM, Poncelet BP. MRI signal void due to in-plane motion is all-or-none. *Magn Reson Med*. 2007;32(1):116-120. doi:10.1002/mrm.1910320116
237. Duerk JL, Simonetti OP. Review of MRI gradient waveform design methods with application in the study of motion. *Concepts Magn Reson*. 1993;5(2):105-122. doi:10.1002/cmr.1820050202
238. Luk Pat GT, Meyer CH, Pauly JM, Nishimura DG. Reducing flow artifacts in echo-planar imaging. *Magn Reson Med*. 1997;37(3):436-447. doi:10.1002/mrm.1910370323
239. Westenberg JJM, Assen HC, den Boogaard PJ, et al. Echo planar imaging–induced errors in intracardiac 4D flow MRI quantification. *Magn Reson Med*. 2021;(August):1-14. doi:10.1002/mrm.29112

240. Buonocore MH, Gao L. Ghost artifact reduction for echo planar imaging using image phase correction. *Magn Reson Med.* 1997;38(1):89-100. doi:10.1002/mrm.1910380114
241. Reeder SB, Atalar E, Bolster BD, McVeigh ER. Quantification and reduction of ghosting artifacts in interleaved echo- planar imaging. *Magn Reson Med.* 1997;38(3):429-439. doi:10.1002/mrm.1910380312
242. Delakis I, Petala K, De Wilde JP. MRI receiver frequency response as a contributor to Nyquist ghosting in echo planar imaging. *J Magn Reson Imaging.* 2005;22(2):324-328. doi:10.1002/jmri.20365
243. Grieve SM, Blamire AM, Styles P. Elimination of Nyquist ghosting caused by read-out to phase-encode gradient cross-terms in EPI. *Magn Reson Med.* 2002;47(2):337-343. doi:10.1002/mrm.10055
244. Chen NK, Wyrwicz AM. Removal of EPI Nyquist ghost artifacts with two-dimensional phase correction. *Magn Reson Med.* 2004;51(6):1247-1253. doi:10.1002/mrm.20097
245. Porter DA, Calamante F, Gadian DG, Connelly A. The effect of residual Nyquist ghost in quantitative echo-planar diffusion imaging. *Magn Reson Med.* 1999;42(2):385-392. doi:10.1002/(SICI)1522-2594(199908)42:2<385::AID-MRM21>3.0.CO;2-J
246. Hennel F. Image-Based Reduction of Artifacts in Multishot Echo-Planar Imaging. *J Magn Reson.* 1998;134(2):206-213. doi:10.1006/jmre.1998.1502
247. Hu X, Le TH. Artifact reduction in EPI with phase-encoded reference scan. *Magn Reson Med.* 1996;36(1):166-171. doi:10.1002/mrm.1910360126
248. Slavin GS, Riederer SJ. Gradient moment smoothing: A new flow compensation technique for multi- shot echo-planar imaging. *Magn Reson Med.* 1997;38(3):368-377. doi:10.1002/mrm.1910380304
249. Smith TB, Nayak KS. MRI artifacts and correction strategies. *Imaging Med.* 2010;2(4):445-457. doi:10.2217/iim.10.33
250. Pruessmann KP, Weiger M, Börnert P, Boesiger P. Advances in sensitivity encoding with arbitrary k -space trajectories. *Magn Reson Med.* 2001;46(4):638-651. doi:10.1002/mrm.1241
251. Pruessmann KP, Weiger M, Scheidegger MB, Boesiger P. SENSE: Sensitivity encoding for fast MRI. *Magn Reson Med.* 1999;42(5):952-962. doi:10.1002/(SICI)1522-2594(199911)42:5<952::AID-MRM16>3.0.CO;2-S
252. Pedersen H, Kozerke S, Ringgaard S, Nehrke K, Won YK. K-t PCA: Temporally constrained k-t BLAST reconstruction using principal component analysis. *Magn Reson Med.* 2009;62(3):706-716. doi:10.1002/mrm.22052
253. Tsao J, Boesiger P, Pruessmann KP. k-t BLAST and k-t SENSE: Dynamic MRI with high frame rate exploiting spatiotemporal correlations. *Magn Reson Med.* 2003;50(5):1031-1042.
254. Gamper U, Boesiger P, Kozerke S. Compressed sensing in dynamic MRI. *Magn Reson Med.* 2008;59(2):365-373. doi:10.1002/mrm.21477
255. Weiger M, Overweg J, Rösler MB, et al. A high-performance gradient insert for rapid and short-T2 imaging at full duty cycle. *Magn Reson Med.* 2018;79(6):3256-3266. doi:10.1002/mrm.26954

256. Jesmanowicz A, Wong EC, Hyde JS. Phase correction for EPI using internal reference lines. In: *Proc., SMRM, 12th Annual Meeting, New York*. ; 1993:1239.
257. Corral-Acero J, Margara F, Marciniak M, et al. The "Digital Twin" to enable the vision of precision cardiology. *Eur Heart J.* 2020;41(48):4556-4564B. doi:10.1093/eurheartj/ehaa159

List of Publications

Peer-Reviewed Publications

1. Dillinger H, Kozerke S, Guenthner C. Direct Comparison of Gradient Fidelity and Acoustic Noise of the Same MRI System at 3T and 0.75T; in submission
2. Dillinger H, McGrath C, Guenthner C, Kozerke S. Fundamentals of Turbulent Flow Spectrum Imaging; *Magn Reson Med.* 2021;(August):1-19. doi:10.1002/mrm.29001
3. Corso P, Walheim J, Dillinger H, et al. Toward an accurate estimation of wall shear stress from 4D flow magnetic resonance downstream of a severe stenosis. *Magn Reson Med.* 2021;86(3):1531-1543. doi:10.1002/mrm.28795
4. Dillinger H, Walheim J, Kozerke S. On the limitations of echo planar 4D flow MRI. *Magn Reson Med.* 2020;84(4):1806-1816. doi:10.1002/mrm.28236
5. Walheim J, Dillinger H, Gotschy A, Kozerke S. 5D Flow Tensor MRI to Efficiently Map Reynolds Stresses of Aortic Blood Flow In-Vivo. *Sci Rep.* 2019;9(1):1-12. doi:10.1038/s41598-019-55353-x
6. Walheim J, Dillinger H, Kozerke S. Multipoint 5D Flow Cardiovascular Magnetic Resonance - Accelerated Cardiac- and Respiratory-Motion Resolved Mapping of Mean and Turbulent Velocities. *J Cardiovasc Magn Reson.* 2019. doi:10.1186/s12968-019-0549-0

Conference Contributions

1. Beat Phenomena in MRI - Theoretical and Experimental Description of the Impact of Mechanical Resonances on Fast Readouts. Dillinger H, Kozerke S. Proceedings of the 31st Annual Meeting of ISMRM. 2022.
2. Mechanical Resonance Recording and Analysis using auDIO files (MR-RADIO). Dillinger H, Peper E, Guenthner C, Kozerke S. Proceedings of the 31st Annual Meeting of ISMRM. 2022.
3. Background Phase Error Reduction in Phase-Contrast MRI based on Acoustic Noise Recordings. Dillinger H, Peper E, Guenthner C, Kozerke S. Proceedings of the 30th Annual Meeting of ISMRM. 2021.
4. Direct Comparison of Gradient Modulation Transfer Functions and Acoustic Noise Spectra of the same MRI at High- (3T) and Lower-Field (0.75T). Dillinger H, Kozerke S, Guenthner C. Proceedings of the 30th Annual Meeting of ISMRM. 2021.
5. Limits of Turbulent Flow Spectrum Encoding using 4D Flow MRI. Dillinger H, McGrath C, Kozerke S. Proceedings of the 30th Annual Meeting of ISMRM. 2021.
6. Three-Point Dixon Abdominal Water/Fat Separation using a Lower-Field 0.75T MRI. Guenthner C, Dillinger H, Boernert P, Kozerke S. Proceedings of the 30th Annual Meeting of ISMRM. 2021.

7. Member Initiated Symposium Flow and Motion Study Group “Turbulence in and around the heart” at the 30th Annual Meeting of ISMRM. 2021.
8. Junior Fellows Symposium: ISMRM Shark Tank Finalist “MR-RADIO (Mechanical Resonance Recording & Analysis using auDIO files)” at the 30th Annual Meeting of ISMRM. 2021.

9. 5D Flow Tensor MRI with Multipoint Encoding for Efficient Mapping of Reynolds Stresses in the In-vivo Aorta. Walheim J, Dillinger H, Gotschy A, Kozerke S. Proceedings of the 29th Annual Meeting of ISMRM. 2020.
10. Limitations of Echo Planar Imaging in PC-MRI of High Flow Regimes. Dillinger H, Walheim J, van Gorkum R, Kozerke S. Proceedings of the 29th Annual Meeting of ISMRM. 2020.
11. Combining variational methods and particle tracking in 4D Flow MRI for displacement artifact compensation. Buoso S, Dillinger H, Kozerke S. Proceedings of the 29th Annual Meeting of ISMRM. 2020.
12. Improved In Vivo Estimation of the Reynolds Stress Tensor from 4D und 5D Flow MRI Using Cholesky Decomposition-Based Neural Networks. Vishnevskiy V, Dillinger H, Walheim J, Zhang L, Kozerke S. Proceedings of the 29th Annual Meeting of ISMRM. 2020.

13. Flow Effects in Echo Planar 4D Flow MRI. Dillinger H, Walheim J, Kozerke S. Proceedings of the 36th Annual Scientific Meeting of ESMRMB. 2019.
14. Multi-Point 5D Flow MRI - Accelerated Cardiac- and Respiratory-Motion Resolved Mapping of Mean and Turbulent Velocities in 4 Minutes. Walheim J, Dillinger H, Kozerke S. Proceedings of the 28th Annual Meeting of ISMRM. 2019.
15. 5D Flow Tensor MRI for Mapping Reynolds Stresses in the Aorta. Jonas W, Dillinger H, Kozerke S. Proceedings of the 28th Annual Meeting of ISMRM. 2019.
16. Multi-Point 5D Flow MRI - Accelerated Cardiac- and Respiratory-Motion Resolved Mapping of Mean and Turbulent Velocities in 4 Minutes. Walheim J, Dillinger H, Kozerke S. Proceedings of the 28th Annual Meeting of ISMRM. 2019.
17. Rapid cardiac MR myocardial perfusion quantification using machine learning trained with synthetically generated sample data. Hoh T, von Spiczak J, Joyce T, Lingwood R, Dillinger H, Kozerke S. Proceedings of the 36th Annual Scientific Meeting of ESMRMB. 2019.

18. Easy-to-Implement and Rapid Image Reconstruction of Accelerated Cine and 4D Flow MRI Using TensorFlow. Vishnevskiy V, Walheim J, Dillinger H, Kozerke S. Proceedings of the 27th Annual Meeting of ISMRM. 2018.

Acknowledgements

This endeavor would not have been possible without the contribution and support of many. First of all, I'd like to express my deepest gratitude to my supervisor Prof. Dr. Sebastian Kozerke for giving me the opportunity to conduct my PhD project in his group. His valuable guidance, feedback and open mindset supported my progression in the field and enabled me to follow up on own ideas. Furthermore, I am grateful for Prof. Dr. Dominik Obrist who agreed on reviewing this thesis.

I am deeply indebted to Jonas Walheim, who introduced me to the research field and related workflows. His offering of unconditional assistance and consultation made my journey in the MR realm much more enjoyable and kept me sane during the course of my PhD. In addition, I would like to thank another valued member of the flow team, Eva Peper for the great collaboration and her unparalleled support during extensive scan sessions.

Many thanks go to Christian Günthner for discussing even the most unorthodox MR-related ideas with me while contributing his consolidated knowledge which made our cooperation not only joyful but also fruitful.

I am thankful for my current and former office mates, who made this working environment a blessed one. Besides the colleagues already mentioned, I would like to highlight Mareike Gastl, Stefano Buoso, Robbert van Gorkum, Tobias Hoh and Jonathan Weine for a pleasing atmosphere in our office and the open discussion of ideas. This also applies to my lab colleagues Julia Busch, Sophie Peereboom, Johanna Stimm, Julia Trächtler, Gloria Wolkerstorfer, Mohammed Albannay, Constantin von Deuster, Andreas Dounas, Pietro Dirix, Maximilian Fütterer, Alexander Gotschy, Greg Kwiatkowski, Charles McGrath, Xavier Montoya, Moritz Platscher, Georg Spinner, Christian Stöck, Valery Vishnevskiy, Jochen von Spiczak, Gevin von Witte, Conny Waschkies, Patrick Wespi, Jonathan Zopes, the colleagues being part of the MR hardware group and more. Thanks to all of you for not only being coworkers but becoming valued friends.

I would also like to extend my thanks to the Gyrotools team, especially Martin Bührer and Gérard Crelier, and also Roger Lüchinger for offering their help on processing data, accessing scanners and software. Big thanks go to Isabel Spiess for her organizational work at the institute where she ensures that everything runs smoothly and to our former technician Stephen Wheeler who has supported me by bringing my ideas to life in an MR-compatible way. In addition, I would like to mention my students and project partners, who gave me the opportunity to learn from them in many ways.

Esther, you make cornered rooms round, you bring colors in my life that I would not have been able to see without you. Thank you for your support and love throughout the years. I am extremely grateful to have you in my life.

Dear Margarete and Michael, thank you for your unconditional love and assistance in a way a child can only wish for. Barbara, thanks for being a role model as my big sister – I have and will always look up to you. Lukas and Theo, I am happy that you are part of our family. Last but not least, I would like to thank my family members and friends which are not named here.

Wie merkwürdig ist die Situation von uns Erdenkindern? Für einen kurzen Besuch ist jeder da. Er weiss nicht wofür, aber manchmal glaubt er es zu fühlen. Vom Standpunkt des täglichen Lebens ohne tiefe Reflektion weiss man aber: Man ist da für die anderen Menschen. Zunächst für diejenigen, von deren Lächeln und Wohlsein das eigene Glück völlig abhängig ist. Dann aber auch für die vielen Unbekannten, mit deren Schicksal uns ein Band des Mitfühlens verknüpft. Jeden Tag denke ich unzählige Male daran, dass mein äusseres und inneres Leben auf der Arbeit der jetzigen und schon verstorbenen Menschen beruht, dass ich mich anstrengen muss, um zu geben im gleichen Ausmass, wie ich empfangen habe und noch empfange.

How strange is the lot of us mortals! Each of us is here for a brief sojourn; for what purpose he knows not, though he sometimes thinks he senses it. But without deeper reflection one knows from daily life that one exists for other people - first of all for those upon whose smiles and well-being our own happiness is wholly dependent, and then for the many, unknown to us, to whose destinies we are bound by the ties of sympathy. A hundred times every day I remind myself that my inner and outer life are based on the labors of other men, living and dead, and that I must exert myself in order to give in the same measure as I have received and am still receiving.

Albert Einstein, Mein Weltbild / The World As I See It